Hydro-dynamic Effects with Particular Consideration of Water Quality and their Measurement Methods

Winfried Heller

Institut für Strömungsmechanik
Technische Universität Dresden

This work was approved by the Faculty of Engineering of Dresden University of Technology as habilitation thesis in order to grant the academic degree of a habilitated doctor (Doctor habilitatus):

Habilitation thesis submitted:	18.04.2005
Day of the defense:	15.12.2005

Chairman:	Prof. Dr.-Ing. habil. Prof. h.c. H.-J. Hardtke,	Technische Universität Dresden
Reviewers:	Prof. Dr.-Ing. habil. A. Dittmann,	Technische Universität Dresden
	Prof. Dr.-Ing. habil. N. A. Adams,	Technische Universität München
	Prof. Dr. rer.nat. habil W. Lauterborn,	Universität Göttingen

English translation of the original text by
Göran Thomas, email: goeran_t@web.de

Published (german) in:
Strömungsmechanik, Band 2
Der Andere Verlag, Tönning, Lübeck and Marburg
ISBN 3-89959-428-2

Preface

Thanks to outstanding mathematicians and natural scientists of previous centuries such as Isaac Newton (1642 – 1727), Leonhard Euler (1701 – 1783), Claude Louis Marie Henry Navier (1785 – 1836), George Gabriel Stokes (1819 – 1903), Osborne Reynolds (1842 – 1912), John William Strutt Rayleih (1842 – 1919) and Ludwig Prandtl (1875 – 1953), the field of fluid mechanics has evolved into an independent branch of science with great significance for the basic education of engineers. However, the equations devised by these scientists for the calculation of fluid flows have one thing in common: They do not explicitly describe the hydrodynamic effects that result from a fluid's quality.

This founded the motivation for the present thesis because, during the last decades, this area was subject to intensive research, in which I also participated. This work is meant to be a contribution to summarizing the development of fluid mechanics with particular emphasis on water quality and hydro-dynamic effects. At this point, I would like to thank all those who greatly supported me during my work.

I wish to express my particular gratitude to Dr. rer.nat. Andreas Keller of the Laboratory of Hydraulic Engineering at Munich University, whose exceptionally competent specialist support paved the way for this work. Moreover, for professionally discussing and reviewing this thesis, I would like to thank Prof. Dr. rer.nat. habil. Werner Lauterborn of Göttingen University, Prof. Dr.-Ing. habil. Nicolaus Adams of Munich Technical University and Prof. Dr.-Ing. habil. Achim Dittmann of Dresden Technical University.

My deepest gratitude, however, goes to my wife Elke, who not only provided the necessary private backing throughout my professional career but also actively participated in it.

Winfried Heller
Possendorf, January 2006

Contents

List of Symbols and Indices

Symbols

a	m/s	sound velocity, constant
A	m^2	area
b	-	constant
B	T	strong mactnetic field
b_i	-	diffuse ligth term
c	-	concentration, solubility
c_A, c_L	-	lift coefficient
c_W, c_D	-	drag coefficientt
c_p	J/kg K	specific heat at constant pressure
$c_{p\,min}$	-	minimal pressure coefficient
c_v	J/kg K	specific heat at constant volume
D	m^2/s	diffusion constant
d	m	diameter
E	N m	energy
f	-	saturation degree
F	N	force
G	m^2/s^2	potential
G_A	-/s	gas precipitation
H	Pa	Henry coeffizient
k	m^2/N	proportional factor
K	-	calibration factor
k_p	-	coefficient
M	kg/kMol	molecular weigth
m	kg	mass
$\dot{m}$	kg/s	mass flow
n	-	number of moles
n	-	isentropic exponent
N	-	interaction parameter
n'	$1/m^3$	mole per volume
n_M	-	refraction
p	Pa, bar,	pressure
q	m/s	velocity
R	m	radius
r	m	coordinate, radius
R_G	J/kg K	gas constant
S	N/m	surface tension
T	K	absolute temperature
t	s	time
$\vec{u}$	m/s	velocity vector
u	m/s	velocity component
V	m^3	volume
$\dot{V}$	m^3/s	volume flow
x	m	coordinate
y	m	coordinate
α	vol ‰	absorption coefficient, gas content

β	Bq	radiation
ϑ	°C	temperature
ν	m^2/s	kinematic viscosity
φ	-	angle
ϕ	-	anglel
ρ	kg/m^3	density
κ	-	adiabatic exponent
λ	-, m	technical solubility coefficient, wave length
Γ	m^2/s	vortex intensity
γ	Bq	radiation
ω	1/s	angular velocity
σ	-	cavitation number
α'	-	Oswald distribution coefficient
λ_0	m	wave length in vacuum
ϕ_i	-	phase delay
Θ	-	angle
η	-	constant
σ_L	S/min	conductivity
Λ	-	coefficient
Ω	1/s	angular frequency
ε	kJ/kg K	specific heat
δ	-	angle
ζ	-	loss coefficient

Indices

A	lift
Bl	bubble
D	drag
E	inflow
Fl	fluid
G	gas
Gl	equilibrium
i	inside
K	curve
krit	critical
L	lift
M	dial gage
R	tube
ref	reference
S	Sättigung
V	vapor, loss
W	water
∞	infinite, undisturbed
0	initial state

1 Introduction

1.1 Historical Framework and Motivation

Seit Flowing fluids have always been fascinating to man, and experience with properties of fluids, especially water, is of general nature. Since the day of our birth we have bathed in water, drunken liquids, or seen rain drops fall. Like humans, plants and animals largely consist of water. So, every young scientist or engineer begins his education with a good deal of empirical knowledge about fluids. This knowledge, however, may consist of many unrelated individual bits of experience, probably often resulting in a rather intuitive feeling than an accurate collection of facts. This intuition might also have guided Leonardo da Vinci (1452 until 1519) when, already more than 500 years ago, he drew flow structures behind a pole in flowing water.

Figure 1: Leonardo da Vinci. Studies with an old man and water, around 1513

Intuition also tells that, in a fluid, a cavity will be created in every place where an infinitesimal tension occurs, because a liquid, so easily flowing, splashing or sloshing around, dividing and re-merging, cannot possibly have a tensile strength. However, there are several examples from nature casting a shadow on that intuitive knowledge telling us that fluids could not sustain tensile stresses. Trees, for instance, drag water out of the earth into considerable heights, which can only be explained by conceding the property of sustaining tensile stresses to fluids.

Famous mathematicians and natural scientists of the last centuries endeavored to fathom the observed streaming phenomena and to analyze them mathematically.

Isaac Newton (1642 – 1727), a British philosopher, mathematician and medic, laid the foundations of classic mechanics by formulating the three basic laws of motion. Newton first observed that the inner molecular friction between two neighboring fluid elements basically depends only on the alteration of velocity when transiting from one element to the other. His attempt to calculate the tensile strains in fluids and the term 'Newton Fluid' belong the principles of modern fluid mechanics.

Leonard Euler (1701 – 1783), who is denominated the most important mathematician of the enlightenment, also worked in the field of hydro-dynamics. Founding on the fundamental law of

dynamics, which goes back to Newton's principle of inertia, Euler formulated the equation of motion for inviscid fluids. Euler's equation was integrated by Daniel Bernoulli (1700 – 1782), who, with this equation, could show the correlation, that the total pressure within a system is constant and additively composed of the static and the dynamic pressure.

The Navier-Stokes Equations are a system of non-linear partial differential equations of second order from the field of fluid mechanics. They represent the principle of linear momentum in differential form and characterize the behavior of flows in fluids and gas mixtures, namely the dependency of velocity and pressure as a function of position and time. However, this particular principle of linear momentum is only valid for Newton fluids, such as water or air.

The equations are named after the Frenchman Claude Louis Henry Navier (1785 – 1836) and the Brit George Gabriel Stokes (1819 – 1903), who had both developed the equations independently in the first half of the nineteenth century (1827 – 1845). Until today, it has not been achieved to prove the existence of global solutions, and until today, this problem is one of the most important unsolved mathematical problems, whose solution has been promised a reward of one million dollars.

The Irishman Osborne Reynolds (1842 – 1912) initially worked as an Engineer, and was then appointed the first English chair of Civil and Mechanical Engineering at Owens College in Manchester. He authored numerous important works about hydro-mechanics. The Reynolds criterion for the transition of laminar to turbulent flow is named after him.

Lord John Williams Rayleigh (1842 – 1919) examined the legalities a gas bubble is subjected to in a fluid at a certain pressure. This initially only static approach was changed by M.S. Plesset into a dynamic, time-independent equation. The resulting Rayleigh-Plesset Equation is a differential equation that qualifies bubble growth depending on time, pressure, surface tension, inertia and viscosity.

Ludwig Prandtl (1875 – 1953) discovered the importance of the boundary layer and formulated the Boundary Layer Theory. In 1907 he conducted tests with supersonic flow and made ground-breaking contributions by introducing the model experiment in the wind tunnel. Prandtl developed a theory of turbulent flow with the Prandtl number as a parameter and a wing theory that had important influences on aircraft construction.

The list of famous scientists could still be continued. To both them and the vehement technical development of the twentieth century it must be accredited that fluid mechanics have advanced from a branch of physics to become an independent field of science. Nonetheless, the equations for calculating fluid flows set up by those scientists have one element in common. They do not describe explicitly the hydro-dynamic effects resulting from a fluid's characteristics and their quality.

This was the actual motivation of this paper as over the last decades there has been a great deal of intense research in this area, to which the author contributed as well. Particularly in the field of flow cavitation, but also in magneto-hydro-dynamics a fluid's quality and its reaction to outside influences, such as velocity, pressure, temperature and so on, plays an important role.

Fluids, especially water, are solvents not only of salts and minerals, but also of gases. Thus, they are a conglomerate of dissolved and undissolved solids, of dissolved and free gas bubbles as well as often biological substances. The quantity and size distribution of the undissolved gas bubbles and solids as well as the state of saturation are characteristics of the solution and affect a fluid's

properties. There is a particularly clear correlation between the quality of a fluid and its property of building up tensile strength.
An additional motivation to summarize the current state of research was the fact that, considering the field of technical engineering, the primary interest lies with a fluid's properties that appear in practice and that these should be measured with the greatest possible ease as well as accuracy. Additionally, until today, it has been very difficult to find a suitable measurement method to determine a fluid's quality. Particularly shipbuilders with their research institutes, producers of pumps or hydraulic engineers are still greatly interested in both the theoretical description of the physical processes in technical flows and in the development of suitable measuring devices.

To this date, no comprehensive account of the developments in this area has become known to the author. This paper attempts to make a contribution to cover this scientifically and technically very demanding topic comprehensively. For this purpose, the most important publications in this area have been arranged into the respective chapters with regard to the objective of this work.

Subsequently, an overview of the development and the current stage of research in this field will be given. Naturally, there will only be a selection out of the great number of published works. Regarding methods and devices to determine gas concentration and tensile strength in water, nearly the complete development can be reproduced.

The main focus of this work will be the depiction of the scientific development of fluid mechanics with particular emphasis on the water quality in regard to hydro-dynamic effects. Regarding content, it has been set store by the historical development and the detailed description of the individual chapters of historic development. The primary objective of this work is the complete and comprehensive presentation of the scientific development in this area from the advent of the twentieth century until the state of research at the beginning of the twenty first century.

1.2 Physical Foundations for Fluids

Even today, not all questions concerning the structure of water have been answered yet. X-ray structure analysis has shown that the particle distribution in a fluid is not entirely arbitrary (especially near melting point), as it is in gases. Within fluids, the degree of a short-range order remains. Naturally, due to the disappearance of the long-range order, fluids lose their isotropic property, which is characteristic of crystalline bodies.

In addition, the small relative volume change of most substances during melting (about 10%) proves that there must be a certain similarity between the order of particles in fluids and the order of these particles in their respective solid substances. Furthermore, experiments show that the latent heat of fusion is very small compared to the latent heat of vaporization, which is about 30 to 40 times as much. This means that during melting, intermolecular bonding forces are only weakened relatively little.

Therefore, forces between fluid molecules cause similarly strong bonds compared to solids. Cohesion forces between fluid molecules, just as adhesion forces between a fluid and a solid, are induced by the so-called van der Waals-forces, which are attracting forces between the molecules. These forces are mainly "dispersion" forces that result from fluctuations of the charge distribution within the molecules, which can, however, only be derived from quantum theory. Additionally, there may be forces of "orientation" between dipole molecules and forces of "induction" between dipole molecules and dipoleless, yet polarizable molecules. In some fluids hydrogen bonds between the molecules also play a role (valence forces), but these are chemical bonds. As for atoms and molecules in their basic states, molecule forces are always attracting (range of molecule forces).

During evaporation or vaporization of a fluid, the molecules must surmount the van der Waals forces in order to escape the fluid formation. This is caused by thermal motion. Prerequisite for braking away from the formation is a free phase interface, since otherwise the molecule would have no space to elude the attracting forces of the surrounding molecules. Consequently, inside the fluid no evaporation or vaporization can occur unless there are interfaces, too.

The process of vaporization can be instigated either by lowering the pressure or by supplying heat. For every temperature and pressure, a so-called vaporization equilibrium is established, that is an equilibrium between these molecules exiting the fluid and those returning into the fluid. Evaporation will intensify with both increasing temperature and decreasing pressure until a new equilibrium is found. From a certain point on, temperature (boiling point) or pressure (steam pressure) cannot be increased or decreased respectively any further because then the fluid is completely vaporized.

The p, T equilibrium phase diagram shows the transformation curves of a substance's phases with the coordinates pressure and temperature according to the Clausius-Clapeyron equations.

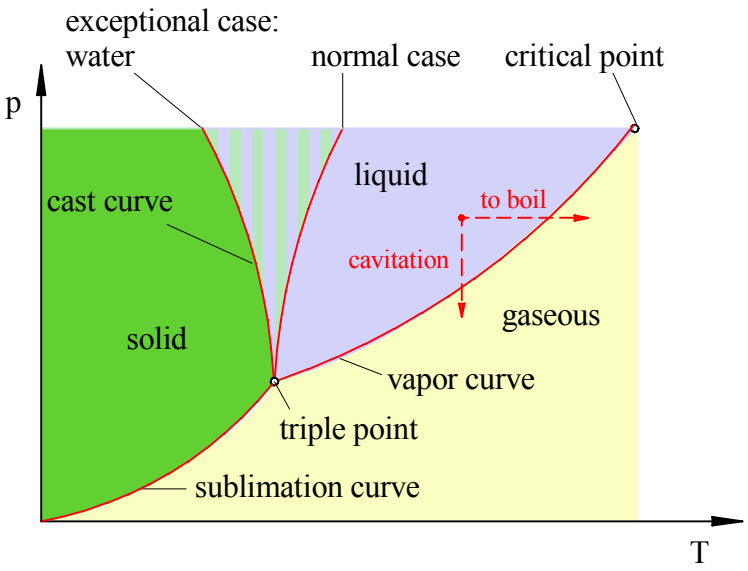

Figure 1.2.1: Phase transformation curves in a p, T diagram after Elsner [1980]

While most substances increase their volume during melting, water (as well as bismuth and gallium) exhibits a different behavior. These substances' solid phases have greater specific volumes than their liquid phases, that is with increasing pressure, the temperature of fusion falls. Thus, an explanation is given that water ice melts under increased pressure at temperatures below 0 °C (see Elsner [1980]).

If there are interfaces inside a fluid, evaporation will also occur there, that is gas bubbles will be formed, rising to the surface. These phase interfaces may be bubbles, incompletely covered particles of suspended matter or incompletely covered container walls, e.g. pores where gas bubbles could be lingering. In case of pressure reduction at constant temperature, particularly in flowing fluids, this process is also called cavitation (lat. cavus = hollow) because, due to their lower density, the gas bubbles become visible against the surrounding fluid. In areas of re-gaining pressure, these gas bubbles disappear, and the vapor condenses abruptly. The induced pressure waves produce a noise with high frequency parts, which is typical for cavitation processes. Flows are characterized according to this phenomenon by the cavitation number σ:

$$\sigma = \frac{p_\infty - p_V}{\frac{\rho}{2} q_\infty^2} \tag{1.2.1}$$

It denotes the pressure difference between the pressure of the unperturbed flow p_∞ and the vapor pressure p_V in relation to the dynamic pressure of the unperturbed inflow q_∞.

However, under absence of free interfaces within the fluid, the transformation curves in the p, T-diagram can be transcended in either direction under certain conditions. For instance, in a suitable container pure water can be heated up to 270 °C at atmospheric pressure.

On the other hand, in case of pressure reduction and under absence of free interfaces, pressure can be reduced below vapor pressure. Using the van der Waals equation, it can be calculated how far this is theoretically possible. Johannes Diderik van der Waals (1837 – 1923) put forward the real gas law, which is called after him. He worked on state equations of gases, vapors and fluids, and in 1910, he was awarded the Nobel Prize in Physics. He described intermolecular forces as interacting forces between molecules with saturated chemical bonds. These are said to be cause

of the existence of fluids and molecule crystals. Intermolecular forces are of electric nature. At very close distances, they act repelling; at farther distances, they are attractive forces. The latter are called van der Waals-forces.

Starting with the ideal gas law, van der Waals developed his equation by adding correcting factors, which he had gained from experiments, for pressure (a) and the molecules' volume (b).

$$\left(p + a\frac{n^2}{V^2}\right)\cdot\left(V - n\cdot b\right) = nRT \tag{1.2.2}$$

This equation makes it possible to explain certain properties of fluids because it bases on the notion of fundamental continuity between gaseous and liquid state. Thus, a fluid is seen as a real gas compressed to a very small volume and that is under the influence of its own inner pressure, caused by cohesion forces between the particles.

The van der Waals-equation is of the third degree, which can easily be seen once it is rewritten:

$$V^3 - V^2\cdot\left(n\cdot b + \frac{R\cdot T}{p}\right) + V\cdot\frac{a\cdot n^2}{p} - \frac{a\cdot b\cdot n^3}{p} = 0 \tag{1.2.3}$$

This equation has three solutions. If the curves for constant temperature, i.e. the isotherms, are drawn, the result is the following picture with the so-called Maxwell-Construction:

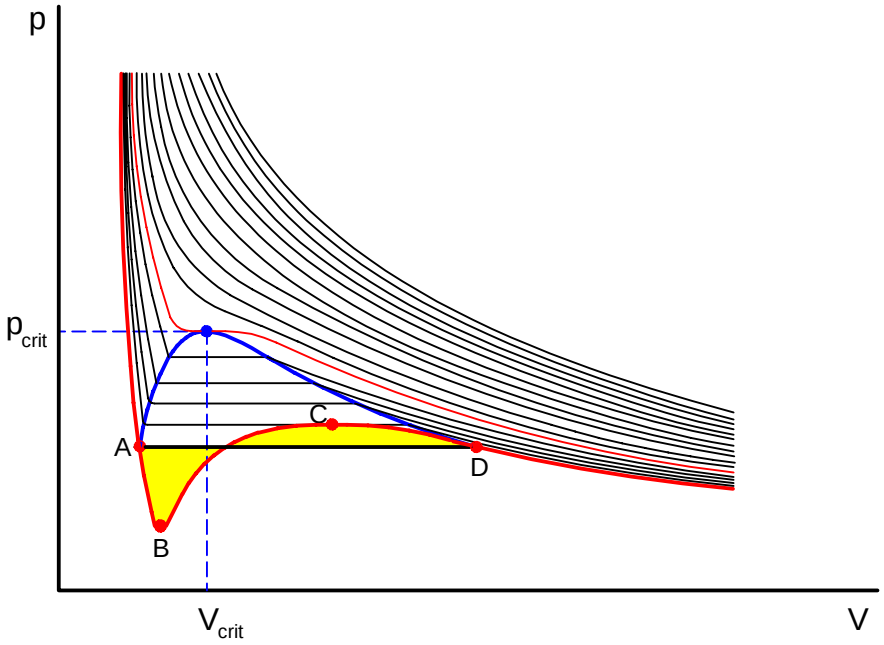

Figure 1.2.2: p, V-diagram for the van der Waals gas with two phase area after 'Thermodynamik und Statistische Physik' (http://uni-bayreuth.de)

The curves' positive slope in some areas indicates that the van der Waals equation cannot be regarded a valid state equation of a substance for all values (p, V) because in these areas the isothermal compressibility would be negative, which cannot occur for a state of thermodynamic equilibrium of a substance. At least in these areas, the p, V-diagram of a substance described by the van der Waals equation must therefore look different. In fact, at compression (decrease of volume), the pressure p of the gas increases until the vapor pressure

of the respective temperature is reached. At further compression, gas condenses to form a liquid, the pressure remaining constant, equal to the vapor pressure. Only when there is merely a little liquid left in the container, will the pressure rise again.

Figure 1.2.2 also shows that a two-phase area, where gas and liquid co-exist, can only be found for temperatures below the so-called critical temperature. The respective isotherm in figure 1.2.2 has been drawn out in red. When this critical temperature is approached, the two-phase area will be contracted to become a single point in the p, V - diagram. Above the critical temperature (critical point), liquid and gas cannot be distinguished any longer. The critical point in the p, V - diagram is marked as an inflection point with horizontal tangent for its respective isotherm. The reason for this are the points B and C (points with horizontal tangent) converging with the inflection point into the critical point. Points on the isotherm in the area between A and B as well as between C and D can be realized as meta-stable states ("overheated fluid" or "under-cooled vapor"). It can be seen that at constant temperature considerable tensile strains may occur.

Due to the instability of intermediate states, which are signified by pressure reduction at decreasing volume (e.g. C-B-A), the real transition from one state into another does not take place on the theoretic isotherm, which corresponds to a uniform liquid-gaseous phase, but on a horizontal isotherm (line A-D) that corresponds to the division of the system into two different phases (liquid and saturated vapor) and the gradual transition from one phase into the other. It is know that this discontinuity in the transition from one state into another only disappears above the critical temperature, where the isotherms become monotone and thus, practically realizable. Near the critical point there is a real similarity between a fluid and a real gas. Also theoretically, hardly any tensile strength can be applied here.

Normally, the isotherm in the transition area is determined by the fact that the two yellow-filled areas must be equal (Maxwell's rule). Only in carefully performed and accordingly prepared (nuclei removal) experiments, the van der Waals-isotherms can partly be realized. If the theoretical tensile strength of pure, homogeneous water is calculated according to the van der Waals-equation by:

$$p = \frac{nRT}{V - nb} - a\left(\frac{n}{V}\right)^2 \tag{1.2.4}$$

orders of magnitude will be gained that may well be appropriate for steel, about 10^4 bar. Of course, this value is only valid for an absolutely homogeneous medium. If thermodynamically caused voids in the quasi-crystalline structure of the water are considered, that is small vapor bubbles due to molecular motion where molecular bonds are weakened, values of strength will be obtained that are lower by about one order, thus about 1000 bar. These are still respectable values of strength. The emergence of small vapor bubbles, also at pressures below the vapor pressure or tensile strains, does therefore not mean that this overheated state of the fluid will collapse immediately through vaporization. Due to the surface tension of the fluid, the bubble is under higher pressure than the surrounding fluid, so for very small vapor bubbles, the fluid is by no means overheated. Therefore, all bubbles below a certain critical size normally disappear again.

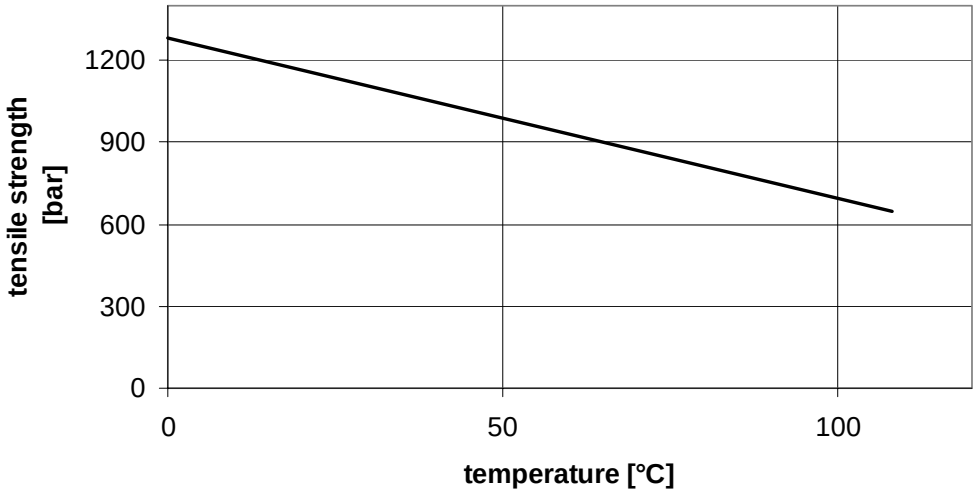

Figure 1.2.3: Theoretical tensile strength of pure water after Keller [1980]

In many particular cases, the probability of nuclei of the new phase being spontaneously created in oversaturated fluids was calculated and thus, the theoretical tensile strength of pure fluids was obtained. For pure water, Keller [1980] calculated the values shown in figure 1.2.3.

Therefore, water should be able to sustain tremendous tensile strains. In reality, however, it does not, as we very well know. To date, the highest tensile strains measured in purest water (distilled several times, degassed) are around 280 bar (see chapter 4.2.4). Figure 4.2.9 illustrates the temperature dependency on the strength of pure water and shows simultaneously one of the many anomalies of water, namely the strong decline of the tensile strength close to the freezing point. The maximum tensile strength was found at 10 °C. Measurements by Keller [1982] also produced a maximum tensile strength at 10 °C for all degrees of gas saturation and system pressures examined (see chapter 4.3.6).

The reason why the theoretical values of tensile strength cannot be obtained in practice may be divers. On the one hand, all techniques of tensile strength measurement of fluids rely on the adhesion forces between the fluid's limits and the fluid itself being greater than the cohesion forces. This is also the reason why the tensile strengths obtained in experiments vary so greatly according to the test method.

Another reason is given by energy-rich cosmic radiation (mostly fast μ-mesons) limiting the maximum tensile strength by inducing gas bubbles in an overheated fluid. In 1960, Donald A. Glaser was awarded Nobel Prize in Physics for his invention of the so-called bubble chamber. This is an ionization detector for low-ionizing particles. The chamber is filled with fluid that is brought to a boil by sudden pressure reduction. As preferred fluid, liquid hydrogen is used. First, the hydrogen is slightly under-cooled at a pressure of 5 to 6 bar until it is completely bubble-free. Due to the pressure being halved within a few milliseconds, the boiling temperature, that is dependant on the pressure, drops. The used fluid's temperature is now above the new boiling temperature. Now, for a few milliseconds, the chamber is sensitive to ionizing particles flying in. Miniature vapor bubbles are formed at the ions because they lose energy due to ionization loss. This effect is used to make the paths of ionizing radiation visible.

2 Diffusion and Bubble Growth

2.1 Basics of Solubility of Gases in Water

2.1.1 Introductory Remarks

The term 'gas' refers to a state of aggregation (phase), in which the energy content of the individual molecules is greater than the bond energy between these molecules. Since both the distance between these molecules and their mutual allocation can be varied freely, it is characteristic to gases to occupy any given space. The phase denomination 'gas' is valid to substance mixtures (air), chemical compounds (CO_2) and elements (O_2).

According to its nature, overheated steam is nothing but a real gas, whereas vapor is a gas that exists in equilibrium with its own liquid phase. The thermal equation of state, which was obtained by methods of statistical thermodynamics and which is valid for an ideal single gas,

$$pV = n \cdot R_G T \tag{2.1.1}$$

can also be applied to a mixture of ideal single gases. According to the Dalton Law, each single gas in an ideal gas mixture will occupy the complete available space of the mixture and will have the partial pressure pn, notwithstanding the remaining gas components in the mixture. The total pressure of a gas mixture p is composed of the individual pressure values, the partial pressures $p_{G,n}$ of the mixture's components.

$$p = p_{G,1} + p_{G,2} + p_{G,3} + \ldots + p_{G,n} \tag{2.1.2}$$

This partial pressure pG will be effective if a given volume V is occupied by only one of the gas' components instead of the whole mixture. By means of the gas laws, which are valid for both pure gases and gas mixtures, the partial pressure p_G of a gas existing in the gaseous phase at a volume concentration V_G/V can be specified as fractional amount of the total pressure p after Boyle – Mariotte:

$$p_G = \frac{V_G}{V} \cdot p \tag{2.1.3}$$

The heat fed to a system is transformed into motion energy of the molecules; the resulting gain of the average speed of the molecules leads to an increase of the gas pressure. If a system consists of various substances in different mass proportions – all in the same phase –, it shall be named a solution or mixture.

2.1.2 Solubility

Gases react chemically with water; thus, for instance, CO_2 combines with water to form carbonic acid H_2CO_3. However, certain parts of the gases also mix with water molecularly; they dissolve at certain conditions to a degree, at which there are exactly as many gas molecules entering the water from the gas body as leaving the water at its surfaces. This state is characterized by the saturation value of the solution.

In 1803, William Henry (1775-1836, factory owner in Manchester) found that at sufficient dilution the 'vapor pressure' of a solute is proportional to its concentration in the solution.
At constant pressure, the solubility (saturation concentration) c_s of a gas is proportional to the partial pressure pG of the gas being in gas phase above the fluid.

$$c_S = k \cdot p_G \tag{2.1.4}$$

Of course, this law can also be given using the ideal gas law,

$$p \cdot V = n \cdot R \cdot T \tag{2.1.5}$$

n - number of moles R -gas constant
T - absolute temperature

as well as using the known volume proportion V_G/V of the gas in a mixture above the fluid:

$$c_S = k \cdot n' \cdot R \cdot T \cdot \frac{V_G}{V} \tag{2.1.6}$$

n' - number of moles per volume unit.

Instead of the proportional factor k, the adsorption coefficient α after Robert Wilhelm Bunsen (1811-1899) is applied, which specifies the gas volume soluble in the volume unit of the fluid at a partial gas pressure of 760 mmHg (converted to norm conditions: 0°C, 760 mmHg).
If water is used as a solvent, the gas space near the water surface can be considered saturated with water vapor. Therefore, it is useful to define α as the total pressure p = 760 mmHg, that is the partial pressure of the gas $p_G + p_V$.
The following table 2.1.1 after Hodgman [1957] gives the adsorption coefficient α for the gas mixture air, which is of special interest here, dissolved in water:

T [°C]	00	05	10	15	20	25	30
α [‰]	29,18	25,68	22,84	20,55	18,68	17,08	15,64

Table 2.1.1: Absorption coefficient α [Ncm³ gas/1000 cm³ H_2O] for air (free from CO_2, NH_3) dissolved in water at a total pressure $p = p_G + p_V = 760$ mmHg.

In practice, the saturation concentration c_s of gases dissolved in fluids is therefore determined by the relation:

$$c_S = \alpha \frac{p}{760} \tag{2.1.7}$$

Henry's law is exact only for infinitely diluted solutions and low pressures. This is coherent considering that in a solution the properties of the descrete components have already changed. So, gas molecules entering the solution at a later stage are not confronted with the pure solvent any more, but already with the solution. Within the scope of the following explications and applications, this law will, however, provide sufficient accuracy.

By specifying the adsorption coeffient α according to table 2.1.1, it is assumed that the gas mixture air in its known composition (20,9 vol% oxygen, about 78 vol% nitrogen, about 1 vol% noble gases) permeates the water. The partial pressure $p_{G,n}$ of each single gas in the mixture as well as its particular adsorption coefficient determine the saturation concentration $c_{S,n}$ of a solution. Only the sum of these values – at known environmental conditions – provides the sought adsorption coefficient α of the gas mixture air.

Thus, considering the equilibrium of air and water, it appears that the portion of diluted oxygen in the total gas content rises above the known value of 21%. Despite its low atmospheric partial pressure of $p_{G,O2}$ = 0.21atm, the share of dissolved oxygen lies between 34.91% (0°C) and 33.60% (30°C), due to its high solubility (e.g. see Keller [1973]).

Nowadays, the following notation is also used for practical applications of Henry's law:

$$c_S = \frac{p_G}{H(\vartheta)} = \left(\frac{V_G}{V}\right)_S \tag{2.1.8}$$

with $H(\vartheta)$ - Henry coefficient..

From these perceptions, as an area of problems the necessity arises to separately identify the degree of saturation of a solution enriched with gas mixtures according to the individual components and their respective partial pressures in the actual gas phase.

2.1.3 Degree of Saturation

The pressure commonly correlated to the concentration c of the diluted gas is the total pressure of all gases above the fluid. For a gas volume in the fluid, the correlated pressure is the gas pressure in this cavity. The gas pressure is dependent on the size and geometry of the gas inclusion. Regarding its gas, the solution may therefore be either under- or oversaturated, or also fully saturated.

Here, the customary definition of the saturation degree f, with the atmospheric pressure as correlated pressure, loses its importance. The degree of saturation is defined as the ratio of the existing concentration c and the saturation concentration c_S at a given pressure above the fluid. With the total pressure in a nucleus of any shape, the saturation concentration is:

$$c_S = \alpha \cdot (p_{Fl} + 2S/R - p_V) \tag{2.1.9}$$

with: S - surface tension ; p_V - partial pressure of the vapor.
Thus, the degree of saturation is specified by

$$f = \frac{c}{c_S} = \frac{c}{(p_{Fl} + 2S/R - p_V) \cdot \alpha} \tag{2.1.10}$$

where $f < 1$ stands for an undersaturated, $f = 1$ for a saturated and $f > 1$ for an oversaturated solution compared to a nucleus with the radius R.
For $f < 1$, due to $c < c_s$, gas will diffuse into the fluid, whereby the saturation concentration of the nucleus increases as a result of the radius decreasing and the nucleus quickly dissolving. At $f > 1$ gas will diffuse from the oversaturated fluid into the nucleus, which expands beyond measure due to the capillary pressure. The equilibrium radius R_{Gl} for $f = 1$ is

$$R_{Gl} = \frac{2 \cdot S}{\frac{c}{\alpha} - p_{Fl} + p_V} = \frac{2 \cdot S}{c \cdot H(\vartheta) + p_V - p_{Fl}} \tag{2.1.10}$$

A simple measure to produce an oversaturated solution is therefore to reduce the gas pressure above a saturated solution: the saturation concentration $c_{S,2}$ corresponding to the new reduced pressure is lower than the existing concentration $c_{S,1}$ of the gases diluted in the fluid. If the saturation pressure corresponding to the respective gas content is identified with p_S and the arbitrary existing partial pressure of a gas is identified with p_G, the following cases can be distinguished:

a) $p_S = p_G$ - state of equilibrium
b) $p_S < p_G$ - undersaturation
c) $p_S > p_G$ - oversaturation

For example, in water circulation tunnels, all these states of saturation may occur. Oversaturated, dissolved gas diffuses from the fluid into small bubbles within the fluid volume or into the gas phase above the fluid's surface.

2.2 Nuclei

2.2.1 Introductory Remarks

If it can be achieved by filtration to rid a fluid of all impurities, with gradual pressure reduction the appearance of small bubbles, growing with progressing saturation, at the container walls can be observed. The diluted gas diffuses into minute gas inclusions within the clefts of the walls. Interfaces between the two phases are therefore the pre-condition for the segregation of diluted gases. Microscopically minute gas volumes, which are present in these areas and are therefore triggering the gas segregation, are denominated nuclei. They represent small inhomogeneities in the water where molecular forces are being disturbed and thus, the quasi-crystalline structure of the water is weakened.

The existence of nuclei is always a prerequisite for a change of phase. Boiling nuclei, responsible for the boiling of fluids, represent the most well-known example. Under the absence of such boiling nuclei, water can be heated far above its boiling point without vaporization. As shown in figure 1.2.1, the steam curve (or steam pressure curve) represents the so-called line of co-existence between gaseous and liquid phase. However, a phase may also be existent (metastably) beyond that line of co-existence in points of state belonging to the other (stable) phase. As was proven, within a pure phase, which has become metastable after transition, the other phase stably corresponding to the newly reached state is not continuously formed immediately beyond the co-existence line. On the contrary, the line is normally rather significantly transited. For instance, in pure steam being under-cooled by adiabatic expansion the temperature exceedance may reach 30 K and more before nuclei of the liquid phase are starting to form as minute droplets. This process is called homogeneous condensation or homogeneous nucleus formation. Conversely, in case of an over-heated fluid it is called homogeneous evaporation.

It is different if the phase, when transiting the co-existence line, is already of homogeneous structure, that is steam already bearing droplets of water with air or steam nuclei. In this case, the co-existence line is normally merely slightly transited and the new phase is formed around the already existent nuclei. This process is called inhomogeneous or heterogeneous condensation or vaporization respectively (nucleus formation). According to the theory of equilibrium steam pressure, an already existing free surface is assumed. However, if a homogeneous fluid exists, it must first be broken up. For this process tensile stresses, that is negative pressures, are needed, which are not in direct correlation with the steam pressure. The probability that in a homogeneous fluid a new expandable phase is formed after transition of the co-existence line is calculated by means of methods of statistical thermodynamics (see e.g. Isay [1989] and Keller [1980]).

Possible types of nuclei, filled with non-condensable gas (air) or condensable water vapor, are free gas nuclei, pore nuclei at floating particles and pore nuclei at walls. A sudden pressure reduction results in an immediate expansion of the fluid volume, thus, accelerating the individual fluid particles toward the open water level. Cohesion forces within the fluid and adhesion forces at the container walls counteract this movement. As a result, there are negative pressure values that overlay the applied reduced pressure and therefore heavily oversaturate the fluid. Consequently, in the fluid there is molecular movement that facilitates gas diffusion from the fluid into the nuclei.

The effective degasification of a fluid is only possible if a constant interface exchange is guaranteed. Energy is needed for this purpose, keeping the two-phase system is agitated or maintained in turbulent flowing motion (Kuz [1971]).

2.2.2 Bubble Nuclei

(2.2.2 – 2.2.5 after Stiedinger u. Stoffel [2000])

When considering bubble nuclei of air in resting fluids, one must examine their stabiltiy and behavior at changing environmental conditions.

According to Eqn. (2.1.7) the saturation equilibrium is:

$$c_S = \frac{p_G}{H(\vartheta)} \tag{2.2.1}$$

On the gaseous side of the interface there is the pressure $p=p_G+p_V$, with the partial pressure of water vapor $p_V(\vartheta)$ and the partial pressure of the gas above the fluid p_G.
For the system water-air one can approximately apply:

$$H(\vartheta) = (0{,}346 + 0{,}00927 \cdot \vartheta) \left[\frac{\text{bar}}{\text{vol\%}}\right] \tag{2.2.2}$$

with temperature ϑ.

As described in chapter 2.1.2, the compostion of dissolved air changes because of the different solubility of its components O_2 and N_2. If the solution's equilibrium is disturbed, under- or oversaturated solutions will develop, specified by the degree of saturation $f = c/c_S$. The concentration gradient at $f \neq 1$ is perpendicular to the interface where full saturation is found. The transportation velocity of the dissolved substance is determined by the diffusion coefficient D and the concetration gradient dc/dn of the system (see chapter 2.3.1.). The transportation direction is determined by the degree of saturation with diffusion from the gas into the fluid and vice versa being completed when $c_\infty = c_S$ is reached (c_∞ – saturation concentration at far distance from the bubble).

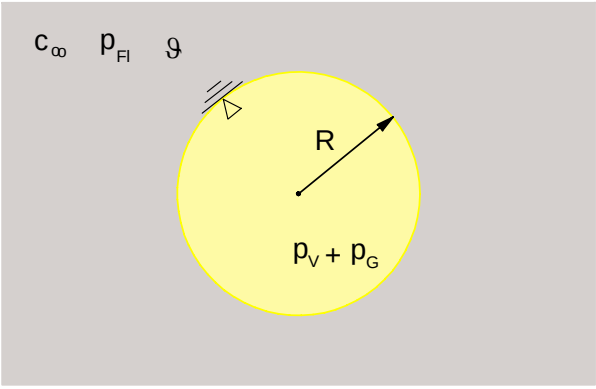

Figure 2.2.1: Equilibrium radius of spherical nuclei

The equilibrium radius of a spherical bubble nucleus, assuming pressure equilibrium

$$p_i = p_G + p_V = p_{Fl} + \frac{2 \cdot S}{R} \tag{2.2.3}$$

with: p_i pressure inside the bubble and $c_\infty = c_S = \text{const.}$ is then calculated by:

$$R_{Gl} = \frac{2 \cdot S}{c_\infty \cdot H(\vartheta) + p_V(\vartheta) - p_{Fl}} = f(\text{liquid, gas, } p_{Fl}, \vartheta). \tag{2.2.4}$$

Regarding water at 20°C and 1bar, there are equilibrium radii in the order of $R_{GL} \approx 0{,}06$mm. Necessary substance values such as $p_V(\vartheta)$ und $s(\vartheta)$ of water can be found in Wagner & Kruse [1998] or D'Ans & Lax [1992].

According to eqn. (2.2.3), the surface tension s causes a pressure difference $p_i - p_{FL}$, which means that the internal bubble pressure is always higher than the pressure of the fluid. Consequently, the assumption $c_\infty = c_S = \text{const.}$, under the precondition of pressure equilibrium after eqn. (2.2.3), can hardly be held. Accordingly, at a pressure increase of $\Delta p_{Fl} \geq 0$ there is always an unbalance of the solution (undersaturation), which results in the bubble nuclei completely being dissolved or resorbed. The higher Δp_{Fl} and the smaller the bubble is, the faster this process will be.
For $\Delta p_{Fl} < 0$ the fluid is oversaturated, which leads to bubble growth by gas diffusion from the fluid into the bubble. The thereby increasing buoyancy results in a constant buoyant acceleration of the bubbles at

$$u_A = \frac{2 \cdot g \cdot R_{Bl}^2}{9 \cdot \upsilon}, \tag{2.2.5}$$

until the gas bubbles finally exit and the fluid degasses. The process can be observed especially well at the example of a freshly opened bottle of champagne or mineral water. After a longer time the bubbles disappear almost completely as described above. Therefore, it can be concluded that spherical air bubble nuclei cannot exist in resting fluids over a longer period of time. In flows, the time for the diffusion at varying pressure differences is decisive for these bubbles' existence.
However, also after even a very long resting time bubbles visibly exist in a water glas. It will now be explained why not all the bubbles disappear.

2.2.3 Pore Nuclei

Stable states of bubbles are also possible für saturation degrees f < 1, namely when the surface stress works towards the water. This is the case when the gas nuclei are in clefts or impressions of the solid flow bounds or dirt particles. Various geometrical shapes of these pores may occur. Basically, they can be of spherical or conical shape, and they must behave hydrophobicly toward the fluid (see figure 2.2.2). The resulting contact angle Θ depends on the ratio of molecular forces within the fluid and those between the fluid and the boundaring solid substance. At insufficient wetting (hydrophob) the molecular forces within the fluid are stronger than the forces between fluid and wall (Keller [1973]; Morch [1986]; Skarsoulis [1988]).

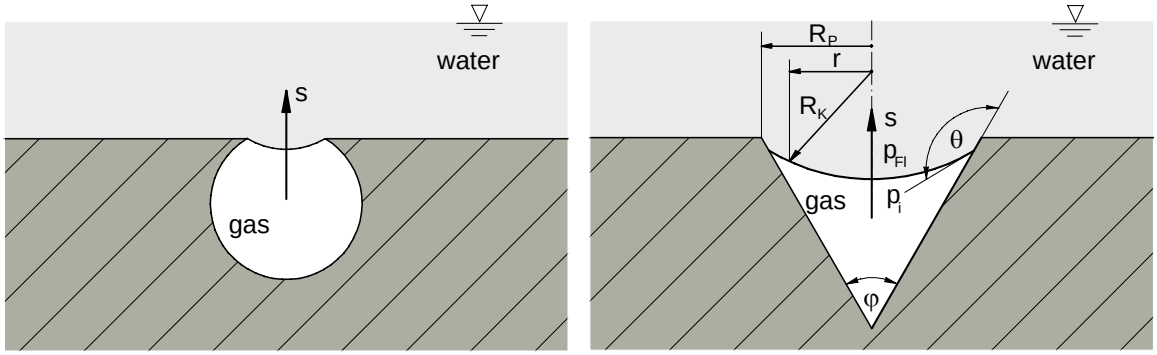

Figure 2.2.2: Geometry of pore nuclei after Harvey [1945]

Resuting from the geometry of a spherical pore nuclui, the curve radius R_K at a constant contact angle is the larger, the bigger the included gas volume is. This is valid until the interface reaches the border of the pore nucleus. A stability assessment of this type of nucleus shows that at incresing pressure the fluid is undersaturated and therefore, gas diffuses into the fluid. The pressure equilibrium is:

$$p_i = p_G + p_V = p_{Fl} - \frac{2 \cdot S}{R_K} \qquad (2.2.6)$$

with: $$R_K = \frac{r}{\left|\cos\left(\Theta - \frac{\varphi}{2}\right)\right|} \qquad (2.2.7)$$

Consequently:

$$R_{Gl} = \frac{2 \cdot S \cdot \left|\cos\left(\Theta - \frac{\varphi}{2}\right)\right|}{p_{Fl} - p_V - c_\infty \cdot H(\vartheta)} \qquad \text{where: } R_{Gl} = R_p \qquad (2.2.8)$$

At a smaller nucleus volume and a smaller curve radius the gas pressure is descreasing and a new equilibrium is established.
Equally, a decreasing pressure leads to a new equilibrium and a new interface is established until r = R_P. When this „critical“ bubble radius is exceeded, the bubble will detach itself from the wall. Therefore, one can see that nuclei can exist in resting fluids over a long time, if they are bound in indentations. If the fluid transits to flow, these pore nuclei can swim off as micro-bubbles.

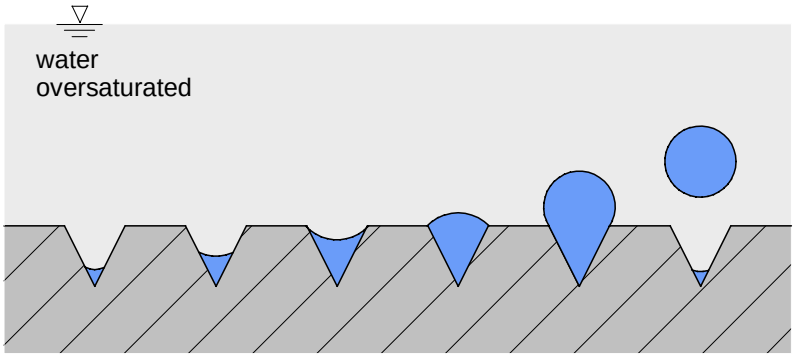

Figure 2.2.3: Growth of a nucleus in an oversaturated fluid through pressure reduction

2.2.4 Quasi-static Nucleus Behavior

The behavior of nuclei without the influence of diffusion is considered. Here the temporal pressure changes dp/dt respectively $c \cdot \partial p/\partial s$ are so quick that, despite solution equilibrium being disturbed, the gas mass in the nucleus remains approximately constant.
A spherical nucleus is considered. The behavior of these bubble nuclei disregarding diffusion can be described fairly easily under certain conditions:
- gas mass in the nucleus remains m_G = const., that is diffusion is not considered
- inertia forces of the displaced fluid are disregarded, valid for dR/dt small
- heat supply is very quick or a constant temperature within the fluid;

$$p_V = \text{const.}, \vartheta_G = \text{const.}$$

Applying the ideal gas law, the pressure equilibrium is:

$$p_{Fl} - p_V = \frac{p_{G0} \cdot R_0^3}{R^3} - \frac{2 \cdot S}{R} \tag{2.2.9}$$

with: $R = f(p_{Fl} - p_V)$
The stability limit compared to pressure lowering is:

$$\frac{dR}{d(p_{Fl} - p_V)} \to \infty \text{ respectively } \frac{d(p_{Fl} - p_V)}{dR} = -3\frac{p_{G0} \cdot R_0^3}{R^4} + \frac{2 \cdot S}{R^2} \stackrel{!}{=} 0. \tag{2.2.10}$$

Thus, the critical bubble radius is determined by:

$$R_{krit} = \sqrt{\frac{3}{2}\frac{p_{G0} \cdot R_0^3}{S}} \tag{2.2.11}$$

By inserting (2.2.11) into (2.2.10), the citical pressure is obtained:

$$(p_{Fl} - p_V)_{krit} \cdot R_{krit} = \frac{p_{G0} \cdot R_0^3}{R_{krit}^2} - 2 \cdot S = -\frac{4}{3} \cdot \frac{S}{R_{krit}} < 0. \tag{2.2.12}$$

One can see that for $4/3\ S/_{Rkrit} > p_V\ R_{krit}$ the stability limit is within the order of tensile stresses (see chpt. 4), because then it is $p_{Fl,krit} < 0$.
As correlation between R_{krit} and R_0 one gets with

$$p_{G0} = p_0 - p_V + \frac{2 \cdot S}{R_0} \tag{2.2.13}$$

and with (2.2.11):

$$R_{krit}^2 = \frac{3}{2}\frac{p_{G0} \cdot R_0^3}{S} \tag{2.2.14}$$

it follows: $$\frac{R_{krit}}{R_0} = \sqrt{3 \cdot \left[\frac{(p_0 - p_V) \cdot R_0}{2 \cdot S} + 1 \right]}. \qquad (2.2.15)$$

Resulting for the critical pressure difference:

$$(p_{Fl} - p_V)_{krit} = -\frac{4}{3} \cdot \frac{S}{R_{krit}} = -\frac{4}{3} \cdot \frac{S}{R_0} \cdot \frac{R_0}{R_{krit}} \qquad (2.2.16)$$

respectively $$(p_{Fl} - p_V)_{krit} = -\frac{4}{3} \cdot \frac{S}{R_0} \cdot \frac{1}{\sqrt{3 \cdot \left[\frac{(p_0 - p_V) \cdot R_0}{2 \cdot S} + 1 \right]}} \qquad (2.2.17)$$

This means that the critical pressure difference $(p_{Fl} - p_V)_{krit}$ is dependent on the nucleus' size, the fluid and the distance of vapor at the place of reference. Considering water at $p_0 = 10^5\,\text{Pa}$, $\vartheta = 20°\text{C}$, $p_V = 2350\,\text{Pa}$ and $S = 7{,}3 \cdot 10^{-2}\,\text{N/m}$, tensile stresses result for nucleus sizes of $R_0 < 9 \cdot 10^{-6}\,\text{m}$. For nucleaus sizes $R \approx 5 \cdot 10^{-5}\,\text{m}$ the value of the critical pressure matches that of water vapor.

2.2.5 Dynamic Nucleus Behavior

For the temporal change of the bubble radius one can assume a differential equation in its simplest form by Rayleigh (1917), who first considered the empty bubble with $p_i = 0$. Later, however, he also included the gaseous contents of the bubble. This differential equation, today known as Rayleigh-Plesset Equation, has been amended for the influence of certain parameters by various researchers (see section 2.3) One way of deriving it could be that the change of bubble size is connected with the change of kinetic energy of the surrounding fluid. It is in equilibrium with the potential energy. With the assupmtions:
- unperturbed spherical single bubble;
- gas mass m_G = const; i.e. no diffusion;
- known temporal change of pressure $p_\infty = p_\infty(t)$ in far distance from the bubble;
- friction-free, incompressible fluid;
- neglegtable enthalpy of evaporation

the potential energy of the bubble, because of the pressure difference in far distance and at the bubble's bordering, is:

$$\frac{dE_{pot}}{dt} = \frac{dE_{pot}}{dR} \cdot \frac{dR}{dt} = (p_\infty - p_{Fl,W}) \cdot 4\pi R^2 \cdot \dot{R}. \qquad (2.2.18)$$

The kinetic energy within the fluid, neglecting the kinetic energy of the gaseous contents of the bubble, is:

$$\frac{dE_{kin}}{dt} = 2\pi \cdot \rho_{Fl} \cdot \left(2 \cdot R^3 \cdot \dot{R} \cdot \ddot{R} + 3 \cdot R^2 \cdot \dot{R}^3 \right) \qquad (2.2.19)$$

With:

$$\frac{dE_{pot}}{dt} = -\frac{dE_{kin}}{dt} \text{ (friction-free)} \qquad (2.2.20)$$

the Rayleigh-Plesset Equation can be deduced to:

$$R \cdot \ddot{R} + \frac{3}{2} \cdot \dot{R}^2 = \frac{1}{\rho_{Fl}} \cdot \left(p_{Fl,W} - p_\infty \right) \tag{2.2.21}$$

It is a non-linear, ordinary differential equation with:

$$p_{Fl} = p_V + p_G - \frac{2 \cdot S}{R}$$

The gas pressure is:

$$p_G = \left(\frac{V_0}{V} \right)^2 \cdot p_{G0} = \left(\frac{R_0}{R} \right)^{3n} \cdot p_{G0} \tag{2.2.22}$$

with n = 1isothermic change of the gas
n = κ adiabatic change of the gas

and: $p_{G0} = p_0 + \frac{2 \cdot S}{R_0} - p_V$

Notably, the assumption of no diffusion occuring at pressure changes is unrealistic for many technical applications. That is why these processes shall be discussed further in section 2.3.

2.3 Influence of Diffusion at Pressure Changes

2.3.1 Introductory Remarks

In flows variations of the fluid pressure occur, which changes the state of saturation of the fluid surrounding the bubbles or nuclei.
Diffusion is defined as the transition of a chemical substance through a solvent or of a gas through a mixture of other gases. This motion is caused by the concetration difference of the diffusing substance within the solution or the mixture. In order to be able to solve the diffusion equation, boundary conditions must be defined, preferably being justified by acknowledged results of measurement.

Particularly in pressure changing fields, bubble oscillations lead to so-called “directed” diffusion from the gas dissolved in the fluid into the bubble. The reason is that at a constant diffusion coefficient, the bubble surface is changing depending on the pressure and thus, the gas mass per time unit diffusing into the bubble at low pressure is greater than the gas mass diffusing from the bubble into the fluid at high pressure. Under such conditions, a bubble will grow due to directed diffusion while this growth will yet be accelerated because of constantly decreasing surface tension. Subsequently, a number of important authors and their publications will be presented.

2.3.2 Differential Eqution for Bubble Growth by Kuz

Kuz [1971] describes bubble growth as follows. If the center of a resting gas bubble is chosen as origin of a steric polar coordinate system, the concentration of diluted gas c at a certain point in the solution with the distance r from the origin at any time t is calculated, after concentration equilibrium has been established for the molecular layer (t > 0) (see Matai [1954]), by the following diffusion equation:

$$\frac{\partial c}{\partial t} = D \cdot \frac{\partial^2 c}{\partial r^2} \tag{2.3.1}$$

In addition to (2.3.1) and with the help of the diffusion constant D, the mass of the gas diffusing into the bubble per time unit can be specified by:

$$\frac{d_m}{dt} = A_B \cdot D\left(\frac{\partial c}{\partial r}\right)_R \tag{2.3.2}$$

In order to calculate the volume increase of a gas bubble caused by diffusion, it is necessary to derive the value $(\partial c/\partial r)_R$ from (2.3.1). In case that the diffusing substance's own volume is small compared to the solvent's, the construction of the diffusion equation (2.3.1) is concordant with the differential equation for heat propagation. This analogy allows the examination of diffusion processes with the help of formulas and methods provided by the solutions of problems of heat transfer. Epstein [1950] used this analogy for solving the equation (2.3.1):

$$\left(\frac{\partial c}{\partial t}\right)_R = (c_0 - c_s)\left(\frac{1}{R} + \frac{1}{\sqrt{\pi \cdot D \cdot t}}\right) \tag{2.3.3}$$

The state of a gas bubble with the radius R under the influence of the static pressure p of the fluid and the pressure caused by surface tension 2S/R (S – surface tension) is described by the equation:

$$p + \frac{2S}{R} = \frac{n \cdot R_G \cdot T}{V_B}$$

$$p + \frac{2S}{R} = \frac{R_G \cdot T}{M} \cdot \rho(R) \tag{2.3.4}$$

with:

R_G	- gas constant
T	- absolute temperature
n	- number of mole
V_{Blase}/n	- mole volume
M	- molecular weight
$\rho(M)$	- density of the gas

Considering that

$$m = \frac{4\pi}{3} R^3 \cdot \rho(R) \tag{2.3.5}$$

specifies the mass of the gas bubble, with (2.3.4) the temporal change of this mass dm/dt at a variable radius R results in:

$$\frac{dm}{dt} = 4\pi R^2 \frac{dR}{dt}\left[\rho_{(\infty)} + \frac{4}{3}\frac{M \cdot S}{R_G \cdot T} \cdot \frac{1}{R}\right] \tag{2.3.6}$$

$\rho_{(\infty)}$ - density of the gas, if $R = \infty$.

The gas mass diffusing into the bubble was also described with (2.3.2), (2.3.3). This identity of (2.3.2) and (2.3.6) finally leads to the differetial equation of the bubble radius R:

$$\frac{dR}{dt} = \frac{D(c_0 - c_s)}{\rho_{(\infty)} + \frac{4}{3}\frac{M \cdot S}{R_G \cdot T} \cdot \frac{1}{R}}\left(\frac{1}{R} + \frac{1}{\sqrt{\pi \cdot D \cdot t}}\right) \tag{2.3.7}$$

With some mathemetical effort the function R(t) can be derived and evaluated for the saturation value $f_0 \leq 1.00 \geq f_0$.
For some characteristic values f_0, table 2.3.1 shows the times t_{10,R_0} for the growth of gas bubble until ten times their initial radius R_0 due to diffusion. For comparison, table 2.3.1 also shows the growth times t'_{10,R_0} of gas bubbles without the effect of the surface tension s.

	$R_0 = 10^{-3}$ cm		$R_0 = 10^{-2}$ cm	
f_0	t_{10,R_0} [s]	t'_{10,R_0} [s]	t_{10,R_0} [s]	t'_{10,R_0} [s]
1,25	567	496	$501 \cdot 10^2$	$496 \cdot 10^2$
1,50	266	248	$249 \cdot 10^2$	$248 \cdot 10^2$
1,75	174	165	$166 \cdot 10^2$	$165 \cdot 10^2$
2,00	129	124	$124 \cdot 10^2$	$124 \cdot 10^2$
5,00	32	31	$31 \cdot 10^2$	$31 \cdot 10^2$

Table 2.3.1: Growth times of gas bubbles from R_0 to $10 \cdot R_0$ due to gas diffusion after Epstein & Plesset [1950]

The solution of differential equation (2.3.7) with the isocline method and the following values, considering a step $\Delta t = 1s$ and the initial radius R = 10^{-5}, results with:

$D = 2\ 10^{-9}\ m^2/s$; $T = 293\ K$; $\varrho = 1{,}205\ kg/m^3$
$R_G = 8314\ J/kMol\ K$; $M = 28{,}96\ kg/kMol$
$S = 0{,}0725\ N/m$; $\Delta c = c_S\ (f_0 - 1) = 18{,}68 \cdot 4 \cdot 10^{-3}$
$f_0 = c_0/c_S = 1{,}25 \ldots 5 = 5$ dialed; $c_S = \alpha \cdot p/760\ mmHg$
$\alpha = 18{,}68 \cdot 10^{-3}$ bei $p = 760\ mmHg$

in the bubble growth shown in diagram (2.3.1).

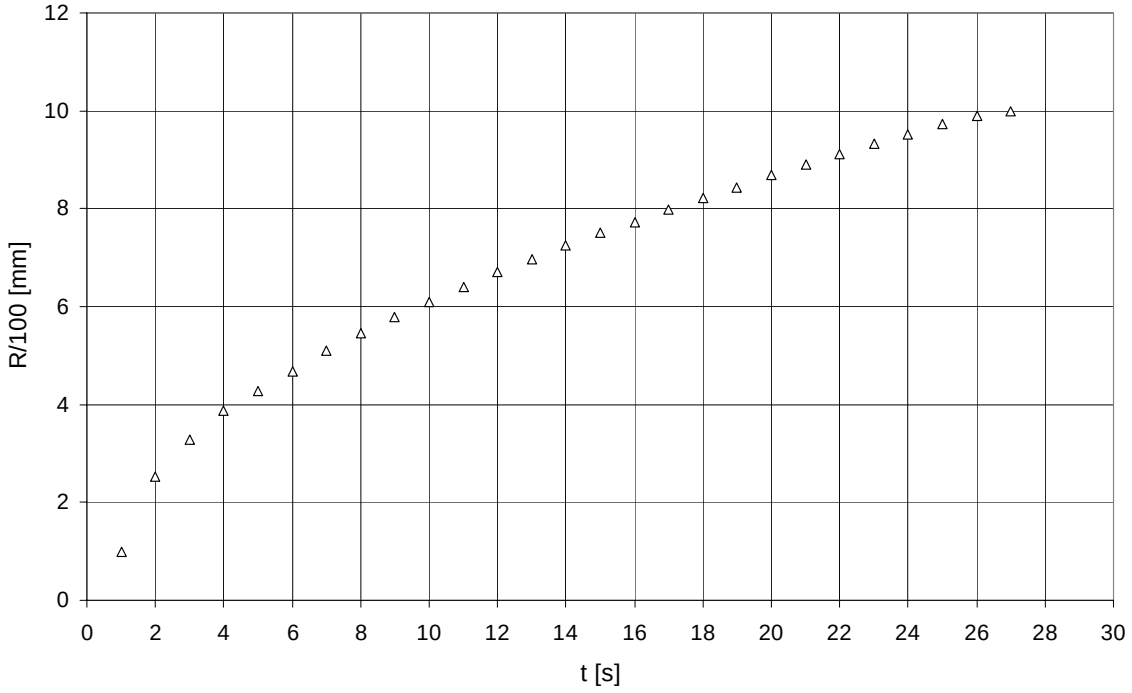

Diagram 2.3.1: Bubble growth for $f_0 = 5$ after equation (2.3.7)
(calculation by Heller [1995])

At $f_0 = 5$ (heavy oversaturation) the bubble has reached the tenfold radius after 27 seconds. These remarkably long times can be explained by diffusion of the dissolved gas being in resting water; so, concetration exchange is not facilitated by turbulent mixing.
Table 2.3.1 shows that the growth times are almost identical, no matter whether the surface tension is effective or not.

$$R'^2 = R_0^2 + \frac{2D \cdot (c_0 - c_s)}{\rho} \cdot t \tag{2.3.8}$$

Manley [1960] was able to show in experiments that after a short initiation phase with low bubble growth, (2.3.8) in the form of:

$$\frac{R'^2 - R_0^2}{t} = \frac{2D \cdot (c_0 - c_s)}{\rho} = \text{konst.} \tag{2.3.9}$$

describes precisely the bubble growth as a fuction of time and therefore, neglegting the surface forces in theoretical discussion is legitimate, in case $R_0 \geq 10^{-3}\,cm$. Furthermore, he proved that (2.3.8) also describes the temporal collapse of an air bubble in an undersaturated solution, as long as the bubble radius is larger than 0.5 mm. In the following final phase the diffusion coefficient D is decreased due to a aggregation of dirt particles at the bubble wall.

2.3.3 Diffusion Equation for Bubble Growth by Kümmel

Already Epstein. Plesset [1950] considered bubble behavior in under- and oversaturated as well as saturated solutions. According to them, in case of a resting and slowly growing bubble, for the concentration gradient $(\partial c/\partial r)_{Ra}$ at the phase interface of a spherically symmetric bubble, the following relation results:

$$\left.\frac{\partial c}{\partial r}\right|_R = \Delta c \cdot \left[\frac{1}{R} + (\pi \cdot D \cdot t)^{-1/2}\right] \cdot \rho_G \tag{2.3.10}$$

Δc is the difference between the given gas concetration c of the solution in far distance from the bubble and the saturation concentration c_S, determined by the gas pressure inside the bubble; ϱ_g is the gas density.
The temporal mass flow through the phase interface O at a given diffusion coefficient D can be determmined by:

$$\frac{dm}{dt} = A \cdot D \cdot \left(\frac{\partial c}{\partial t}\right)\Bigg|_R$$

Using (2.3.10), this equation can be derived to:

$$\frac{dm}{dt} = 4\pi R^2 \cdot D \cdot \Delta c\left[\frac{1}{R} + (\pi D t)^{-1/2}\right] \cdot \rho_G \tag{2.3.11}$$

With the relation: $\Delta c = c - c_s = c - \alpha\left(p_{Fl} - p_V + \frac{2S}{R}\right)$

(2.3.11) becomes:

$$\frac{dm}{dt} = 4\pi R^2 \cdot D \cdot \rho_G\left[c - \alpha\left(p_{Fl} - p_V + \frac{2S}{R}\right)\right] \cdot \left[\frac{1}{R} + (\pi \cdot D \cdot t)^{-1/2}\right] \tag{2.3.12}$$

The gas mass m within a bubble is:

$$m = \frac{4}{3}\pi \cdot R^3 \cdot \frac{p_G}{R_G \cdot T}$$

and the change of mass over time is:

$$\frac{dm}{dt} = \frac{4\pi}{R_G \cdot T} \cdot \left(3R^2 \cdot p_G \cdot \frac{dR}{dt} + R^3 \cdot \frac{dp_G}{dt} \right) \tag{2.3.13}$$

With the equation of force equilibrium of a spherically symmetric bubble

$$\pi R^2 (p_{Fl} - p_i) + 2\pi RS = 0 \; ; \quad p_i = p_G + p_V$$
$$\frac{dp_G}{dt} = \frac{dp_{Fl}}{dt} - \frac{2S}{R^2} \cdot \frac{dR}{dt} \tag{2.3.14}$$

Inserting (2.3.14) in (2.3.13), this makes:

$$\frac{dm}{dt} = \frac{4\pi}{R_G \cdot T} \cdot R^2 \left(p_{Fl} - p_V + \frac{4S}{3R} \right) \frac{dR}{dt} - \frac{R}{3} \cdot \frac{dp_{Fl}}{dt} \tag{2.3.15}$$

This equation describes the temporal change of mass due to the temporal change of radius dR/dt and the temporal change of the fluid pressure dp_{Fl}/dt. Equating the two equations (2.3.12) and (2.3.15) describing the mass change eventually results in:

$$\frac{dR}{dt} = \frac{\rho_G \cdot R_G \cdot T \cdot D \left[c - \alpha \left(p_{Fl} - p_V + \frac{2S}{R} \right) \right] \cdot \left[\frac{1}{R} + (\pi Dt)^{-1/2} \right] - \frac{R}{3} \cdot \frac{dp_{Fl}}{dt}}{p_{Fl} - p_V + \frac{4S}{3R}} \tag{2.3.16}$$

This non-closed solvable differential equation describes the temporal motion of a bubble surface due to diffusion and pressure lowering.

Applying the isocline method with the following values:

$\Delta t = 1s$; $R = 10^{-5}$ m; $dp_{Fl}/dt \rightarrow 0$
$D = 2\ 10^{-9}$ m²/s; $T = 293$ K; $\varrho = 1{,}205$ kg/m³
$R_G = 287$ Nm/kg K; $p_{Fl} = 10^5$ N/m²; $p_V = 0{,}0241 \cdot 105$ N/m²
$S = 0{,}0725$ N/m; $\Delta c = c - \alpha(p_{Fl} - p_V + 2S/R) = c_S\ (f_0 - 1) = 18{,}68 \cdot 4 \cdot 10^{-3}$
$f_0 = c_0/c_S = 1{,}25 \ldots 5 = 5$ dialed; $c_S = \alpha \cdot p/760$ mmHg
$\alpha = 18{,}68 \cdot 10^{-3}$ bei $p = 760$ mmHg

the bubble growth shown in diagram (2.3.2), in comparison to equation (2.3.7), can be calculated.

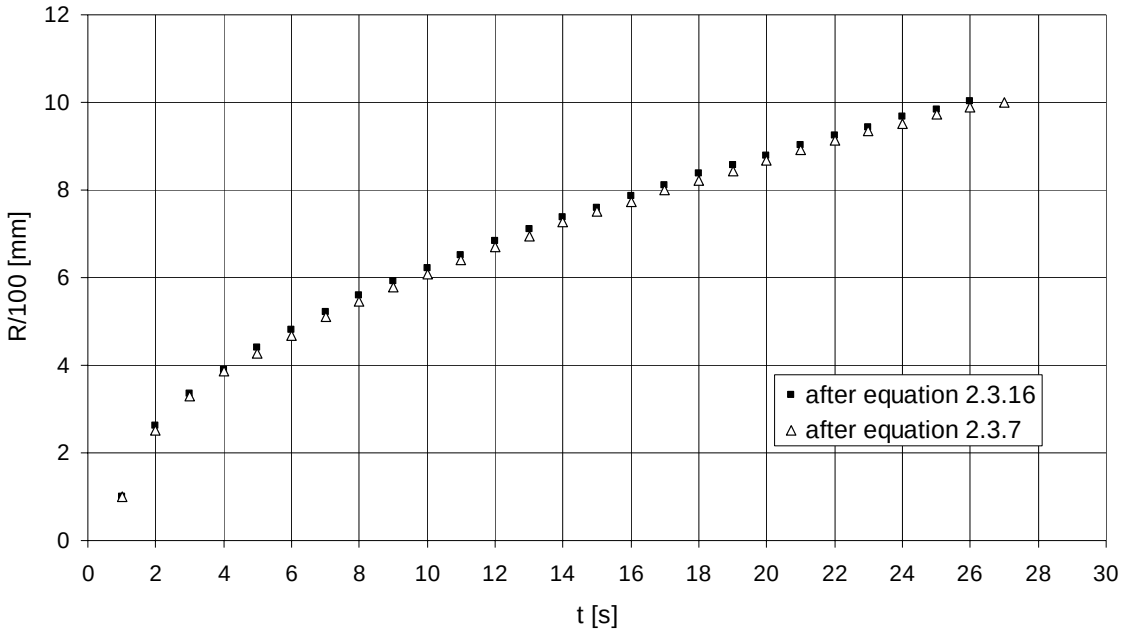

Diagram 2.3.2: Bubble growth for according to equations (2.3.7) and (2.3.16) (calculation by Heller [1995])

At $f_0 = 5$ (heavy oversaturation) the bubble has reached its tenfold radius after 26 seconds. The influence of the pressure gradient only becomes effective, when it is greater than 10^5. Since this is realized in a very short time, the process of diffusion itself is losing its influence.

2.3.4 Equation of the Total Gas Mass by Watanabe &Prosperetti

Watanabe & Prosperetti [1994] presented the following approach to determine the gas mass that a bubble will gain at sudden severe pressure reduction due to diffusion. Growth and collapse (i.e. cavitation, see chpt. 1.2 or chpt. 5.3) of the nucleus against the surrounding pressure p(t) is described by the well-known Rayleigh-Plesset-Equation:

$$R \cdot \frac{d^2R}{dt^2} + \frac{3}{2}\left(\frac{dR}{dt}\right)^2 = \frac{1}{\rho}\left[p_G + p_V - \frac{2S}{R} - \frac{4\mu}{R}\frac{dR}{dt} - p(t)\right] \tag{2.3.17}$$

The steam pressure p_v is assumed constant, p_G is the gas pressure of the bubble. The equilibrium condition of the bubble at unperturbed surrounding pressure p_∞ is:

$$p_{G0} + p_V = \frac{2S}{R_0} + p_\infty \tag{2.3.18}$$

The concentration c_S of undissolved gas at a partial pressure p_G of the gas after Henry's law is:

$$c_S = k \cdot p_G \tag{2.3.19}$$

In order to stabilize the nucleus along a streamline, inside the bubble an additional "artificial" gas is assumed, which is insoluble in fluids and whose only purpose it is to balance the pressure of the „real" gas inside the bubble, so that $c_S = c_\infty$ can be assumed in far distance from the bubble. Thus, the initial pressure p_0 of the artificial gas is given by:

$$\frac{c_\infty}{k} + p_0 + p_V = \frac{2S}{R_0} + p_\infty \tag{2.3.20}$$

In order to make sure that the artificial gas has only little influence on the subsequent development of the bubble, p is expressed by the adiabatic pressure-volume-relation:

$$p = p_0 \left(\frac{R_0}{R} \right)^{3\kappa} \tag{2.3.21}$$

with a relatively high adiabatic index κ. Tests with other values confirm that the effect on the real mass of the "real" gas inside the bubble is less than expected.
Since the bubble begins to grow, the gas pressure is falling inside, resulting in the dissolved gas diffusing from the solution into the bubble, at the rate:

$$\frac{dm}{dt} = 4\pi R^2 \frac{M_{Fl}}{M_G} \cdot \rho \cdot D \cdot \left. \frac{\partial c}{\partial r} \right|_{r=R}, \tag{2.3.22}$$

M_{Fl}, M_G are the molecular masses of the fluid and the gas.
For calculating the concentration gradient, the solution of the diffusion equation is necessary:

$$\frac{\partial c}{\partial t} + \frac{R^2}{r^2} \frac{dR}{dt} \frac{\partial c}{\partial r} = \frac{D}{r^2} \frac{\partial}{\partial r} \left(r^2 \frac{\partial c}{\partial r} \right) \tag{2.3.23}$$

with R and dR/dt from (2.3.17).
The equation has to be integrated under the conditions that $c = c_\infty$ in far distance from the bubble and that $c = c_s = p_g/k$ at the bubble's surface. The gas pressure p_g is found with the assumption that the gas behaves isothermically.:

$$\frac{p_G}{p_{G0}} = \frac{m}{m_0} \left(\frac{R_0}{R} \right)^3 \tag{2.3.24}$$

During process of the fast bubble growth, most of the gas diffuses into the bubble while the diffusion interface is very thin. This is why the approach of Eller & Flynn [1965] is employed. Here, just as in Barlow & Langlois [1962], a transformation into a Lagrange variable is done and the equations (2.3.23) and (2.3.22) are solved. The results of the calculation show that the effect of mass increase due to diffusion is substantial. Nuclei with radii of about 6µm increase their air volume up to 4.6-fold, and nuclei of 50µm in size even grow up to 13.4-fold.

2.4 Temporal Process of Gas Deposition

2.4.1 Introductory Remarks

Basic research concerning the question of gas deposition from oversaturated solutions is rare. Subsequently, the only method known to the author to measure the temporal process of gas deposition G_A of dissolved gases will be introduced. It was theoretically expanded by Kuz [1971] later.

2.4.2 Determination of the Deposition Velocity by Schweitzer

As an expression for the temporal process of gas deposition G_A of the dissolved gases, the change of gas volume dissolved in a fluid per time unit shall be chosen:

$$G_A = \frac{dc}{dt} \tag{2.4.1}$$

In order to gain the function c(t), Schweitzer [1950] conducted the following experiments with the gadget shown in figure 2.4.1.

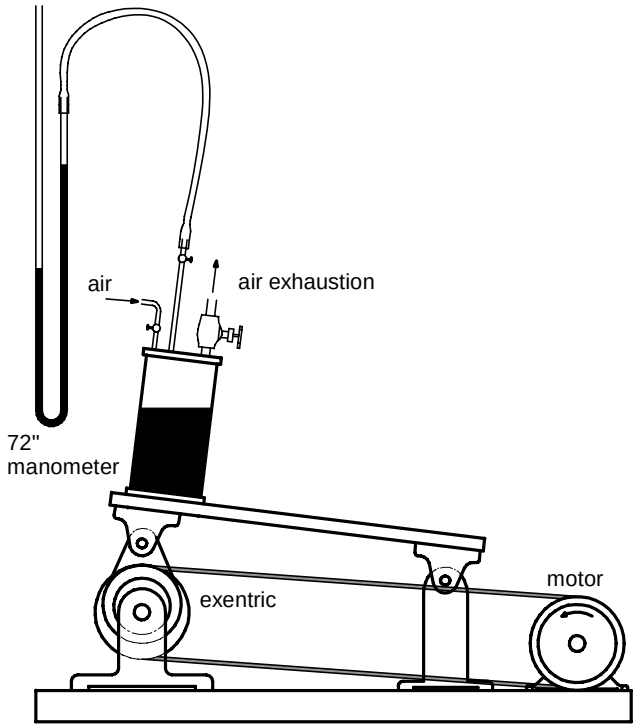

Figure 2.4.1 Gadget by Schweitzer [1950]

The closed cylindric container with a volume of 3400 cm^3 was partly filled with the fluid to be examined (distilled water, oils, fuels), so the gas phase (air) was above the fluid level. By lowering the air pressure, an oversaturated solution was produced $p_g < p_s$. When the pressure was gradually lowered, no gas bubbles developed. Afterwards, when the container was agitated at a

frequency of about 7 Hz, an intense development of gas bubbles began, causing the gas concentration c_s within the fluid reach a saturation value after a sufficiently long time. Since the container was kept closed throughout the experiment, the gas pressure p_g increased respectively.
In this simple gas-fluid system, where the sum of the dissolved and undissolved gases remained constant during the experiment, the gas deposition can be concluded by means of a linear equation of the measured pressure characteristics $p_g(t)$ in the gas phase.

The results of the experiment indicate that the development of gas G_A is decreasing, eventually approaching zero, while the gas concentration within the fluid is approaching its saturation value c_s. Therefore, direct proportionality can be assumed between the gas development G_A and the oversaturation (c_s – c). Schweitzer [1950] summarized these considerations in the following mathematical term:

$$G_A = \frac{dc}{dt} = k_A \cdot [c_S - c(t)] \tag{2.4.2}$$

Integration of this equation leads to

$$c(t) = (c_0 - c_S) \cdot e^{-k_A t} + c_S \tag{2.4.3}$$

$$G_A = k_A (c_S - c_0) \cdot e^{-k_A t} \tag{2.4.4}$$

With the saturation degree $f_0 = c_0/c_s$ as the signifying value, (2.4.3) and (2.4.4) can be re-written to:

$$c(t) = c_S (f_0 - 1) \cdot e^{-k_A t} + c_S \tag{2.4.5}$$

$$G_A = \frac{dc}{dt} = k_A c_S (1 - f_0) \cdot e^{-k_A t} \tag{2.4.6}$$

Equation (2.4.6) indicates that a high saturation degree f_0 at the beginning of the experiment significantly enhances gas precipitation G_A, with $t \rightarrow \infty$, i.e. $c \rightarrow c_s$, G_A decreasing asymptotically approaching zero. The constant k_A is a system conditional; in the experiment it results from the type of mixing of the two phases gas and fluid (Kuz [1971]).

2.4.3 Theoretical Expansion by Kuz

Kuz [1971] expands Schweitzer's [1950] findings with the following thoughts:
The saturation value cs was introduced into the calculation as a constant although the initially lowered pressure p_g had increased in the closed container due to gas deposition until a new equilibrium was reached and although the saturation concentration c_s of a solution is determined by the pressure $p_g(t)$ in the gas phase after Henry's law. The processes during gas deposition in a closed cylinder are described by the following approach:

$$G_A = k_A \left[c_S \cdot p_G - c(t) \right] \tag{2.4.7}$$

Consequently, the equations are only applicable where the gas pressure p_g remains constant above the fluid level. Schweitzer [1950] assumes further that the temporal process of gas deposition is determined by the gas excess $\Delta c(t) = c_s - c(t)$. Considering the actual circumstances, it is necessary to write after (2.4.7):

$$\Delta c(t) = c_S(t) - c(t) \tag{2.4.8}$$

However, this formulation seems also insufficient, describing the process of gas deposition inexactly and ambivalently. Specifying the difference between the varying gas contents $\Delta c(t)$ alone – without relation to the gas saturation value cs determined by the particular environmental conditions pressure and temperature – can mean both a light over- or undersaturation at low temperatures (c_s high) as well as a strong over- or undersaturation at high temperatures (c_s small). More precise, however, is the specification of the degree of the relative oversaturation.

$$f'(t) = \frac{c_S(t) - c(t)}{c_S(t)} \tag{2.4.9}$$

or the saturation degree:

$$f(t) = \frac{c(t)}{c_S(t)} \tag{2.4.10}$$

which will be used subsequently. The velocity of gas exchange G_A is determined by this saturation degree f(t) in fluids; f(t) is changing with the regarded system. For the closed container examined by Schweitzer [1950], the equation is finally modified to:

$$G_A = \frac{dc}{dt} = \eta \left(1 - \frac{c(t)}{c_S(t)} \right) \tag{2.4.11}$$

If the gas space above the fluid is infinite or the gas pressure p_g within is kept constant, the deposition velocity is:

$$G_A = \frac{dc}{dt} = \eta' \left(1 - \frac{c(t)}{c_S} \right) \tag{2.4.12}$$

The theoretical considerations about the precipitation of gases from oversaturated solutions are compared to Schweitzer's [1950] results in figure 2.4.2.

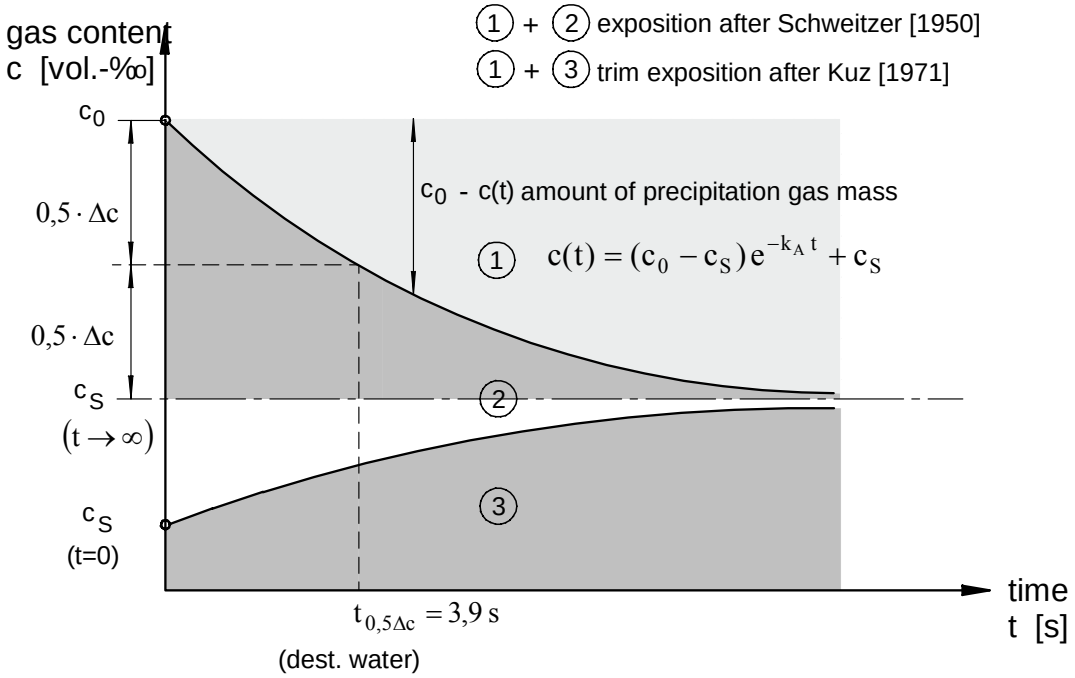

a. gas precipitation from an oversaturated solution in motion in a closed container; $c_s(t) \neq \text{const}$

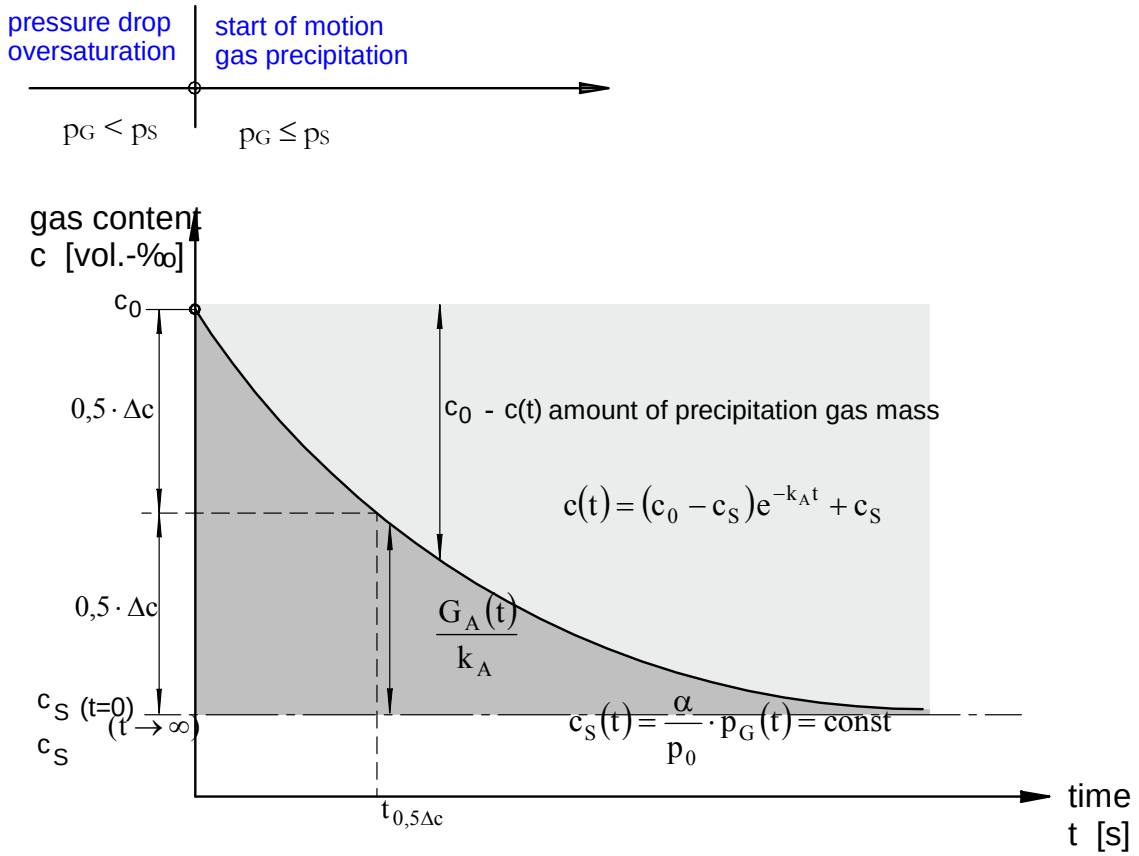

b. gas precipitation from an oversaturated solution in motion in a closed container; $c_s(t) = \text{const}$

Figure 2.4.2 Process of gas precipitation from an oversaturated solution after Kuz [1971]

3 Measurement Methods to Determine the Nucleus and Gas Content

3.1 Methods to Determine the Gas Content

3.1.1 Introductory Remarks

For determining the gas content, chemical, physical or chemo-physical methods are employed. While chemical methods are based on the bonds between the several gas components with reagents, physical methods mostly remove the diluted gases from the fluid by applying a negative pressure. According to Henry's law, the soluble gas mass is proportional to the partial pressure of the component above the solution and is – within the valid range – only dependent on the temperature. Concerning air, this range extends to about 30 bar. Solubility is decreasing with rising temperature.

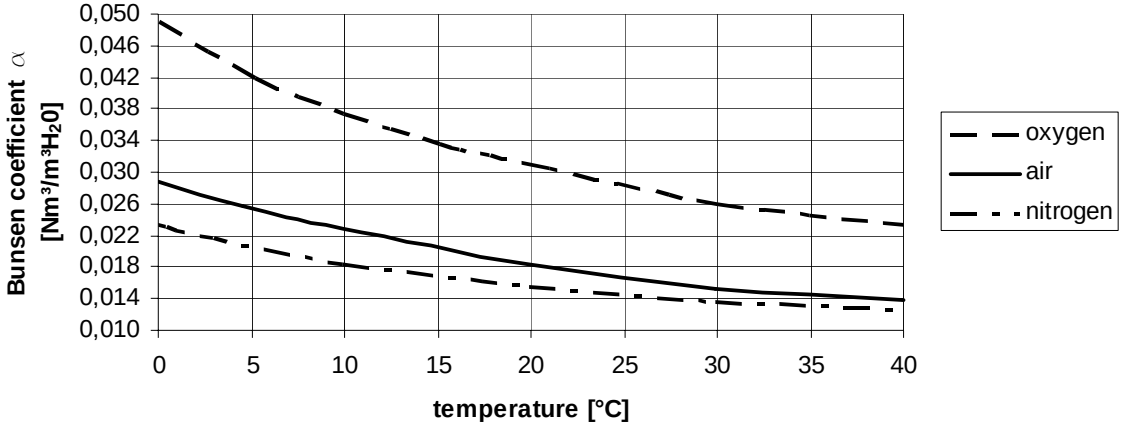

Figure 3.1.1 Solubility coefficients of oxygen, air and nitrogen in water

3.1.2 Chemical – Analytical Method

For the determination of the dissolved oxygen content in water at a concentration of c > 0.1mg O_2 / dm³ H_2O, the water-analytic Method by Winkler [1889] can be utilized. Potassium-iodide containing sodium hydroxide solution is added to a certain amount of water with $MnCl_2$-solution (manganese chloride). A precipitate is formed consisting of high-order manganese oxide hydrates, which are equivalent to the oxygen dissolved in the sample. After the precipitate has settled, it is dissolved with an acid. Iodine is released, which is equivalent to the O_2 of the original sample. The released iodine is titrated back with $Na_2S_2O_3$ (sodium thio-sulphate) and a starch solution as indicator. The used amount of thio-sulphate is a measure of the amount of O_2. The result is the specific amount of O_2 in ppm ≡ mgO_2 / kgH_2O, which is then directly comparable to the electro-chemical method, subsequently described in chapter 5.3.

3.1.3 Electro-Chemical Method

The dissolved oxygen content of the water in the cycle is used as measurand. Measurement principle: The oxygen diffuses through an O_2-permeable Teflon membrane of an electronic probe and causes an ionic current between two electrodes inside the sensor. This current is proportional to the partial pressure of the oxygen. In a receiver the probe's signal is converted and directly displayed respective to the mass proportion of the oxygen as ppm ≡ mgO_2 / kgH_2O. In order to determine the total content of dissolved gases via this display, the percentage of oxygen must be known. The atmospheric volume proportion of oxygen is:

$$\frac{V_{O_2}}{V_{Luft}} = 0{,}209 \tag{3.1.1}$$

Contrastively, the proportion of oxygen of air dissolved in water is substantially higher (see chapter 2.2), which results from the oxygen's higher solubility ($\lambda_{O_2} = 0{,}03$) compared to nitrogen's ($\lambda_{N_2} = 0{,}015$). The technical solubility coefficient λ specifies the gas mass in Ncm^3 (N characterizes the standard state T = 273,15K, p = 1,013bar) that will be absorbed by 1g of water if the partial pressure of the gas is 1,013bar.
The technical solubility coefficient is correlated with the Bunsen coefficient α by the relation:

$$\alpha = \lambda \cdot \rho_W \cdot \frac{0{,}9807}{1{,}0130} \tag{3.1.2}$$

λ and α are therefore used parallelly because the O_2-analyzer indicates the oxygen content in relation to the mass; the gas content c, however, is related to the volume. For the temperature T = 293K and p_B = 1,013bar, with $\rho_{O_2} = 1{,}43 kg/Nm^3$ the correlation between the dissolved air and the O_2 analyzer's display can be derived to:

$$c \text{ in} \frac{Nm^3 Luft}{m^3 H_2O} = 2 \cdot 10^{-3} \cdot \text{Anzeige in} \frac{mgO_2}{kgH_2O} \tag{3.1.3}$$

A fluid-gas solution is characterized by the total volume of all dissolved gases. These do not inevitably correspond to the individual components and their respective partial pressures and solubility coefficients. Thus, the term 'gas content' is used instead of 'air content' (Kümmel [1978]).

3.1.4 Gadgets to Determine the Total Gas Content

As already mentioned in chapter 2.3, by lowering the gas pressure can cause oversaturation of the solution. To regain the degree of saturation, dissolved gas will diffuse from the solution into gas phase (see chapter 2.5).
In order to achieve this and to determine the amount of gas simultaneously, various gadgets have been developed over the last 75 years whose mode of operation will be described subsequently.

3.1.4.1 Gadget by Van Slyke

Donald D. van Slyke of the Hospital of the Rockefeller Institute for Medical Research first used this method in 1917 for the mano-metric determination of blood gas by means of the gadget depicted in figure 3.1.2. The principle is to expose a fluid sample (here blood), which is connected to a mercury column, to a pressure that takes the fluid near its boiling point at the surrounding temperature. In order to accelerate the resulting degassing, the fluid is agitated – as shown in figure 3.1.3.

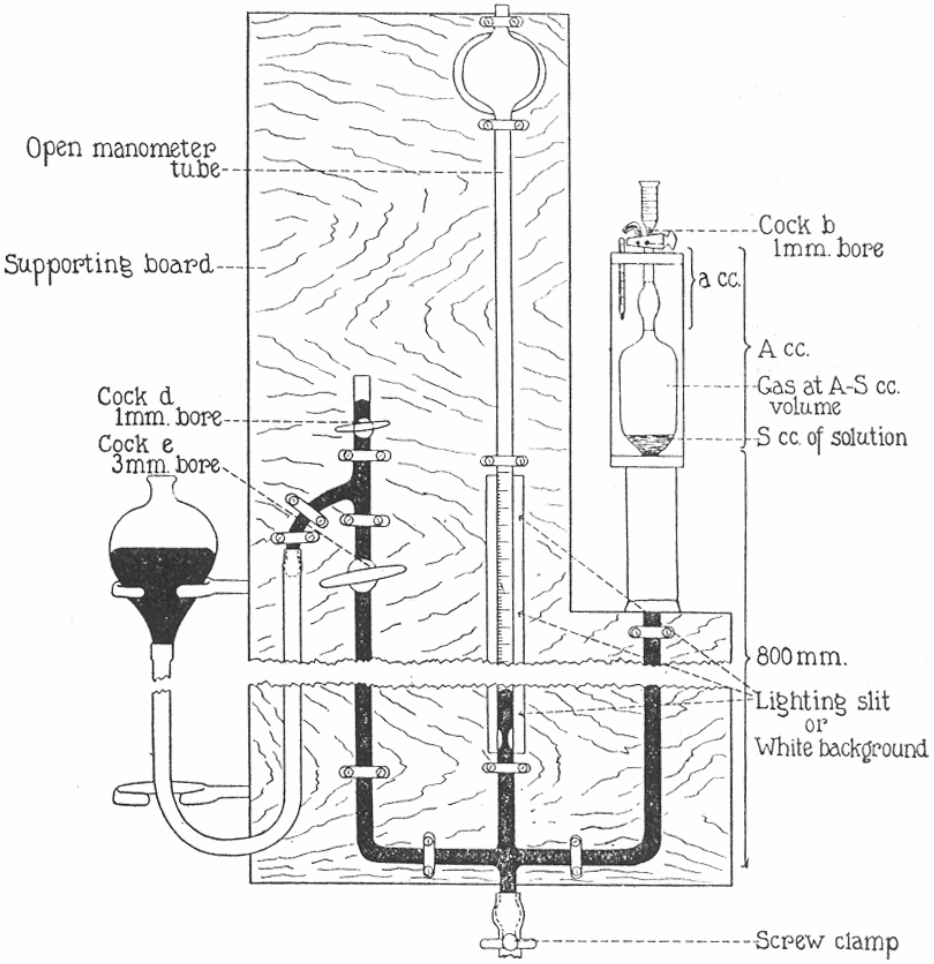

Figure 3.1.2 Gadget by Van Slyke [1924]

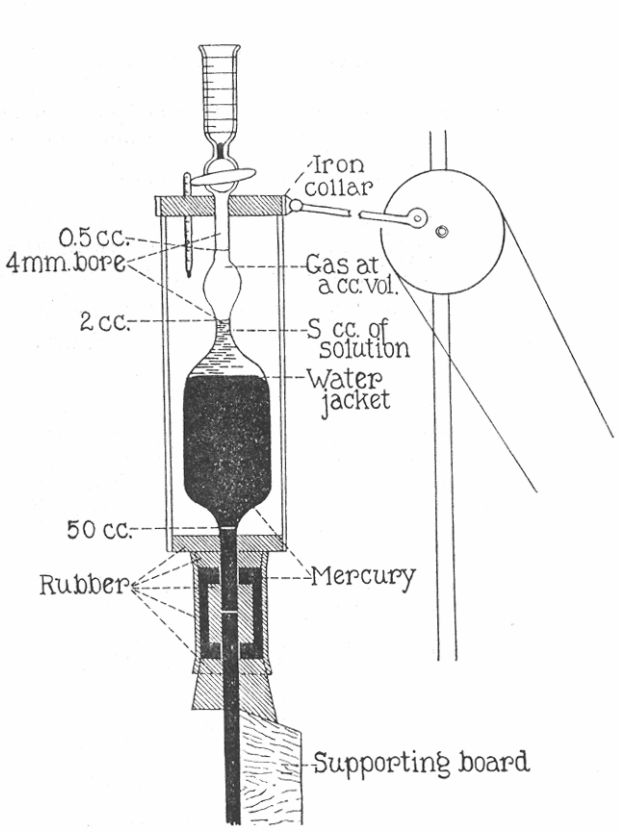

Figure 3.1.3 Detail (agitation device) of figure 3.1.2

The released gas volume was determined by van Slyke [1924] by the pressure difference in relation to the geometric dimensions of his gadget referring to a temperature of 0°C and a pressure of 760 mmHg:

$$V_{0°,760} = V(t)\,\frac{p_B - p_V}{760(1 + 0{,}00367 \cdot t)}\left(1 + \frac{V_S}{V_A - V_S} \cdot \alpha'\right) \tag{3.1.4}$$

where p_B is the corrected barometric pressure; p_D is the vapor pressure of water and t the temperature in °C. α' is the Ostwald distribution coefficient of gas between the gas and fluid phase.

$$\alpha' = \frac{T}{273\ K} \cdot \alpha \tag{3.1.5}$$

α is the Bunsen absorption coefficient; V_A, V_S are the geometric dimensions (measuring volume) and $V(t)$ is the gas volume at t°C.

3.1.4.2 Gadget by Numachi

In 1936, F. Numachi of the Hydro-Mechanic Laboratory of the Tohoku Imperial University of Sendai (Japan) picked up van Slyke's [1924] method and built the gadget depicted in figure 3.1.4 to determine dissolved gases in water.

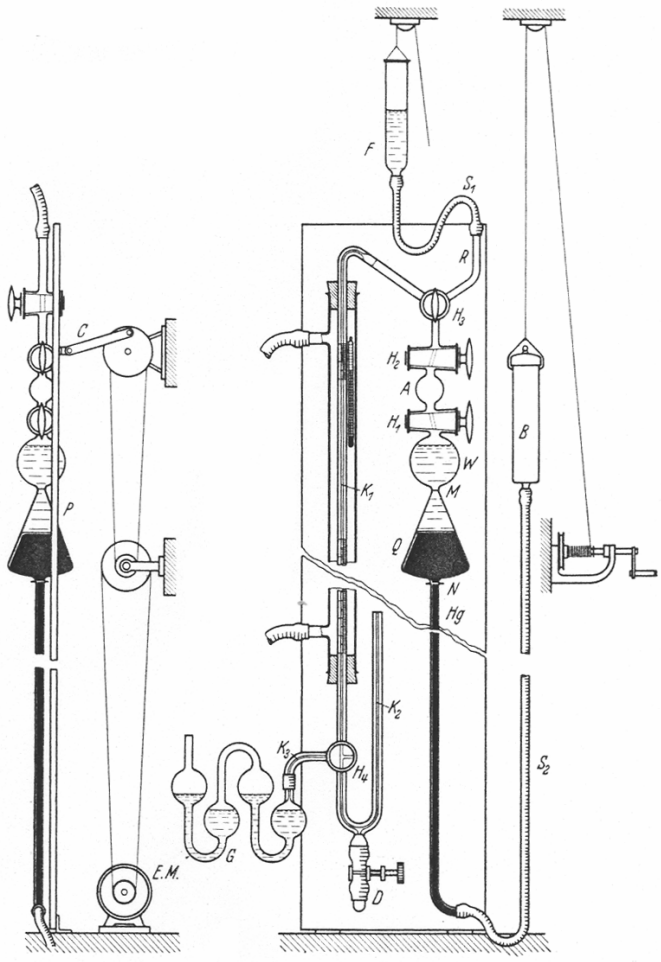

Figure 3.1.4 Gadget to determine dissolved air in water by Numachi [1936]

Numachi believed that this method does not exhibit the difficulties and complications of van Slyke's [1924] method, which were namely the difficult handling of the gadget and the production and storage of the gas-free reagents. After several alterations the new gadget featured the following advantages:

1. Water is boiled at room temperature to release the gas. Consequently, the defect in the former boiling method resulting from the condensation process of water can be avoided.
2. An asymptotic decline of the partial pressure is effected, so that even smallest residua of gas are released.
3. When the sample is taken, not even the smallest amount of gas can remain at the inside wall of the gadget, and during the process the released gas cannot be re-absorbed by the water either.
4. The composition of the gas initially dissolved in the water can be determined.

Figure 5.4.2.2 shows the relation of α_{G_n}/α_G and n. Here α_{G_n} is the volume of gas released per 1cm³ after n repetitions of the process, and α_G is the total volume of gas contained in 1cm³.

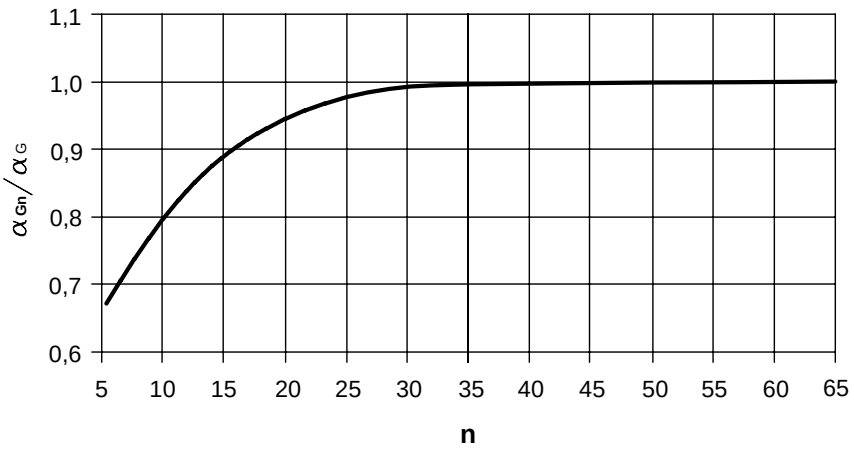

Figure 3.1.5 Percentage of air released from water against the number of repetitions of the process

The volume α_{G_N} of the gas contained in 1cm³ of water reduced to standard state can be gained as follows from the gas volume obtained from 1cm³ of water α_G:

$$\alpha_{G_N} = \frac{p_B - p_V}{760} \cdot \frac{\alpha_G}{100} \cdot \frac{273 \cdot 2}{T} \tag{3.1.6}$$

To reduce the time necessary for determining of the gas content, the sample is agitated at a suitable frequency (about 120min-1) and amplitude of 10 cm. Thus, the required time to release the gas completely is reduced to about one hour.

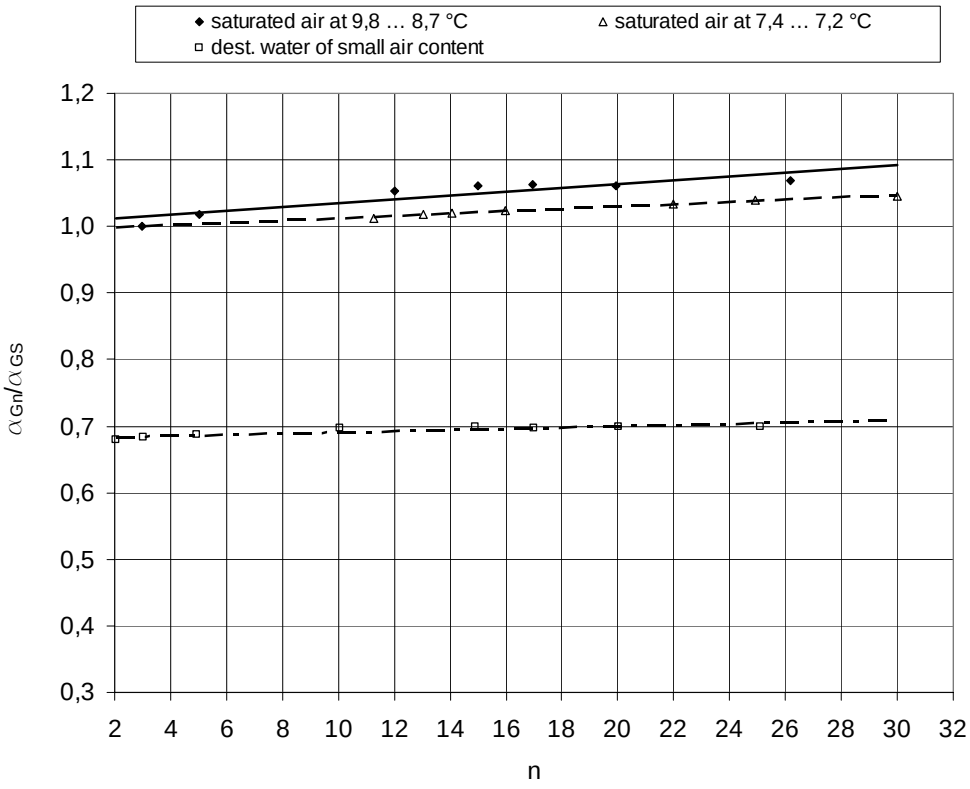

Figure3.1.6 Results gained with the vibration method

Nr	date of sampling	types of water	Temp.°C	α_{GN} x 100	α_{GN}/α_{GS}	α_{CO}/α_{GS}	Vol.-%		
							CO_2	O_2	N_2
1	19.12.1934	service water at the university (directly from the tap)	9,5	2,48	1,06	1,02	4,0	29,7	66,3
2	28.02.1935	service water of the city of Sendai (as above))	14,0	2,63	1,24	1,21	1,6	31,4	67,0
3	20.05.1935	water from the tank of our hydraulic laboratory (as above	11,8	2,43	1,09	1,02	7,0	30,09	62,1
4	13.12.1935	water from the tank of our hydraulic laboratory (as above))	9,0	2,49	1,05	0,97	7,5	30,09	61,6
5	10.01.1935	distilled water (one month after withdrawal))	9,8	1,58	0,68	0,68	0,0	32,0	68,0
6	26.05.1935	sea water (at the surface)	16,3	1,95	1,13	0,97	14,4	25,5	60,1
7	26.05.1935	sea water (at a depth of 1.6 m)	16,0	1,91	1,10	0,96	13,1	28,0	58,9
8	26.05.1935	sea water (at a depth of 6.0 m)	11,0	2,06	1,10	0,96	12,0	27,9	60,1
9		air-saturated water at a teperature of 15°C (reduced to 0°C, 760 mm)	15,0	2,09	1,00	0,99	1,4	33,3	65,3

α_{GN}: total volume of air, reduced to standard state (0°C, 760 mm), that had initially been contained in 1cm³ of water

α_{CO}: same as α, but exclusively CO_2

α_{GS}: volume of air, reduced to standard state (0°C, 760 mm), dissolved in 1cm³ of air-saturated water of the sample water's temperature when the sample was taken (by Landolt-Börnstein).

Figure 3.1.7 Composition of dissolved gas after Numachi [1936]

3.1.4.3 Gadget by Schöneberger

In 1966 at the TH Darmstadt, in order to determine the gas content of water, Schöneberger used the gadget, which was later utilised again by Gast [1971]. It is depicted in figure 3.4.3.1 and represents a modified van Slyke or Numachi gadget. For the determination of the released gas volume, scales were attached to both the capillary and the pressure vessel.

When the device was filled, the mercury column and the pointer of the pressure vessel had to be at their respective zero marks. If then at open outward valve the pressure vessel was gradually lowered, the correlation between the indices of the mercury column and the position of the test vessel was obtained and could be plotted as calibration curve. This correlation is important since the pressure inside the test vessel must later equal the atmospheric pressure while the released gas volume was determined. The following procedure was pursued in order to determine the gas content:

1. The test vessel is filled with the water to be examined (both indices at their zero marks)
2. Then both valves of the test vessel are closed.
3. The pressure vessel is completely lowered. The dissolved gas is released from the water. The process can be accelerated by having a few brass chips inside the test vessel and agitating the whole gadget with an electric engine. Discharging is completed when the partial pressure of the gas equals the saturation pressure of the water. The final position of the mercury column is a measure of the gas volume at the partial pressure p_G.
4. The pressure vessel is raised until the index of the mercury column equals the previously recorded calibration curve. This position at L_1 is a measure of the gas volume at atmospheric pressure.
5. Now the released gas can be pushed out by raising the test vessel to its zero mark, and this procedure can be repeated until no gas release is noticeable any more.

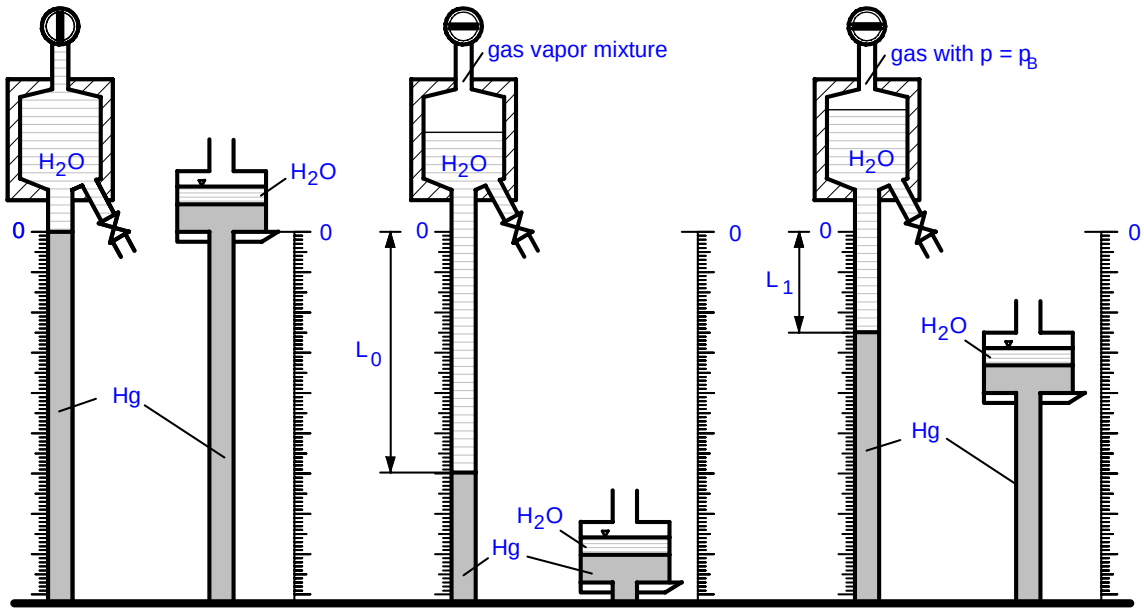

1. before measuring: Test vessel is completely filled with test water.	2. gas discharging finished: Gas-steam mixture in the test vessel. State of saturation in the water.	3. Measurement of the released gas volume at atmospheric pressure.

Figure 3.1.8 Gadget by Schöneberger [1966]

The total gas content sums up to:

$$\alpha_G = \sum L_i \cdot \frac{A_R}{V_W} \tag{3.1.7}$$

3.1.4.4 Gadget by Brand

On 14th December 1973, Brand applied for a patent at the German Patent Office, under reference number 2362158, with his "Apparatus for the determination of the amount of dissolved gas contained in fluids".

This gadget, depicted in figure 3.1.9 (Brand [1980]), consists of a larger cylindrical space with a standpipe connected to it. Inside this larger space there is a rubber bubble, which is attached to a tube leading outwards. The standpipe is closed with a plug. The rubber bubble is inflated just until it is not yet stretched. Then water is poured in via the standpipe until a mark. If now a vacuum pump is connected to the tube leading outwards, the rubber bubble will contract completely producing a negative pressure near the steam pressure of water inside the vessel. The dissolved gas is released and can be expelled, accelerated by agitating the vessel.

After turning off the vacuum pump, atmospheric pressure will re-establish above the re-inflating rubber bubble. When the gadget is put upright, the released gas gathers in the upper part of the standpipe. There the amount of released gas can be determined by means of a scale. To calculate of the amount of gas, it is necessary to determine the used amount of water accurately before or after pouring it in. This can be done in a measuring cup or by weighing the vessel before and after filling.

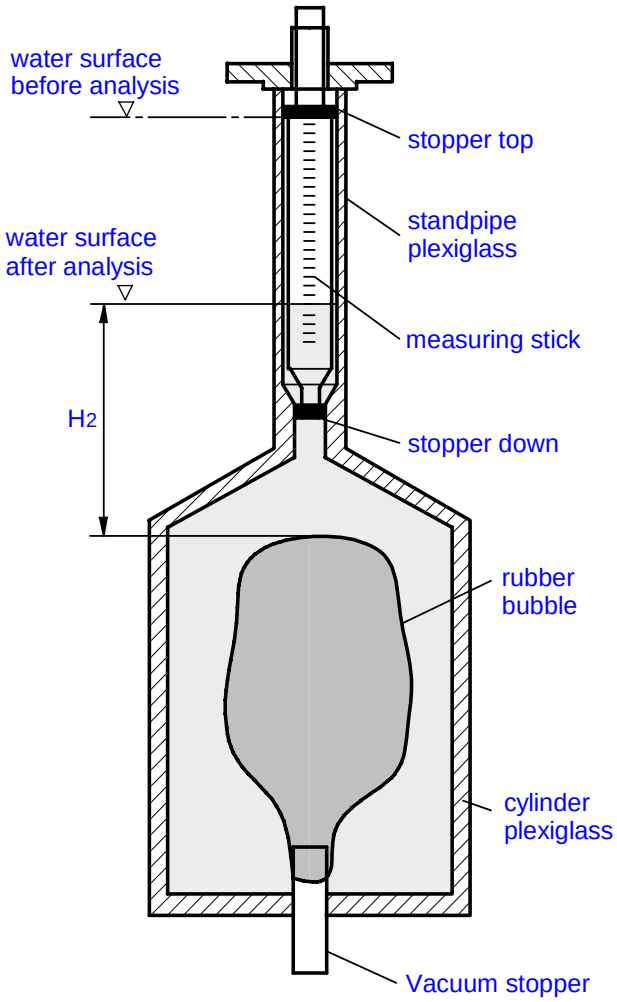

Figure 3.1.9 Gadget by Brand [1973]

Calculation is then done as follows. When the vacuum valve is open, the pressure $p = p_B - \rho_W \cdot g \cdot H_2$ is effective on the gas volume V_G in the standpipe. The gas volume reduced to barometric pressure $V_{G,Bar}$ results to:

$$V_{G,Bar} = V_G \cdot \frac{p_B - \rho_W \cdot g \cdot H_2}{p_B}$$

Thus, the gas content is:

$$\alpha_G = \frac{V_G}{V_W} \cdot \left(1 - \frac{\rho_W \cdot g \cdot H_2}{p_B}\right) \tag{3.1.8}$$

3.1.4.5 Gadget by Heller

In 1991, the author presented a gadget for measuring the total gas content (depicted in figure 3.1.10) within the scope of a thesis paper at the TU Dresden. The functioning of this gadget is based on the principle of displacement, realized by a PTFE bellows, subsequently referred to as "piston". The maximum test volume is 600cm³. At a full piston stroke of 75 mm, a volume of 270 cm³ is displaced or vacated respectively. This displacement ratio is sufficient to produce the necessary negative pressure (max. steam pressure). An index moving along with the piston shows the piston's position in a dial gage (not shown in the picture).

.When measuring, the inward and outward valves must be closed while there is atmospheric pressure inside the measuring instrument. By means of a switchable electric engine (not depicted) driving a threaded rod, the piston is contracted and degassing is initiated.

In order to be able to measure the released gas volume, the piston is withdrawn towards its upper dead center exactly until the connected pressure transducer shows atmospheric pressure. The gas volume accumulated inside the instrument is the total gas content of the water sample (first phase). The initially existent water vapor will condense until reaching atmospheric pressure. The piston has not reached its starting position from before the evacuation process any more because of the now existing gas volume. The piston's position L_M is shown by the dial gage.

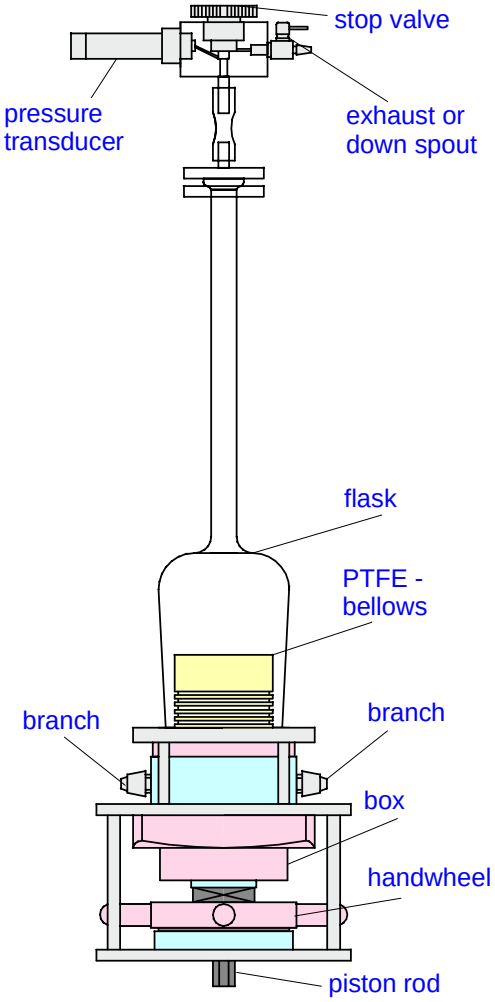

Figure 3.1.10 Gadget by Heller [1991]

If the same water sample is to be evacuated again, the piston will be moved upwards while the outward valve is open, until the water column has reached the valve's position. After closing the valve, another evacuation process can be started. Calculation of the total gas content is done with the formula:

$$\alpha_G = \sum L_M \frac{\frac{\pi}{4} \cdot d_W^2 \cdot (p_B - p_V) \cdot T_0}{V_W \cdot p_0 (T_0 - t)} \cdot 1000 \qquad (3.1.9)$$

with:

$\sum L_M$ - sum of dial gage amplitudes , d_W - effective piston diameter

V_W - Volume of the water sample; p_B - atmospheric pressure

p_V - vapor pressure; t - surrounding temperature

The steam pressure can be taken from charts. With T_0 = 273,15; p_0 = 760 Torr, the measured values are transformed to standard state.

3.2 Methods fort the Determination of Nucleus Spectra

3.2.1 Introductory Remarks

Assessing the properties of water by the total gas content is problematic because only the undissolved part, so-called nuclei, is regarded as the essential influencing variable to the occurring hydro-dynamic effects. Beginning cavitation may be an example here (see chpt. 1.2 or for a detailed discription chpt. 5.3), for whose occurrence the distribution of free nucleus bubbles in size and frequency is of major importance. Some of the known measurement methods for this distribution will be described in short subsequently (see ITTC [1972]).

Measuring nucleus spectra in flowing water proved to be especially complicated and can only be realized with enormous technical effort. The speediness of the measurements and the results' accuracies are often unsatisfactory.

3.2.2 Electrical Methods

3.2.2.1 Bubble Counter – Resistance Measurement

The resistance to electrical current in a conducting fluid through an orifice is affected by the presence of a non-conducting object in the fluid as it passes through the orifice. For counting bubbles in a water tunnel, water would be drawn from the tunnel and passed through the orifice, or a probe used. The passage of bubbles through the orifice modifies the conductivity and the amount of modification is a measure of the bubble size. Solid particles passing through the counter will disturb the measurement and if large enough, may obstruct the flow. The flow through the counter is at a different pressure a d velocity than in the tunnel so the bubble may be at a different size than in the tunnel. The size of the orifice is fixed by the expected bubble size. Because of this size, the statistical sample is very small. Accuracy of counting the number of bubbles, or solid particles, is very high but accuracy of the size measurement is unknown.
(Schiebe [1969], Ahmed u. Hammitt [1969], Ahmed [1972], Keller [1974]).

3.2.2.2 Probe for Resistance Measurement to Determine Cavities in Fluids

A pole-shaped probe was developed to measure the immediate local electric resistance between two electrodes inside the probe's head in a two phase flow. The liquid phase must be electrically conductive. A bubble hitting the tip of the probe causes a change of the electric resistance. In an analysis of the phase change of the signal, the following will be observed:

- The frequency of the phase change and therefore the electric resistance at the tip of the probe is determined by the local bubble frequency.
- The time fraction of the state "circuit open" is a measure of the local void fraction.

– The length of stay of each bubble can be related to the bubble diameter.

For very few bubbles, the signal range of the probe may not be sufficient to determine the concentration. Furthermore, the size of the probe is decided by the measurable size of the bubbles whose diameter should be slightly larger than that of the probe. The one tested by Neal and Bankoff [1963] had a diameter of 500μm. This device, however, is very suitable to measure nucleus sizes and distribution in a water tunnel.

3.2.3 Acoustic Methods

3.2.3.1 Absorption of Ultrasonic Energy – Measurement of Reverberation Decay

The reverberation decay of ultrasonic energy in water is measured. Ultrasonic frequencies are used in a range to excite various bubble sizes at their resonant frequencies. The bubble volume of a given size can be determined by the general decay rate at a given sound frequency.
This method is essentially continuous but concentration of nuclei is determined from theory that includes a number of assumptions among which is a homogeneous distribution of nuclei. There are also instrumentation problems with reverberation in a water tunnel and problems if there are too many bubbles. Rectified diffusion may also play an important role in measured bubble size. The smallest bubble size Strasberg [1955] was able to measure with his apparatus (in still water) was 3 micrometers in radius. Gavrilov [1966] measures bubble sizes from 3 to 69 micrometers in radius (Strasberg [1957], Richardson [1956], Iyengar [1956], Turner [1963, 1963, 1969], Gavrilov [1970]).

Killen and Ripken [1964] measured bubble diameters from 20 to 110 micrometers and Brockett [1969] measured bubble diameters from 10 to 80 micrometers. The maximum size depends on the tunnel characteristics used and the minimum size depends on the transducer. Schiebe and Killen [1969, 1971] conclude that this method is usable in a concentration range of 0,03 to 1,0 parts per million. This concentration may be higher than the concentration levels in some experimental facilities during cavitation inception experiments. The error in size and concentration may be large.

3.2.3.2 Counting of Bubbles Caused by Sound-Waves

The number and size of nuclei are inferred in water by passing sound waves through a flask of water at various frequencies and making a statistical analysis based on visual observations. The frequency at which cavitation occurs supposedly gives the bubble size and the number of cavitation events is equal to the number of bubbles at the size. This method will work only in still water without too many bubbles. The bubble concentration has been related to the sound pressure required for their growth to visibility but has not been related to the bubble size. To relate the sound pressure to bubble size, the process of bubble growth, as well as the mechanism which stabilizes the nuclei, must be known. Accuracy is unknown (Messio [1963]).

3.2.4 Optical Methods

3.2.4.1 Photographic – Direct

This method of determining bubble size and concentration consists of photographing a volume of fluid and measuring the diameter and counting the number of bubbles from an photographic plate. The method is two dimensional in that all bubbles in the volume which are in focus are contained on the film record and the distribution across the volume cannot be obtained.
The method is simple to use and the bubble size, which can be measured, depend on the camera lens systems and the resolution of the film. If small sizes. e.g., the order of one micrometer in diameter, are geing investigated, the volume of fluid would be so small that it would be difficult to obtain a sufficient statistical average to obtain the concentration. A number of investigators have used this method (Fox [1955], Ellis, [1965]).

Comparative measurements to determine bubble and particle spectra with three different optical methods were conducted by Peterson (Holography, see chpt. 3.2.4.3), Keller (Diffused Light Method, see chpt. 3.2.4.5) and Danel (microscope) in 1975. The latter used a specially designed microscope lens in order to photograph the content of suspended matter directly. While holography and the diffused light method were comparable very well, measurements with the microscope produced values significantly too high.

3.2.4.2 Photographic – Indirect

In this method a definite quantity of water is entrapped in an apparatus some distance from the test section. The volume is isolated from the mechanical effects of the flow and held for a certain period of time under the same temperature and pressure that it had in the flow. During this time interval, the bubbles contained in the volume float upward and settle against a glass top on the apparatus. The deposited bubbles are photographed, then the size and concentration determined from the film. Absorption of the nuclei, among many other problems, would be an important drawback to this method (Ilichev [1966]).

3.2.4.3 Holographic Reproduction

Holography was developed by the Hungarian physicist Dennis Gabor (1900 – 1979) in 1947. However, only in 1960 it gained practical importance with the invention of the Laser, a light source with greater coherence length than previous light sources. In comparison to a hologram, in every point of a photograph only one bit of information is recorded, that is the intensity (i.e. the squared amplitude of the electric field) of the light wave illuminating that certain point. In a color photograph, slightly more information is stored. (In fact, the picture is taken three times through three different color filters.) This allows a limited reconstruction of the wave length and thus, the color of the light. However, the light reflected from or diffused by a real object is not only characterized by its amplitude and wave length but also by its phase. In a photograph, the phase of the light reflected from the real object is lost. In contrast, in a hologram both amplitude and phase of the light are recorded (normally at a certain wave length).

When reconstructed, the resulting field of light is (partly) identical to that reflected from the object, which makes it possible to obtain three-dimensional pictures. (Though monochromatic in most cases, color holograms are also possible.). Due to the necessity of interference between reference and object ray, Laser light with sufficient coherence length is used for holography. The laser light is split into two rays. On the one hand, the reference ray, on the other hand the object ray illuminating the object (fig 3.2.1).

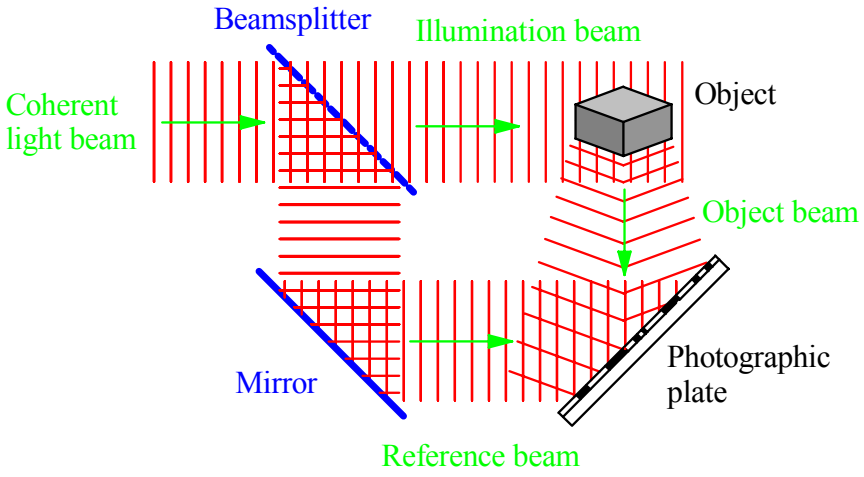

Figure 3.2.1 Process of hologram recording

In order to record the phase of the light wave at every point of the picture, for holography a reference ray is used that interferes with the light of the process or object (the object ray). Due to optical interference of the light waves, between reference ray and object ray a series of intensity patterns are produced, which can be recorded to image storage devices of high resolution (photo plates, special electro-photography such as thermoplastic plates). These patterns form a sort of diffraction grating on the film. When determining bubble sizes by holography only one state (or a series of states) is registered.

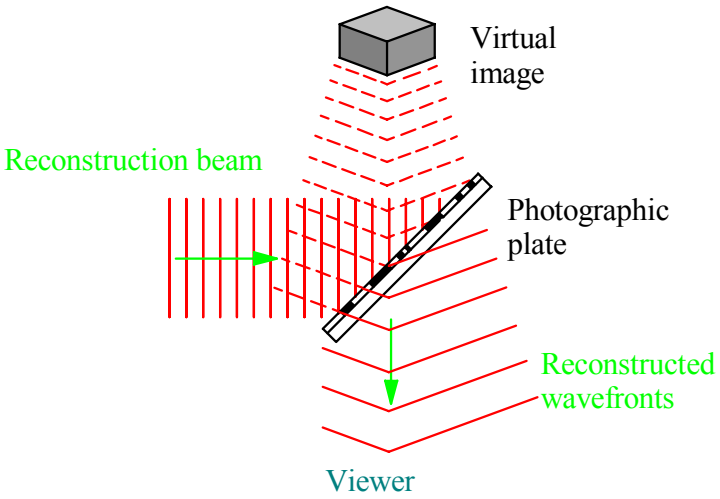

Figure 3.2.2 Process of hologram reconstruction

After the development of the film, the original object ray with both its intensity and phase is reconstructed with the reference ray being diffracted at the intensity patterns on the film. Since both intensity and phase are reproduced, the image appears three-dimensional. The observer varying his/her viewpoint can watch the image turning just as the original would do.

In many areas of physics and engineering, three-dimensional particle fields need to be analyzed according to position and size of the particles. Droplet fields such as in aerosol research, meteorology or engine development at fuel injection could serve as examples. A similar problem arises in cavitation research (see chpt. 5.3). Lauterborn [1979] developed a method to process three-dimensional holographic images digitally by means of a device for the automatic analysis of three-dimensional particle distributions in co-operation with a computer-based focusing on objects in the depth dimension. For example, when reconstructing a hologram with air bubbles in water, two different depth planes at a distance of 5 mm are analyzed.

Thanks to the development of holography, Laser technology and parallelly working computers, today also fast and longer motion processes can be recorded and their dynamics analyzed. This task is very complex and, depending on the particular case and order of velocity, it requires specialized equipment, methods and algorithms. Lauterborn [1989] provides detailed insights into holographic high velocity kinematography. He describes the principle structure of a complete installation for three-dimensional motion analysis by holographic kinematography, suitable recording Lasers and their particular characteristics, and methods for the image separation in hologram series, with which preferably long hologram series and high hologram frame rates can be obtained. For example, holograms with a resolution of 4 μm at a hologram frame rates of a few 100 Hz were produced in order to detect particle paths in a bubble chamber. Additionally, a bubble collapse due to excitation by a sound field under the influence of surface oscillation could be recorded at a frame rate of

66.7 Hz and an image size of 2.4 mm x 2 mm as well as the shock wave of a laser-induced bubble interacting with its surrounding. For further details see Lauterborn [1972, 1977], Hausmann [1978] and Hentschel [1980].

3.2.4.4 Transmitted Light Particle Counter for Fluids [TOPAS]

Apart from particle size distribution, information about particle number concentration is often necessary. Among the optical measurement methods, the detection of extinction (weakening) of individual particles as a particle characteristic is an effective principle to identify particle sizes in a wide measurement range. The physical effect that particles charged with light waves produce extinction respective to their size is utilized. For this purpose, the particle-laden medium flows continually through a defined measuring space. The concentration in the medium and the measuring volume must be adjusted such that at the moment of measurement there is a high probability of only one particle being within the measuring volume.

The signals produced by the individual particles are classified by numbers as particle size information into pre-defined classes. The major limitation of this measurement principle is given by the particle number concentration that is to be analyzed. Therefore, in the past measurement systems assessing individual particles were developed for pure media measurement instrumentation. A recent optical configuration in connection with special signal processing ensures allows the measurement of high particle concentrations.

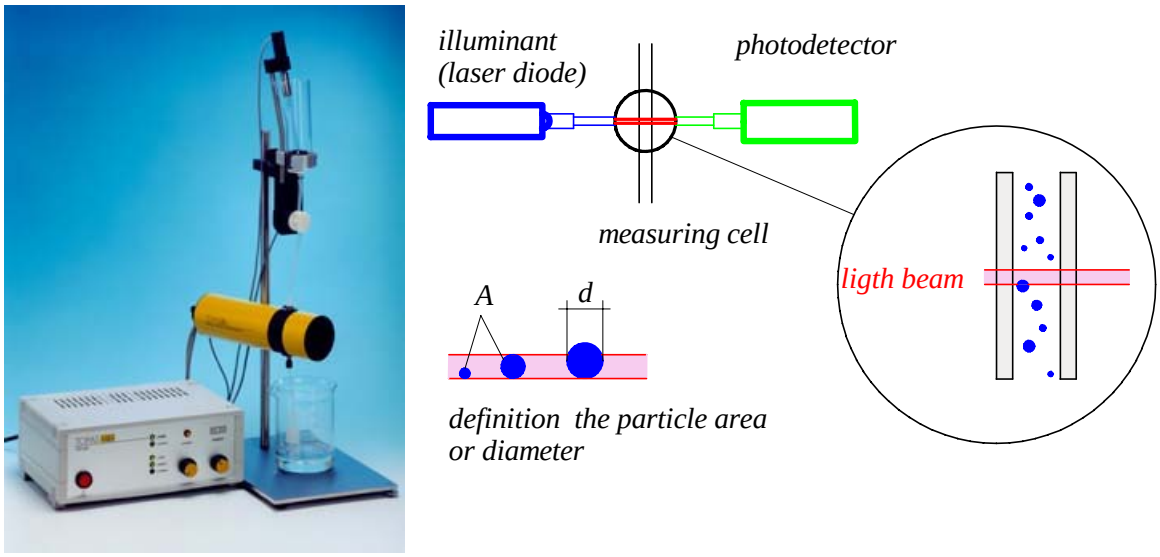

Figure 3.2.3 Particle counter for fluids and principle of extinction measurements by TOPAS [2001]

As shown in figure 3.2.3, the measuring device, which bases on optical measurement of individual particles, allows the determination of particle size distribution and concentration in fluids at a high resolution of particle sizes. Measurement methods assessing individual particles relate the physically measurable value (the particle characteristic) to a particle diameter independently and without any presumptions. Thus, these methods guarantee a high sensibility and accuracy in combination with a quick evaluation of particle systems. The measuring range of particle sizes is 1.5 to 200 µm; the measuring volume is 10 to 30 ml/min and the maximum measuring concentration is $2 \cdot 10^4$ particles/cm^3 (siehe TOPAS [2001]).

3.2.4.5 Diffused Light Counting Method

For the determination of nuclei in water tunnels, Keller [1978, 1979] developed a measuring device (figure 3.2.4) whereby nuclei can be collected and their sizes measured individually by exploiting the optical behavior of nuclei. This method founds on the results achieved in aerosol research at measuring particle sizes. One difference to aerosols is that bubble nuclei have a smaller refraction index than the water surrounding them.

The measuring procedure is described as follows: Flying through an optically limited measuring volume of strong illumination (He-Ne laser), a nucleus emits a flash of light. The measuring volume is the cross-section area of the laser beam and the optical path of the receiver, which is of such small dimensions that, at nucleus concentrations occurring in tap water, the probability of several nuclei coexisting there simultaneously is low. Via a system of photo lenses and apertures the diffused light reaches a photo multiplier whose electrical initial impulse is proportional to the diffused light intensity and thus, proportional to the nucleus size.

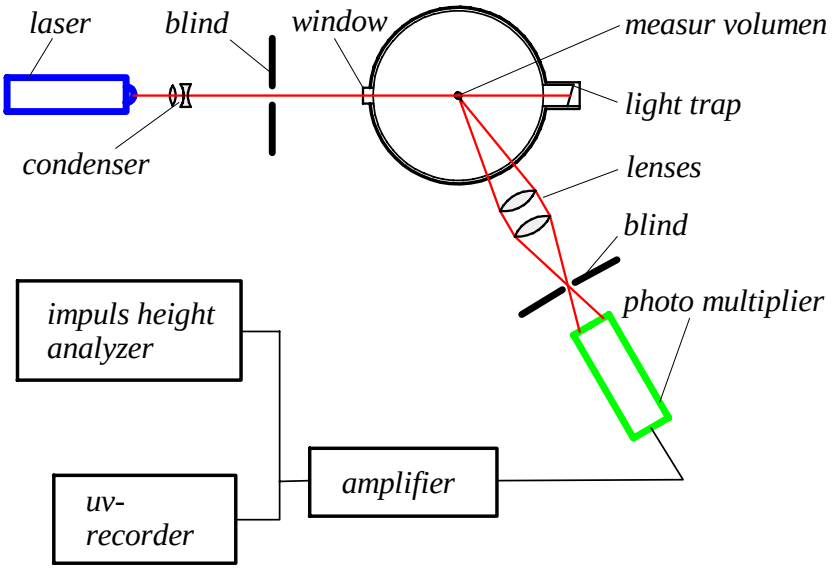

Figure 3.2.4 Principle scheme of the test arrangement for collecting nuclei after Keller [1970]

The impulses are amplified and electronically analyzed by an impulse height analyzer. After a certain time of measuring, the result is obtained in a histogram of nucleus sizes. The nucleus concentration can be calculated from the number of measured nuclei, the size of the measuring volume and the flow rate of the water through the measuring volume.

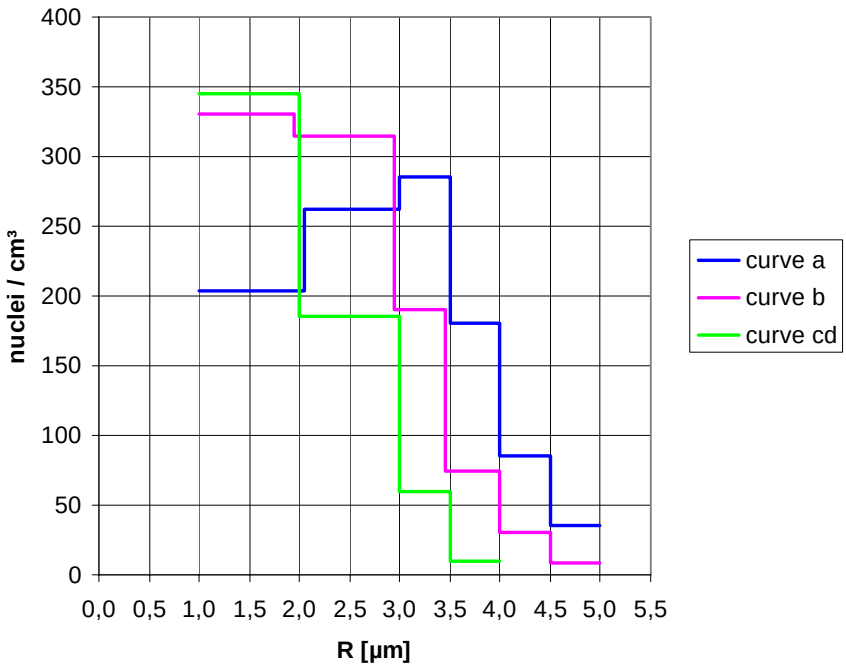

Figure 3.2.5 Nucleus spectra of filtered tap water after various resting times after Keller [1970]

Dispersion intensity decreases rapidly with the nucleus' radius. So, the lower bound of the individually detectable nucleus size is about 1µm. Figure 3.2.5 depicts the measured nucleus spectra of filtered tap water after various resting times. These graphs are typical of several similar measuring cycles and clearly show the change of nucleus spectrum after certain times. A maximum number of nuclei can be found at about 3µm and in fresh water. With an increasing

resting time, this maximum shifts to smaller nuclei. After 20 hours at the latest, the nuclei will have stabilized. The accuracy of this method can be estimated to a total error of about 20% with the exact determination of the size of the measuring volume holding the largest uncertainty. Thus, the major advantage of the diffused light counting method lies in the quick and contact-free measurement of nucleus spectra in water tunnels. For the gadget depicted in figure 3.2.4 the lower bound for the diameter of detectable single nuclei proved 1µm. The water to be examined from a circulation tunnel (cavitation tunnel) was lead through a side channel. During recording the nucleus spectrum, the flow velocity was 7 cm/s at a maximum. This velocity is limited by the electronic equipment that processes the photo multiplier impulses.

Landa [1970] reports a method to collect nuclei directly in the test section at flow velocities up to 12 m/s. With this measuring device, bubbles in the range of 125µm to 1000µm can be detected. Gas bubbles of this order occur in highly turbulent flows due to air intake through the fluid surface or simultaneous degassing processes.

3.2.4.6 Center-Body-Method

The fluid is exposed to a defined flow and pressure field with pressure and flow rate being measured at which a defined number of bubbles per time or measuring volume (due to cavitation) are produced. The limits of the flow are formed by a Venturi nozzle, which is constricted by a so-called centerbody (Gindroz [1992]). Due to subsequent implosions, the bubbles are acoustically detected and counted (impact sounds). The number of cavitation events depending on the pressure in the narrowest diameter of the nozzle is measured. The pressure is determined from a wall pressure measurement and the flow rate. By changing the flow rate through the Centerbody Venturi, the lowest pressure can be adjusted. Its value is determined from measurements of upstream pressure and the flow rate, and the inner geometry.

$$p_{min} = c_{p\,min} \cdot \frac{\rho}{2}\left(\frac{\dot{V}}{A_{ref}}\right)^2 + p_{ref} \tag{3.2.1}$$

where A_{ref} , the reference section upstream of the restricted section, and $c_{p\,min}$ the minimum pressure coefficient along the Centerbody, are known.

Then, all the nuclei with a critical pressure, p_{krit}, higher than the lowest value in the Venturi, p_{min}, will be activated. By repeating this operation for different "lowest pressure values", it is possible to determine the cumulative nuclei distribution as a nuclei spectrum function of the critical pressure, and then, function of the critical radius, R_{krit}.

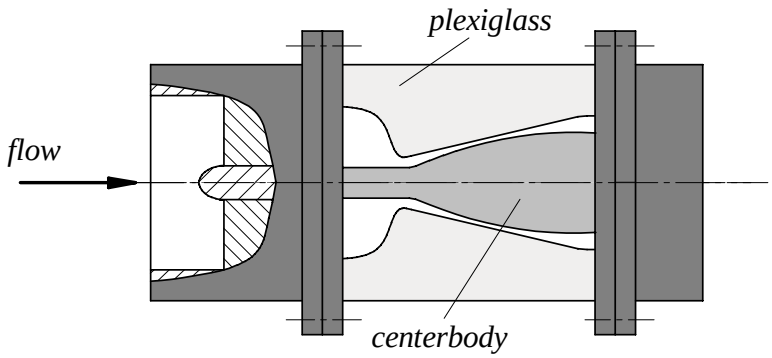

Figure 3.2.6 Principle of the Centerbody Venturi after Gindroz [1992]

The direct relation between critical pressure and critical radius being:

$$R_{krit} = -\frac{3\kappa - 1}{3\kappa} \cdot \frac{2 \cdot S}{(p_{min} - p_V)_{krit}} \tag{3.2.2}$$

κ - ratio of the specific heats of the gas (c_p / c_v)

S - gas-liquid surface tension; p_V - vapor pressure.

Each activated nucleus becomes a bubble, that collapses after growth time and generates a short shock wave. The number of activated nuclei is determined by counting these shock waves, with a piezo-ceramic transducer, associated with an appropriate system for the signal treatment.

3.2.4.7 Phase Doppler Anemometer

The Phase Doppler Anemometer is an optical and therefore contactless measuring device for the simultaneous measurement of size and speed of spherical particles and bubbles in flowing substances. Typical areas of application are the nebulization of fluids (sprays), fuel injection, sputtering, spray drying, pest management, air moistening and so on as well as two phase flows: gassing of fluids, emulsions, cavitation and the like. The measurable particle size ranges from 0.5µm to some mm, velocity ranging at about ±500m/s.

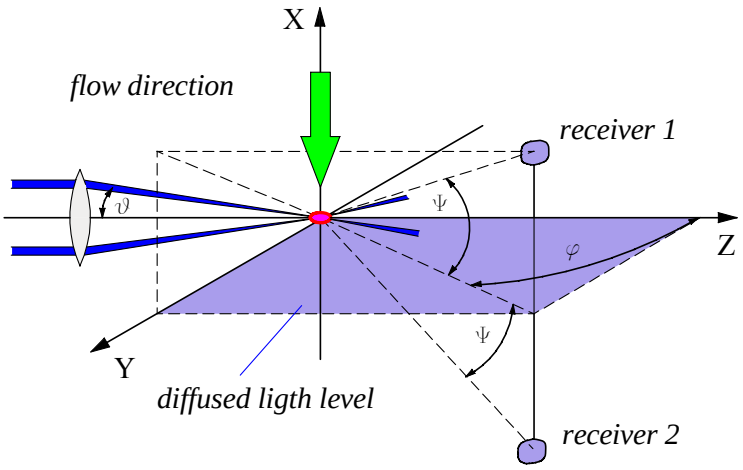

Figure 3.2.7 Phase Doppler Anemometer measurement setup

Similarly to the Laser Doppler Anemometer (LDA), the measurement principle is based on the diffusion of light at small particles. The Doppler frequency shift of the diffused light is utilized to determine velocity, whereas the phase shift between the Doppler signals of two spatially separated detectors is used to determine size.

A particle flying through the measuring volume diffuses the (laser) light of the two laser beams. The two diffused waves will superimpose and produce a signal at a frequency that is proportional to the particle's velocity. By means of two detectors, the phase-delayed signal is recorded. Phase delay is proportional to the particle's diameter, which is calculated as:

$$d_P = \frac{\lambda_0}{2\pi \cdot n_M b_i} \cdot \phi_i \qquad (3.2.3)$$

with:

λ_0 : - wave length in vacuum; n_M : - refraction index of the surrounding medium

b_i : - diffuse light term, abbreviation of a complicated function

ϕ_i : - phase delay

By classifying the measured radii, a distribution of occurrence frequencies of the diameter classes can be obtained.

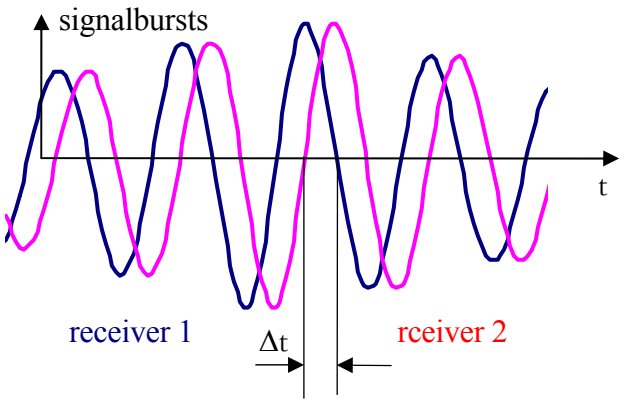

Figure 3.2.8 PDA measurement signal

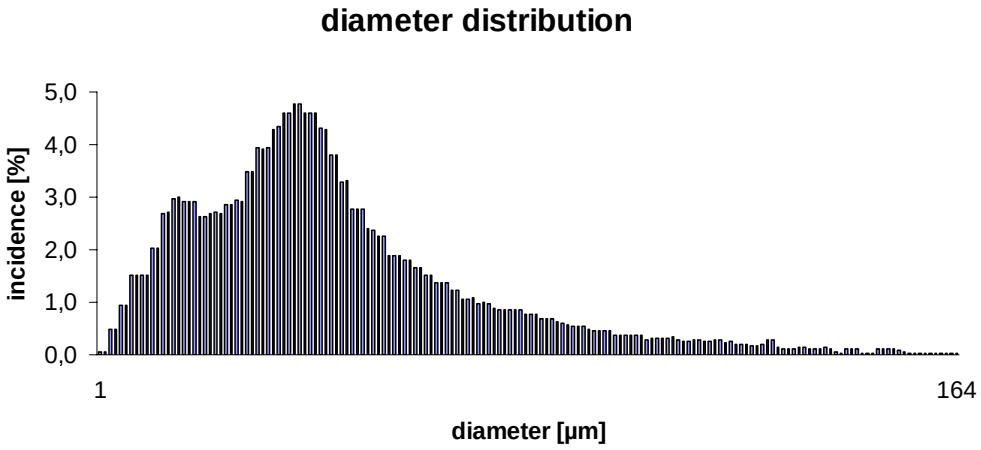

Figure 3.2.9 PDA result

In principal, PDA is an absolute measurement method. However, calibration with test particles is intended. Within the measuring range, complete nucleus spectra are measured in-situ and reactionlessly. The local resolution is determined by the volume measurand, that is by diameter and crossing angle of the laser beams. However, this method cannot distinguish between gas bubbles and solid particles. Measurement uncertainty increases in the order velocity, particle size and concentration.

3.2.4.8 Comparison between Holographic Mapping, Centerbody and PDA

An experimental study was conducted (Gindroz [1992]) in order to compare the three previously mentioned measurement methods for determining nucleus spectra. These systems are installed in line, along a special Perspex tube with optical glass windows, to guarantee similar flow conditions. The comparison is made for different nuclei distributions and flow conditions.

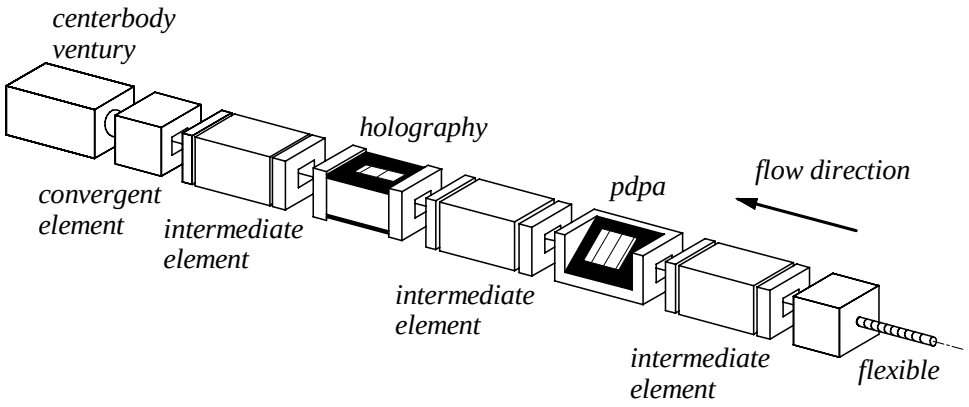

Figure 3.2.10 Installation for comparative nuclei measurements after Gindroz [1992]

First, the in-line installation is tested to determine the pressure and flow ranges that guarantee a correct operation, without leak of water or air suction. If such a problem appears during the comparative tests, the water sample would not be similar for each nuclei measuring technique.

Then, the in-line installation is connected to a test rig, with nuclei control. Several series of measurements are performed, with degassed water, without and with nuclei injection, for different pressure and flow levels. The demineralized test water, filtered at 10μm, is characterized by a measured surface tension of 71 mN/m at 20°C.

The content is represented in concentration relative to the maximum value corresponding to nuclei injection. There is a major problem concerning the absolute concentration levels. Indeed, they are not comparable.

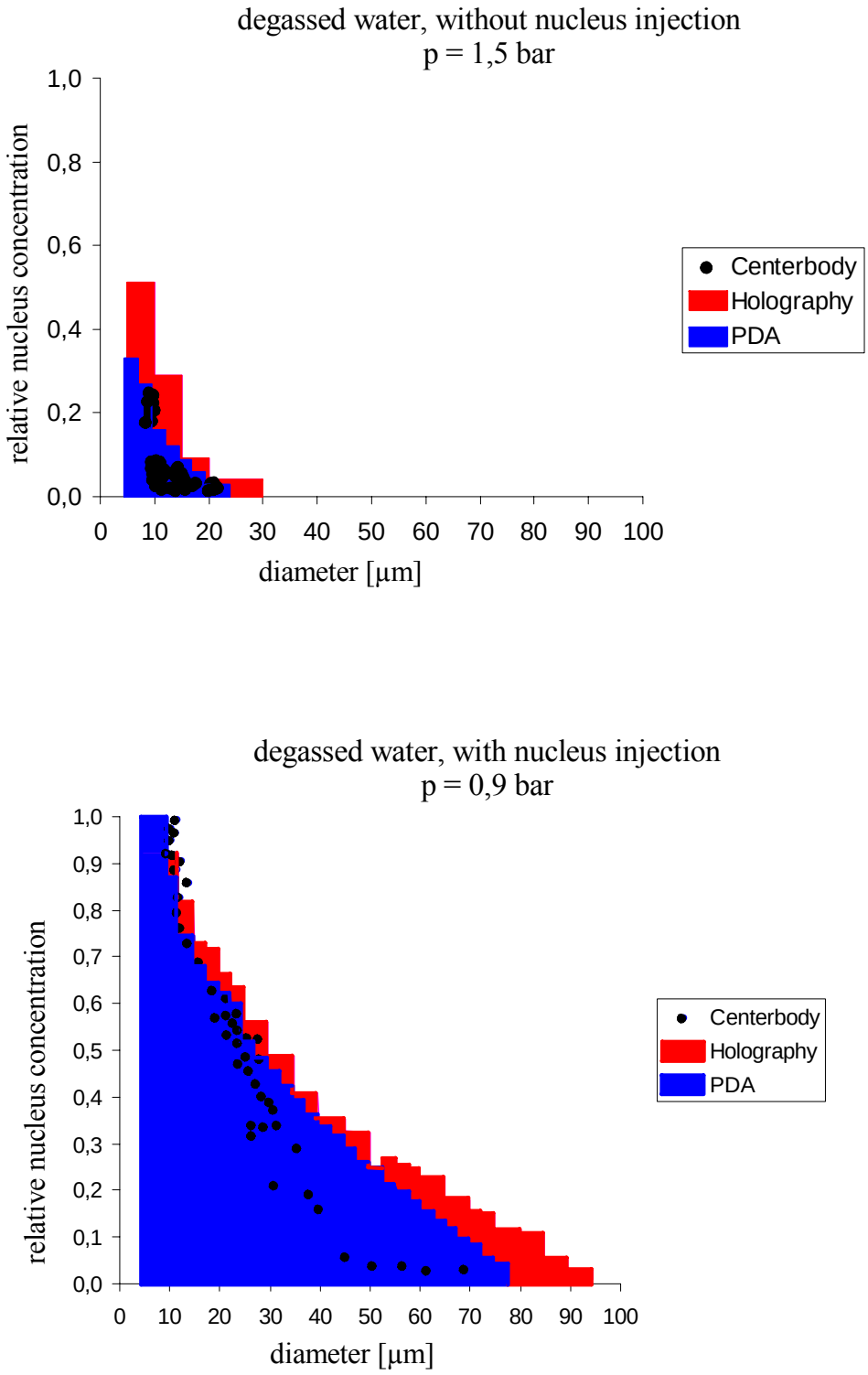

Figure 3.2.11 Comparison of the relative nucleus concentration after Gindroz [1992]

Figure 3.2.11 shows the results of two parallel measurements of nucleus concentrations, depicted as relative nucleus concentrations, i.e. in relation to the maximum value of nucleus injection. Apparently, the graphs are qualitatively similar. Compared to holography, PDA exhibits a

divergence at large diameter, which can be explained with the capacity of the measuring volume. Centerbody Venturi already shows differences at distinctly smaller diameters, which can be traced to the available free flow diameter (see chapter 3.2.4.6).

The PDA is very easy to run and allows quasi-real time measurements of nuclei content and their velocity. But the disadvantage of a very restricted and not well-known measuring volume does not lead to a direct spatial mean value of the nuclei content in the flow.

Holography is still a reference technique in granulometry, but it presents a major disadvantage, due to the long analysing time of the holograms. Moreover, the mean value obtained with a hologram, does not correspond to a temporal mean concentration, as the hologram is recorded at one precise time. For these reasons, it is not reasonable to include this technique as a standard real-time process during tunnel tests.

Regarding to the Centerbody Venturi, it is necessary to determine precisely the lowest pressure value inside the instrument, to define correctly the characteristics of the detected nuclei. After a calibration of its inner pressure distribution, this nuclei count has a major advantage, as it detects only particles governing the cavitation developments. Moreover, it analyzes in real-time the quasi-total volume of the water sample by-passed from the main flow of a test rig.

4 Tensile Strength of Liquids

4.1 Introduction

The foundations concerning tensile strains in water were already laid by Leonhard Euler and Daniel Bernoulli in the 18th century. Euler formulated the equation of motion for frictionless flows,

$$\frac{\partial \vec{u}}{\partial t} + (\vec{u} \cdot \nabla)\vec{u} = -\frac{1}{\rho}\nabla p + \vec{f} \tag{4.1.1}$$

which was integrated by Bernoulli for the flow path:

$$\int_{S_1}^{S_2} \frac{\partial q}{\partial t} ds + \frac{1}{2} q^2 \Big|_{S_1}^{S_2} + \int_{S_1}^{S_2} \frac{dp}{\rho} + G\Big|_{S_1}^{S_2} = 0 \tag{4.1.2}$$

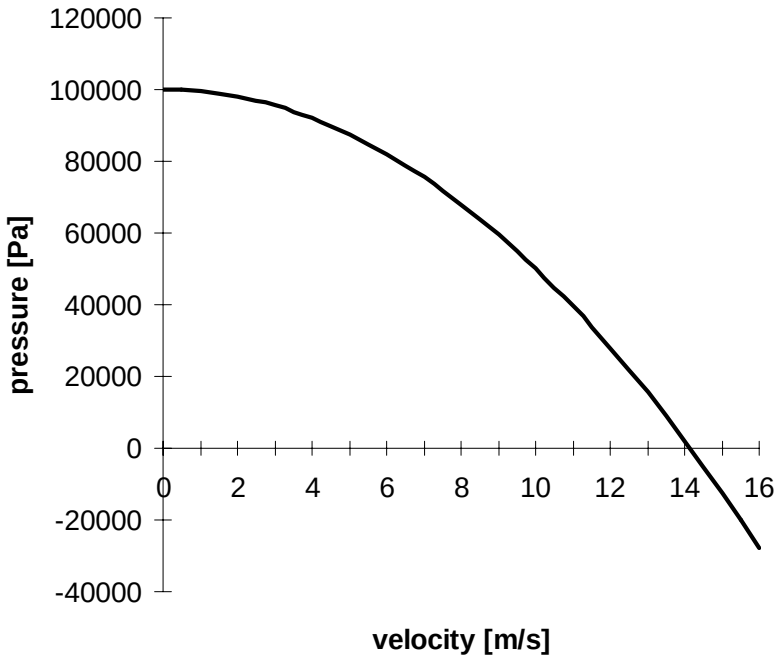

Figure 4.1.1: Pressure-velocity diagram for stationary and frictionless flow

This was the first mathematical relation between pressure and velocity concerning a fluid in motion. Bernoulli predicted negative pressures for sufficiently high velocities. These strains would be capable of breaking fluids, thus, causing cavities. As shown with a simple calculation, negative pressures can be produced in tubes with stationary and frictionless water flows $p_\infty = 10^5\,\mathrm{Pa}$ as soon as flow velocity exceeds $\approx 14\ \mathrm{m/s}$

The limit of bearable tensile strains of water could be estimated to 10^5 bar with the van der Waals equation (see chpt. 1.2). However, intermolecular forces can be severely weakened at interfaces to solid walls and therefore, other bonding forces or strains are effective here. Such theoretical tensile strains have therefore never been observed, even in purest water (see chpt. 2.2). The purity of the water plays a decisive role about bearable tensile strength. The tensile

strength values mentioned above, however, are significantly lowered by before-mentioned nucleus spectra or the nucleus content. Such nuclei represent inhomogeneities and therefore act as canters of boiling within the water. Since there is no need for fluid to break, for interfaces between liquid and gaseous phase are already present, significantly lower tensile strength values that are necessary for boiling are effective.

A difficult fundamental problem is expressed by the question of how low the pressure in water can sink, depending on the nucleus and gas content. Solving the problem theoretically can only be achieved by means of molecular physics. For practical application, however, such a sufficiently accurate analysis seems to be hopeless regarding the complicated molecular structure of nuclei-laden water. Alongside theoretical works, experimental methods to measure tensile strength in fluids have been devised. This development started in the 19th century with simple statistical methods that were continued and improved until the middle of the 20th century. In the advent of the 1970s, the development of dynamic methods began and has continued until today.

The highest tensile strains ever measured were obtained by Briggs [1953] using rotating, Z-shaped tubes (see chapter 4.2.4). This so-called centrifugal method was first employed by Reynolds [1878] (see chapter 4.2.3). As for water, he had reached tensile strength up to 4.8 bar, in contrast to Briggs who had reached up to 280 bar for water (see table 4.2.1), 310 bar for hydrocarbon (chloroform) and no less than 425 bar for mercury. This is likely to be the highest value of tensile strength ever measured for a fluid. Dixon [1909] reported tensile strains of 200 bar realized in cell sap using a Berthelot tube (see chapter 4.2.2).

Vincent [1943] reported tensile strength measurements of 119 bar in mineral oil and 157 bar in water. Using the same mineral oil, which he had previously tested with the original and the advanced Berthelot method, he obtained a maximum tensile strength value of only 7.8 bar with the so-called tonometer method. A fluid that is cooling down is drawn through a thin tube and the critical tensile strength is calculated from the flow rate just before and after the breakaway of the flow. In another experimental series, Vincent [1941] directly applied tensile strains to fluids by enclosing them into a metal bellows. Thus, he obtained 2.4 bar in ethyl alcohol and about 3 bar in mineral oil.

In this account the works of Kenrick, Wismer and Wyatt [1924] should also be mentioned, who saturated fluids with gas at pressures of about 100 bar and then reduced it to atmospheric pressure without letting the fluid froth up. These works, as well as Apfel's [1970] work, which achieved an overheating of water to 270°C at atmospheric pressure, should be included here because a fluid being overheated or saturated with gas is subject to similar strains as a fluid under tensile strength. Additionally, the experiments by Budget [1912] shall be listed here, who measured the force necessary to pull apart wet, optically plain steel surfaces. With a number of assumptions, he estimated the critical tensile strength applicable to water to about 60 bar.

Subsequently, the most important measurement methods will be presented and their results discussed.

4.2 Static Measurements of Tensile Strains

(excerpts after "Cavitation & Tension in Liquids" by D. H. Trevena ISBN 0-85274-454-4, 1987)

4.2.1 U-Tube by Donny

Francois Donny was a professor of industrial chemistry at the University of Gent. His work from 1844 showed that it was possible for a liquid at rest to sustain a tension.

Donny used a U-shaped glass tube one arm of which was sealed. The closed arm was completely filled with air-free sulphuric acid while the acid rose in the open arm to a height of 45 mm such that there was a difference of height of 1.3 m between the two liquid columns. He placed this U-tube into a large sealed glass cylinder that was connected to his air pump. After removing most of the air from the cylinder, such that the residual pressure was only about 5 mm of acid, the liquid still continued to fill the whole of the closed arm. In this case the tension at the top of this closed column was about a quarter of an atmosphere. He also made the point that still grater tensions could be generated in this kind of apparatus.
Specific weight of sulfuric acid is 1.84 g/cm³.

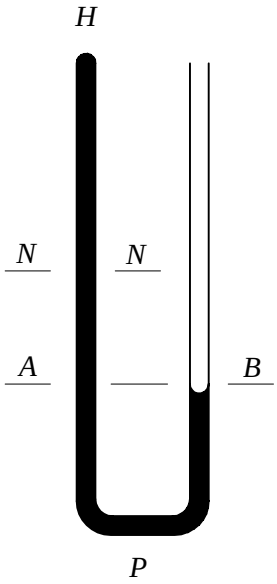

Figure 4.2.1: U-Tube by Donny [1846]

He then repeated the whole procedure with acid that was not completely free off dissolved air. It was found that, once the air pressure in the sealed cylinder started to fall, a large number of tiny bubbles appeared in the closed column and the column itself began to fall with a consequent release of the tension in it. So Donny's work illustrated this important point: when a liquid contains dissolved gas its ability to sustain tension is reduced and when this tension is increased sufficiently the liquid will eventually break with the appearance of tiny bubbles.

4.2.2 Berthelot-Tube Method

The next important work for us to consider was that carried out in 1850 at the Collège de France by Marcellin Berthelot, the prolific and celebrated chemist. Berthelot was a professor of organic chemisty at the Collège and occupied this chair until his death in 1907. His first scientific paper, published in 1850 whilst he was still a young research student, described some work which showed that it was possible for a liquid in a sealed tube to withstand a tension of the order of tens of atmospheres before it cavitated. We now know this experiment as the "Berthelot tube method".

Figure 4.2.2: Marcellin Berthelot (1825 – 1907)

Berthelot used a glass tube which was cylindrical in shape. At ordinary room temperature it was almost completely filled with the liquid, the remaining volume being occupied by air and the liquid vapour. When the tube and its contents were heated the liquid expanded at a greater rate than the Berthelot tube, the air was forced into solution and the liquid filled the tube completely at a certain temperature T_0. When the tube was subsequently allowed to cool the liquid adhered to the walls of the tube and continued to fill it at temperatures below T_0 .Thus as the temperature fell below T_0 a gradually increasing tension was built up in the liquid until it eventually broke at a lower temperature T_b. At the instant of fracture the sudden release of tension was accompanied by a metallic click and a sudden increase ΔV in the external volume of the Berthelot tube; by measuring ΔV the critical or breaking tension just before fracture could be determined. The various stages in a Berthelot tube experiment are shown in figure 4.2.3.

In his original work using water in a glass tube Berthelot found that the volume of the water in the tube had increased by 1 part in 120 just before cavitation occurred and he estimated that the tension in the water at the same instant was about 50 atmospheres. He noted that the cavitation started at the wall of the tube and concluded that the maximum tension generated before the break was a measure of the adhesion of the liquid to the inside wall of the tube rather than the true tensile strength of the liquid.

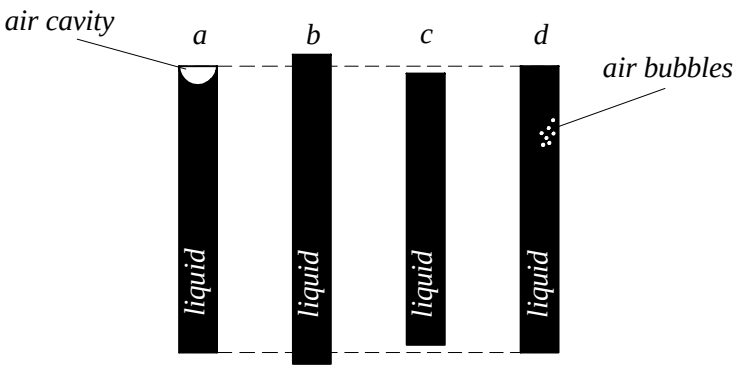

Figure 4.2.3: a) Berthelot tube at room temperature containing liquid and a small volume of air and liquid vapour.
b) Tube after being heated until the liquid just fills it at the temperature T_0 and
c) the liquid is subjected to a gradually increasing tension.
d) Tube and contents after the break.

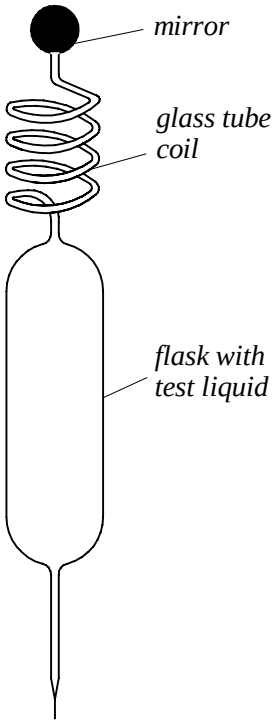

Figure 4.2.4: Meyer's modification of the Berthelot tube [1911]

Berthelot's original experiment was carried out in 1850. Since then the Berthelot tube method has been used intermittently, and with varying degrees of modification, by a number of workers. An interesting modification of the Berthelot tube was used, much later, by Meyer [1911]. This is shown in figure 4.2.4. The glass at one end of a Berthelot tube was drawn out into a fine spiral tube and a small mirror was attached to the end of the spiral. The tube was then filled with the test liquid and the other end sealed as in an ordinary Berthelot tube. Prior to this sealing, known positive pressures were applied to the inside of the tube and the corresponding angles of twist of the spiral were measured using a beam of light focused on the mirror.

Evans [1979] reverted to using a glass Berthelot tube. One reason for this was that he was anxious to observe the test liquid after fracture. Initially he experimented with strain gauges cemented to the outside of straight glass tubes but it was found that the strains obtained were much too small to allow an accurate estimate of the internal pressure. The problem was solved by dispensing with the requirement for the tube to be straight and using instead a glass tube in the form of a spiral, as was first done by Meyer in 1911.

In his work Evans used a long Pyrex glass tube which was formed, before filling, into a spiral consisting of an odd number of half circles so that the ends were parallel and pointing in the same direction.

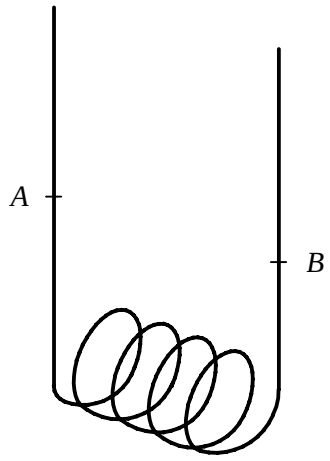

Figure 4.2.5: Evans' modification of the Berthelot tube [1979]

Internal pressure causes the coil to unwind slightly so that the two ends separate; conversely internal tension brings them closer together. The crux of the method was to monitor changes in the separation of the tube ends and to relate these changes to pressure changes in the liquid inside the tube. Evans used a capacitance distance meter to measure this seperation. The spiral was immersed in a water bath, whose temperature could be varied.

If there are n loops in the spiral the total angle through which the tube is formed is (2n + 1)□ radians. In the simplest case, n = 0 would give a simple U-tube. In most of his work Evans used a spiral for which n = 4, that is, a 9□ configuration as shown in figure 4.2.5. In this simplified diagram of the tube the test liquid occupied the region between the two sealed ends at A and B. This sealed part of the tube contained the test liquid and a few air bubbles at various points in the spiral. In an actual experiment the spiral was heated until the last bubble, as viewed through a microscope, had been forced into solution. The cooling process then commenced. The pressure signal was applied to the ordinate of an X-Y recorder and a temperature signal to the abscissa.

One of the great advantages of the method is that the final disappearance of the bubbles on heating can be observed visually as can also the origin of the cavitation bubbles after the break. The breaking tensions obtained for water-in-glass were in the range 30-50 bar. A similar method was also used by Henderson and Speedy [1980]. A Pyrex capillary wound in a spiral was filled with water and sealed. The two ends of the spiral were on the same vertical axis; figure 4.2.6 shows the essential arrangement.

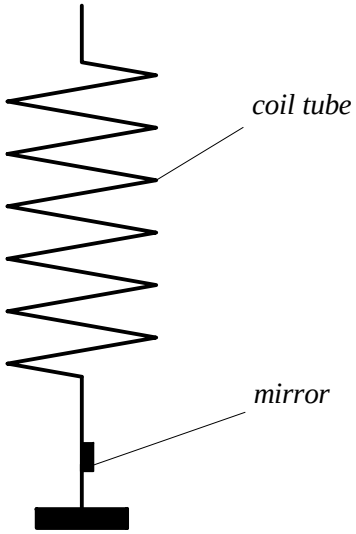

Figure 4.2.6: Hendersons' and Speedy's modification of the Berthelot tube [1980]

Temperature was measured using a thermocouple. Pressure measurements were made using a laser beam reflected from a mirror attached beneath the spiral; the angle of twist of the tube, as obtained from the angular displacement of the laser beam, was a measure of the pressure. The outer diameter of the spiral tube was about 0,5 mm and the internal diameter about a half of this. The total volume of the test liquid in the tube was only 2 to 4 mm^3; this had the advantage that such a small liquid specimen would not contain many nucleation points in the bulk liquid.

The spiral was surrounded by a vertical cylindrical double-walled glass jacket (not shown) which contained a circulating thermostating fluid. This arrangement controlled the temperature of the test liquid, the jacket playing the same role as the bath in the experiments of Evans. With this apparatus, Henderson and Speedy obtained tensions up to 160 bar before cavitation occurred.

4.2.3 Reynolds' J-Tube

In 1878 Osborne Reynolds carried out some experiments which were, in fact, a development of Donny's work. He used a vertical glass tube, 60 inches long and closed at the upper end. This tube was almost completely filled with mercury with a small volume of dilute sulphuric acid., above the mercury, occupying the remainder of the tube. With this arrangement, provided no air bubbles were present, he found that the vertical column of 60 inches would fill the tube and remain intact any sing of fracture. This meant that the tension in the liquid at the top of the filled tube was nearly one atmosphere.

A centrifugal method of applying tension to a liquid was also used by Reynolds. His liquid was contained in a glass J-tube such as that shown in figure 4.2.7. The long arm was open to the atmosphere and the short one was sealed

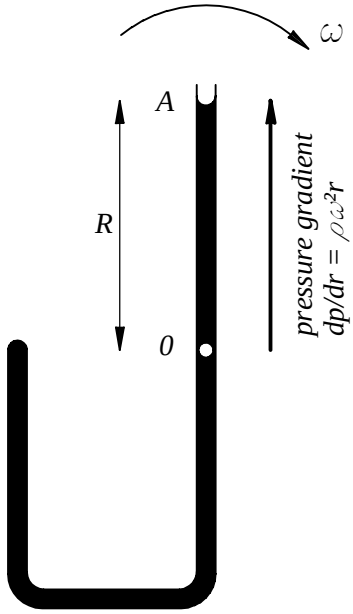

Figure 4.2.7: Reynolds' J-Tube [1878]

If such a tube is rotated with angular velocity ω about an axis O perpendicular to the horizontal plane containing the tube axis, a pressure gradient of $dp/dr = \rho\omega^2 r$ is generated in the direction OA, where r is the distance from O. Since the pressure p_A at A is always atmospheric it follows that the pressure p_O at O is less than atmospheric and we have

$$p_A - p_0 = \int_O^R \rho\omega^2 r \, dr = \frac{\rho}{2}\omega^2 R^2 \tag{4.2.1}$$

where OA = R

Thus:

$$p_O = p_A - \frac{\rho}{2}\omega^2 R^2 \tag{4.2.2}$$

So, if ω sufficiently large, p_O becomes negative, that is tension sets in, and when ω reaches a certain critical value ω_{krit} , the value of the breaking tension can be calculated. Using this method Reynolds obtained a value of 4,8 atmospheres for the breaking tension of water. A few years later, in 1892, applied the same method to obtain a corresponding value of 7,9 atmospheres for ethyl alcohol.

4.2.4 Briggs' Z-Tube

Briggs (1950) also used the centrifugal method. In his work the liquid was held in a Z-shaped Pyrex capillary, of internal diameter 0,6 mm and open at both ends. This Z-tube was mounted horizontally and spun in its plane about a vertical axis through its centre.

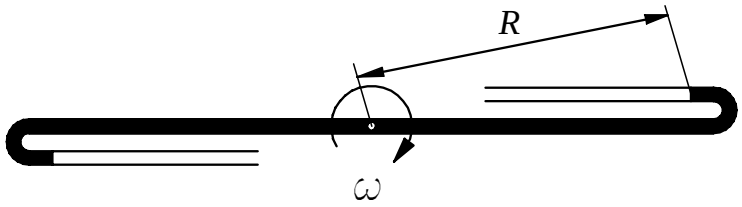

Figure 4.2.8: Briggs' Z-Tube [1950]

With this arrangement the liquid column at this central point was visible even at high angular speeds. The tube was enclosed in a cylinder, with a glass plate on top; when operating, the air pressure was reduced at about 30 mmHg. In the centrifugal field, one half of the liquid column was pulling against the other and the maximum stress, which was at the centre, was given by

$$p_{min} = p_0 - \frac{\rho}{2}\omega^2 R^2 \tag{4.2.3}$$

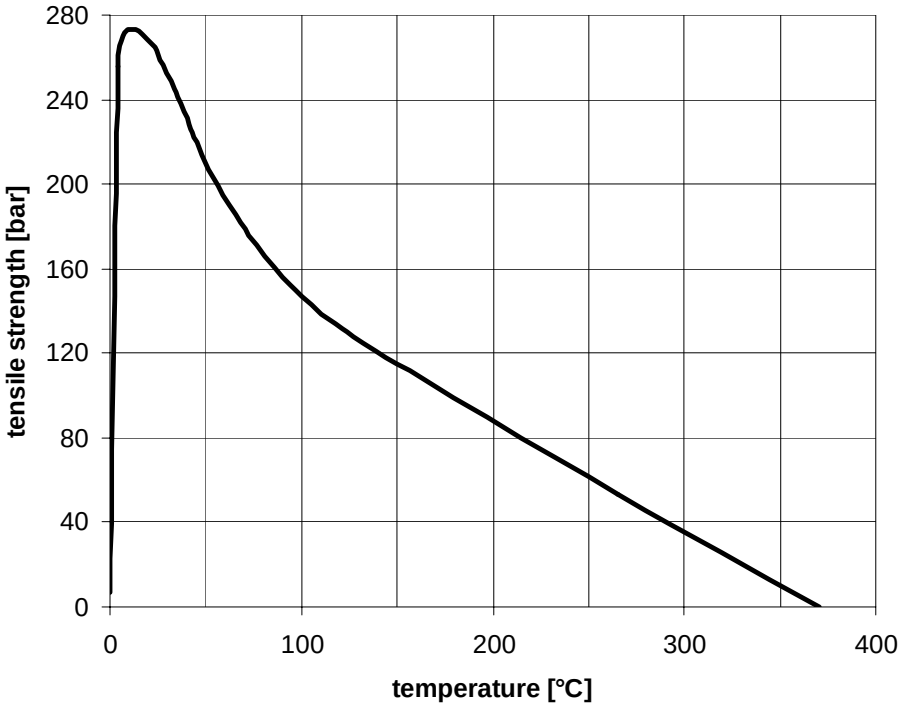

Figure 4.2.9: Results of Briggs [1950]

As in Reynolds' work, the breaking tension could be calculated from the value of ω which caused the liquid column to break at its centre. Briggs emphasized the need for scrupulous cleanliness in this work and the open-ended tube possessed the great advantage of being easy to clean and fill. His results for distilled water are shown in figure 4.2.9. This graph shows that the breaking tension had a maximum value of 277 bar around 10°C and that it decreased to 217 bar as the temperature rose to 50°C.

So although the van der Waals equation does not represent (see chpt. 1.2) the behavior of water quantitatively, it nevertheless gives a fair indication that a decrease in p_{min} with increasing temperature is to be expected. The graph also shows a rapid fall in the value of p_{min} as the temperature fell from 5 to 0°C.

To clarify this decline of p_{min}, Moerch [1999] introduced a model about voids being attached to solid surfaces. This model explains tensile stress maximum at 10°C, based on molecular forces in the fluid interface in places with convex surface of the solid. Here the number of fluid molecule layers with inclination to the hexagonal ice-1 structure will tend to grow if the temperature approaches the freezing point (see Franks [1984]). This is why the fluid layers closest to the solid surface are under additional strain in places with concave structure. Molecular bonds break and already allow the formation of voids if the fluid sustains only little tensile strains.

Briggs emphasised that with this method one could not tell whether the fracture of the column originated on the wall of the capillary (loss of adhesion) or in the body of the liquid (loss of cohesion). His value of 277 bar represents an "all-time high" experimental value for the breaking tension of water. No doubt the relatively low values of pmin obtained by previous workers using the centrifugal method were due to the lack of sufficiently clean conditions in their apparatus.

Strube and Lauterborn [1970] developed the method to study cavitation nuclei at the interface between quartz glass and pure degassed water. The maximum breaking tension observed was 175 bar and they found that the gas content of the water did not play a discernible part (thus implying that "loss of cohesion" was not the important factor in the experiment).

4.2.5 Discussion of Measurement Results and Methods

An analysis of Vincent's measured results clearly shows how widely the values of tensile strains are spread (see table 4.2.1). For one and the same fluid (mineral oil), highly different results were obtained with various measurment methods. In this case, values ranged between 2.9 bar and 119 bar as shown in the table. A similar spread of results can be observed regarding the measured tensile strains of water. Nevertheless, all values are far below the theoretically possible value. It can explicitly be concluded that the properties of the fluid's bounds (walls) play an important role limiting the fluid's maximum tensile strength.

The work of Temperley and Chambers [1946] provides a concise analysis of tensile strains that had been measured to that date by scrutinizing measurements with both the Berthelot tube and the Reynolds Z-tube method. In their work some measurements are corrected and the following "true" tensile strains for water are given:

in the presence of glass: maximum 68 bar, minimum 2 bar; average 32 bar,
in the presence of steel: maximum 23 bar; minimum 2 bar; average 12 bar.

However, these corrections could equally not account for the influence of the container walls. Furthermore, Temperley and Chambers discussed the centrifugal method and claimed in their result that this method would not be suitable to induce high tensile stresses since due to the pressure gradient, small nucleus bubbles would always be drawn to the rotation axis and thus, limit tensile stresses.

Nevertheless, later Briggs reached the highest tensile stresses shown in table 4.2.1 with just this method, though slightly modified. However, it cannot be determined whether these tensile stresses were finally limited by a breakaway of cohesion within the fluid or a breakaway of adhesion at the contact area of water and glass. Eventually, the fact remains that even those extreme tensile strengths measurements are far below the theoretically possible values of strength.

liquid	method	tensile strength [bar]	researcher	year
water	glas Berthelot tube	50	Berthelot	1850
water	U-tube	4,8	Reynolds	1878
alcohol	U-tube	7,9	Worthington	1892
water	glas Berthelot tube	50-100	Dixon u. Jolly	1895, 1909
water	U-tube	34	Meyer	1911
alcohol	U-tube	39	Meyer	1911
ether	U-tube	72	Meyer	1911
cell sap	glas Berthelot tube	50-200	Dixon	1914
mineral oil	metal bellows	2,9	Vincent	1941
mineral oil	Tonometer	1,6-7,8	Vincent	1943
mineral oil	glas Berthelot tube	119	Vincent	1943
water	glas Berthelot tube	157	Vincent	1943
water/steel particle	glas Berthelot tube	68	Temperley	1946
water	glas Berthelot tube	56	Scott	1948
water	Z-tube	150-280	Briggs	1953
mercury	Z-tube	425	Briggs	1953
hydrocarbon	Z-tube	130-310	Briggs	1953
water	glas Berthelot tube	13	Rees u. Trevena	1966, 1967
carbon tetrachloride	steel-Berthelot-tube	15	Rees u. Trevena	1966, 1967
aniline	steel-Berthelot-tube	21	Rees u. Trevena	1966, 1967
liquid paraffin	steel-Berthelot-tube	22-29	Rees u. Trevena	1966, 1967
water	Z-tube	63-175	Lauterborn	1969, 1970
mineral oil	metal bellows	62	Floberg	1973

Table 4.2.1: Overview of static tensile strength measurements after Keller [1980]

4.3 Dynamic Tensile Strength Measurements

4.3.1 Introduction

Two ways to determine tensile strains under dynamic strain will be described. Firstly, positive and negative pressure waves are induced in resting fluids. It is a discontinuous measurement process because a certain amount of a resting fluid is investigated in an apparatus. Secondly, a fluid streaming through an experimentation device is accelerated until local vaporization begins. This is a continuous measurement process.

Temperley and Chambers [1946] were the first to report about tensile strains in water under dynamic strain and mentioned that a momentary tensile strength of about 15 bar had been measured near an explosion, whereas Cole [1948] and Kolsky [1949] estimated the critical tensile strength of water to 20 bar under these circumstances. Here, the measurment method is based on the reflection principle. An explosion in deep water produces a shockwave. Behind this practically discontinuous pressure front, the pressure is decreasing proportionally to time and distance. Apart from the region near the explosion, the propagation speed (speed of sound) is nearly constant and acoustic theory provides a suitable approximation. Such pressure waves induce strains to water surfaces as well as ship walls, for example. These tensile strains can be inferred from wave formations at the water's surface by means of optical methods.

Harvey [1946] reported tensile strength experiments in which glass sticks were moved through a fluid at high speed. Leaving only a small gap between glass stick and the container walls, this system works similar to a leakier piston. Although, there are no clear specifications about the tensile strains reached, they are estimated to a maximum of 100 bar.

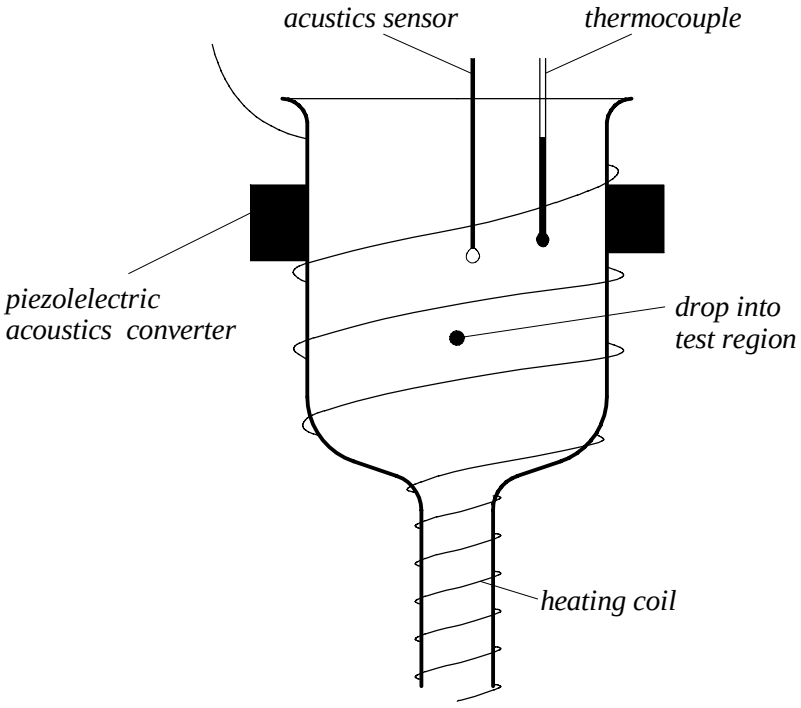

Figure 4.3.1.: Gadget by Apfel [1971]

An interesting method to measure tensile strains in overheated fluids in described by Apfel [1971, 1972]. A fluid droplet rising in glycerin is overheated and exposed to a sound wave of high intensity (see fig. 4.3.1). At sufficiently high alternating tensile strength, the droplet reaches its tensile strength limit and evaporates explosively. Overheating to 135°C combined with acoustic excitation at 50 kHz produced tensile stress measurements up to 200 bar.

Lackmé [1978] used a very direct and novel way of applying a tension to a liquid. The essential part of his apparatus is shown in figure 4.3.2. A test specimen of water was contained in a sealed thick-walled tube, mounted with its axis vertical. The axial length of the enclosed liquid column was 40 mm and its radius 10 mm. At its lower end the liquid column was supported by a vertical cylindrical aluminium bar B and a similar bar A rested flush on top of the liquid. A tension pulse was propagated into the liquid at its lower end. This was done by fixing a circular plate to the bottom end of the bar B and then causing a ring-shaped weight RR to fall on to this plate. The impact of the weight caused a stress wave up the bar B and produce a tension pulse at the base of the liquid column. This pulse, after travelling up through the liquid, was transmitted into the upper bar A.

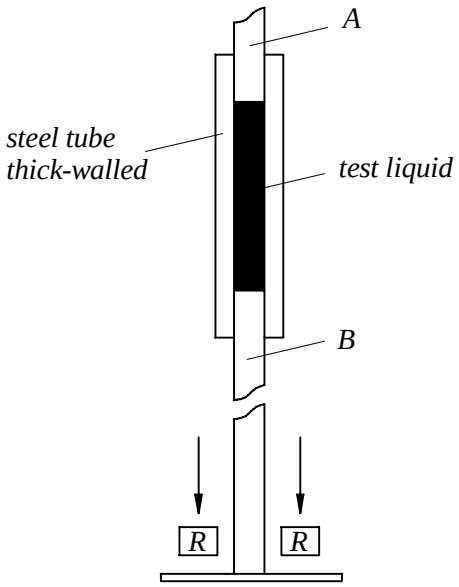

Figure 4.3.2.: Lackmé's apparatus [1978]

A strain gauge mounted on bar B recorded the incident pulse entering the lower end of the liquid and a similar gauge on bar A recorded the transmitted pulse. The duration of the incident pulse was about 100 μs and its amplitude could be varied by changing the height of fall of the weight RR. With the experimental set-up, tensions of up to 5 bar could be transmitted through the water column. Lackmé emphasises that this value was not that of the breaking tension but rather that of the maximum tension that could be generated in his apparatus. The method however seems to be a very promising one and has been extended further by Favreau [1984].

Additionally, high-energy ultra-sonic cavitation experiments shall be mentioned here. However, since these are periodically changing pressure-tension stresses in connection with effects such as resonance vibration and directed diffusion, this special group of dynamically changing strain of fluids will not be discussed in detail here. All other dynamic tensile stress measurements in resting fluids have been carried out in the so-called shock tube (see the following chapter 4.3.2).

4.3.2 The Shock Tube

In high-speed aerodynamic experiments the shockwave tube as reactor for gas kinetic research is utilized. It is based on the nearly instant thermodynamic change of state that occurs in a gas mixture when a perpendicular density shock (shock wave) travels through it. By means of the shock wave tube, gases can easily be heated to high temperatures and measurements can be carried out under isothermic and isobaric conditions.

A shock wave tube consists of a long tube, which is divided by a membrane into a push tube and a running tube. Prior to the experiment, the gas mixture to be investigated is injected into the previously evacuated running tube (low pressure part). Then the push tube (high pressure part) is filled with a rather light fuel gas such as hydrogen or helium until the membrane bursts. After the break of the membrane, a plane shock wave is established, spreading at super-sonic speed through the resting experimental gas, which is abruptly pressurized, accelerated and heated. The temperature and pressure levels of the experiment can be controlled with the strength of the membrane and the initial fuel gas pressure. Normally, the measurement takes place after the reflection of the shock wave at the end-flange in the then resting gas.

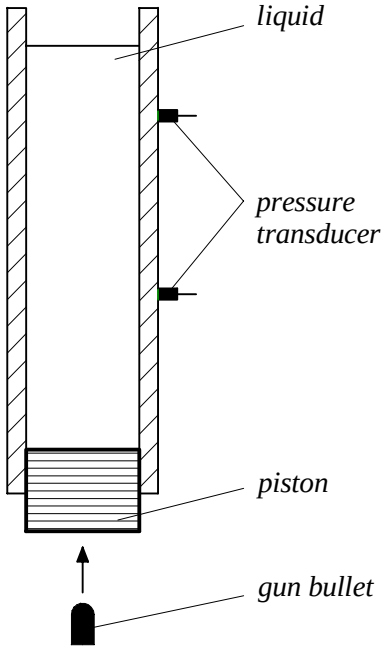

Figure 4.3.3: Sketch of a shock tube with bullet-piston combination after Trevena [1987]

In comparison to the shock wave tube for gas dynamic measurements, the shock tube consists of a vertical steel or glass tube, whose lower end is closed with a piston or plate. After filling the tube with the test liquid, a shock is inflicted on the piston or plate, for instance by means of a hammer or a bullet being fired at the piston (see fig. 4.3.2). This shock creates a shock wave traveling upwards through the tube. It is reflected at the liquid's surface (interface liquid-gas) as a

negative pressure wave and thus, produces tensile strains and cavitation. The pressures occurring within the negative pressure wave are measured with transducers and the tensile strains calculated. The pressure change Δp due to the negative pressure wave can be calculated according to the unsteady (non-stationary) airflow theory from the Euler equation with the shock pressure formula:

$$\Delta p = -\rho \cdot a \cdot \Delta q \tag{4.3.1}$$

with:
ρ - density of the liquid
a - sound velocity in the liquid in an elastic tube
Δq - velocity change of the liquid

liquid	method	tensile strength [bar]	researcher	year
oil	shock tube	8,9	Briggs	1947
water	shock tube	18	Bull	1955
glycerin	shock tube	63	Bull	1955
cell sap	shock tube	130	Bull	1956
oliven oll	shock tube	29	Bull	1956
water	shock tube	9	Devies	1956
water	shock tube	7	Trevena	1964
cell sap	shock tube	62	Rees	1965
water	shock tube	20 - 37	Brown	1967

Table 4.3.1: Overview of tensile strength measurements using the shock tube after Keller [1980]

The tensile strains for water determined using the shock tube method range between 7 bar (Trevena [1964]), 9 bar (Davies [1956]), 18 bar (Bull [1955]) and 20 – 37 bar (Brown [1967]). Here, the container walls also have a significant influence on the possible tensile strains (see chapter 4.2.5). The highest value was reached by Bull [1956] with 130 bar in syrup, as shown in table 4.3.1.

4.3.3 Flow around a Semicircular Body by Silberman & Schiebe

Silbermann & Schiebe [1973] presented a feasibility study about the possibilities to employ so-called standard bodies in order to measure the tensile strength of water. This method uses a mathematically defined, axially symmetric test body, for which an analytic model of a flow field could be developed. From the resulting pressure field, the tensile strains effective on any nucleus near the body in this flow field are computed. The equations for motion and stability of a bubble or a solid particle determine the nuclei's path and therefore the tensile strength of the fluid.

For the practical application of this technique, test bodies were developed that induce flow and pressure fields in their surrounding that are suitable for experimental research and that can equally well be described analytically. According to potential theory, in flow fields every surface or solid wall can be regarded as stream surface or streamline. In the simple case of a body produced by a point source in parallel flow, the body's shape is represented by the stream surface around the front stagnation point. A suitable variable by which a body may be classified is given by its minimum pressure coefficient $c_{p,min}$.

However, the body's shape is not the only variable that must be taken into account. The chance of nucleus formation at surfaces should be limited as much as possible. Therefore, smooth, treated and hydrophilic surfaces are of particular importance. After the test body had been selected, in an experiment the formation of gas bubbles and their collapse respectively could be detected acoustically. Afterwards, the analytic model was adjusted according to these pre-conditions. Thus, Silbermann & Schiebe obtained an analytic transformation model that enabled them to link the experimentally obtained data from carefully selected test bodies with the size distribution of the bubbles in the flow field.

4.3.4 Venturi Nozzle by Oldenziel

The technology subsequently described was presented by Oldenziel [1979] to determine tensile strains in water dynamically. In a flow through the narrowest cross section of a Venturi nozzle, high velocities and low pressures respectively are reached. With the diameter of the test tube d_0 and the diameter of the Venturi nozzle d(x), the pressure is given as a function of the place x.:

$$p(x) = p_0 - 8\frac{\rho \dot{V}^2}{\pi^2 d_0^4}\left[\frac{d_0^4}{d^4(x)} - 1\right] \tag{4.3.2}$$

where p(x) is the local pressure at the narrowest cross section of the Venturi nozzle and p_0 is the measured pressure at the upstream side of the Venturi nozzle. $\dot{V}$ denominates the throughput or the volume flow in the system.

The function d(x) is given by:

$$d(x) = d_t \cdot \cosh(kx) \tag{4.3.3}$$

with d_t being the diameter at the narrowest cross section, and k is about 40 m^{-1}.
The Venturi nozzle in figure 4.3.4 is depicted with this value k.

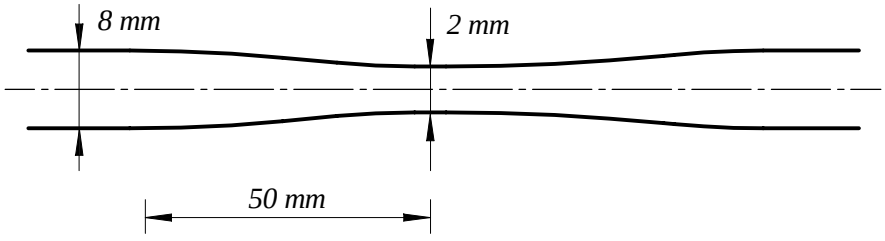

Figure 4.3.4: Shape of the Venturi nozzle after Oldenziel [1979]

The measurements of tensile strength in water were conducted with a Venturi nozzle made of glass (fig. 4.3.4). A container where pressure can be controlled is attached to the downstream side of the Venturi nozzle via a glass tube of 0.5 m in length. The Venturi nozzle where the formation and collapse of steam bubbles takes place is called cavitation Venturi nozzle (see chpt. 5.3 and fig. 4.3.5). The flow through the system was measured by means of a second Venturi nozzle. The diameter of this Venturi nozzle is significantly wider than that of the cavitation Venturi nozzle, so that no vapor bubbles can be formed there.

The vapor bubbles are collected optically by means of the so-called shadow method (see analogy in chpt. 3.2.4.4). This means that light source and photo diode are placed in line. With bubble-free flow, a certain light intensity is measured. If, however, a bubble exists within the measuring volume, light intensity will decrease, which is recorded electronically. This measurement method has a threshold because not all particles are to be counted. Dust, sand particles and other impurities that are not bubbles are not effective as evaporation nuclei and are therefore not counted. This threshold was set to 100 µm.

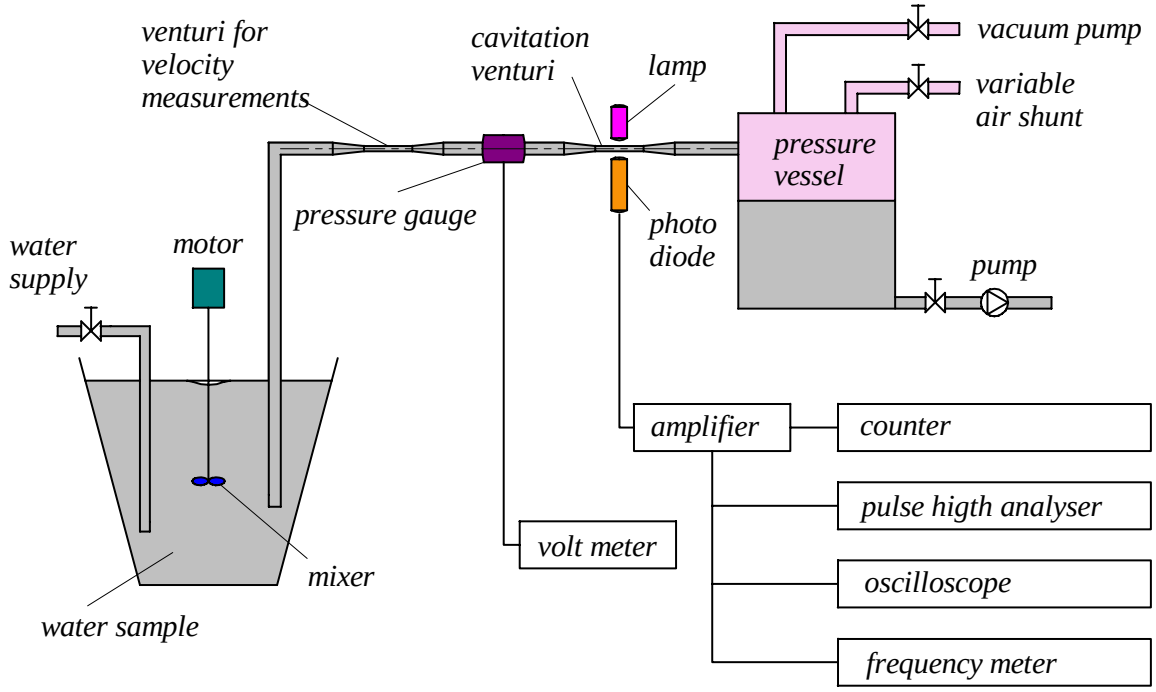

Figure 4.3.5: Layout of the tensile strength meter after Oldenziel [1979]

The advantage of using this tensile strength measuring device is the direct identification of a water sample's tensile strength (i.e. the tensile strength of the impurities enclosed in the fluid). This device only determines the tensile strength of the weakest impurity. There is no reason to assume that nuclei are affected by gas diffusion on their way from taking the sample to the Venturi nozzle. Pressure in this area almost equals the surrounding pressure.

At the test facility of the Delft Hydraulics Laboratory it was found for unfiltered urban water that tensile strains are about 120 kPa. After the water had been filtered with a 5 µm filter, susceptibility to cavitation was significantly lower at about 280 kPa.

4.3.5 In-situ Nozzle by Bachert

Cavitation (see chpts. 1.2 and 5.3) is to be created under defined and reproducible conditions while the static pressure at cavitation inception (=break of fluid) is measured. Until now this static pressure could not be measured directly at the narrowest cross section of a Venturi nozzle because a hole (such as for a pressure sensor) would disturb and affect cavitation inception and thus, not the exact static pressure at the break of the fluid would be measured. That is why the static pressure is indirectly determined with the Bernoulli equation, the static pressure being measured at the exit of the Venturi nozzle after the narrowest cross section and the respective velocity being known.

The value of tensile strength follows directly from the difference between the measured static pressure and the vapor pressure of the test fluid. The device that had been developed for just such measurements is based on the Venturi nozzle (compare chpt. 4.3.3). The principle of the so-called "in-situ" (in place, without change of place) is depicted in figure 4.3.6 (see Bachart et al. [2003]).

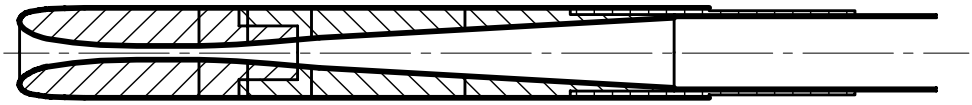

Figure 4.3.6: Principle of the "in-situ" nozzle after Bachart [2003]

During measurement, the nozzle is installed in a bypass directly at the place of interest in the test facility. The development of the nozzle was supported by CFD (Fluent). Initial measurements proved that practical research was in agreement with numerical results.

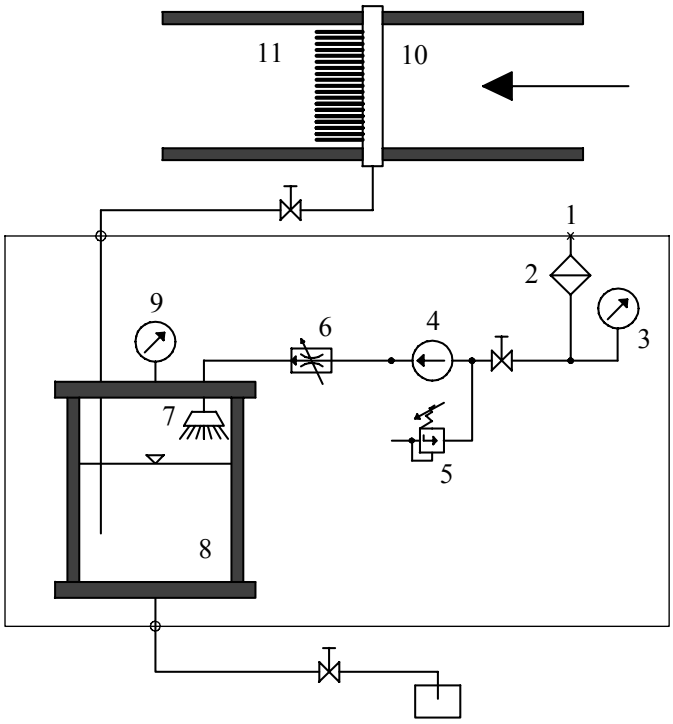

1 *taking out from the test loop*
2 *fine filter*
3 *pressure gauge*
4 *high pressure pump*
5 *pressure limitation valve*
6 *throttle valve*
7 *shower head*
8 *vessel serving as saturation tank*
9 *pressure gauge*
10 *micro bubble injector*
11 *inlet of the pump (test rig)*

Figure 4.3.7: System to produce micro-bubbles (schematically) after Bachert [2003]

Except for the opportunity to measure tensile strains, it is also necessary to control this parameter. In order to create testing conditions with various tensile strength values, a special system producing micro-bubbles was developed and installed in a second bypass of the test rig (fig. 4.3.7). This particular system consists of a high pressure pump, a small container, which serves as saturation tank, and a micro-bubble nozzle installed at the entry of the test rig.

Figure 4.3.8 shows the measured cavitation values at the break of the fluid at various gas contents. The results clearly show the dependency of tensile strains on the gas content: The higher the gas content, the greater are the cavitation numbers or put differently, the lower are the bearable tensile strains.

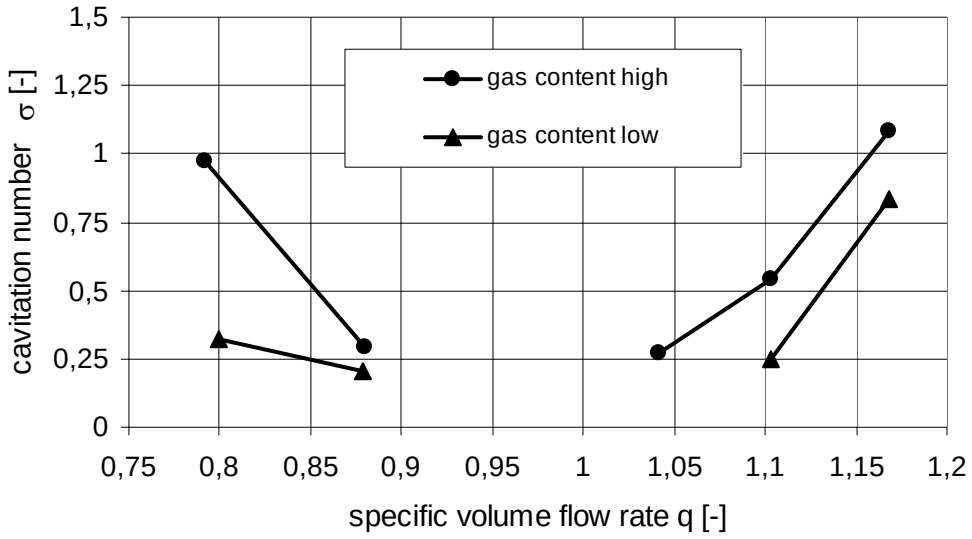

Figure 4.3.8: Cavitation inception at various gas contents after Bachert [2003]

4.3.6 Eddy Nozzle by Keller

In all the previously described static or dynamic tensile strength measurements, the walls' influence could not be prevented. To avoid these unwanted effects, tensile strength must be kept away from the container walls, which causes a negative pressure gradient from the container walls towards the flow center.

Keller [1983] was first to develop a method for the direct determination of the tensile strength of fluids according to the so-called eddy nozzle principle. Here, a defined turbulent flow is generated, overlayed by a known nozzle flow. Keller's observations were such that in flows around bodies, cavitation generally starts in the vortex centers of the interface. This holds both for the non-detached, turbulent interface at a streamlined body in the shear layer between two fluid flows as well as in the transition area of a laminarly detached boundary layer.

The vortex is generated in a so-called vortex chamber (see fig. 4.3.9). It mainly consists of a cylindric section into which the fluid flows tangentially and which is further connected to a conically narrowing part. In this configuration, the fluid is overlayed by a rotation defined by the inflow velocity. The lowest pressure occurs in the narrowest cross-section of the following Laval nozzle in the vortex center, namely in the center of the rotationally symmetric flow. Thus, the fluid will cavitate here first.

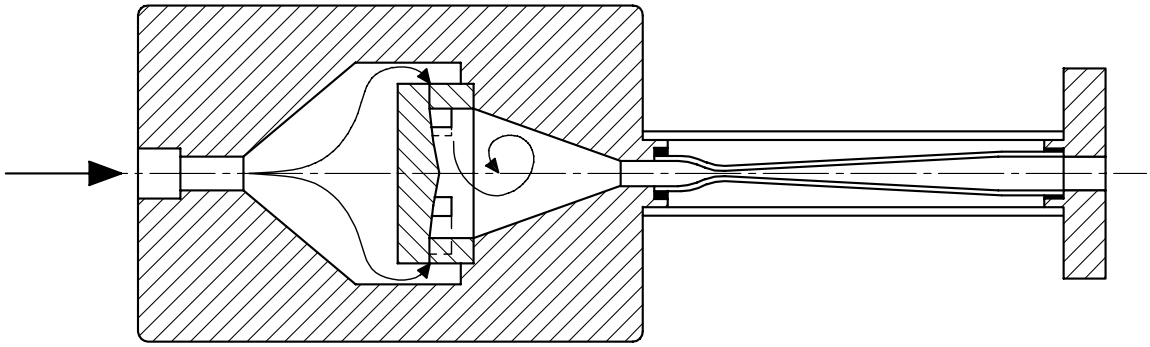

Figure 4.3.9: Sketch of the vortex chamber after Keller [1984]

In order to find the ideal vortex chamber configuration, six inflow forms were built and tested. After the originally circular one-sided inflow into the vortex chamber, rectangular tangetial inflow forms with various cross sections were examined in order to find the optimal relation between the pressure decline of the vortex flow and the pressure decline from the nozzle flow. The test results were such that a symmetrical, tangential inflow from four sides with a parallel inflow area seems best suitable. The relation between the tangential and parallel inflow area was varied in such a way that the pressure decline within the nozzle is composed of 2/3 of vortex flow and 1/3 of parallel flow. This configuration worked optimally.

Figure 4.3.10 (Keller [1982], final report VDMA) shows the tensile strains for water against the temperature, gas saturation pressure and system pressure as measured in a special test rig. (wind tunnel). The tensile strength values maximize for all saturation values and system pressures at a water temperature of 10°C, analog to Brigg's measurements [1950] (see chapter 4.2.4).

Tensile strength experiments with iso-butyl-alcohol (Butanol) produced maximum values of 16 bar and up to 5 bar with silicon oil. To measure the tensile strength of water in a cavitation tunnel, the device is installed directly at the downstream end of the tunnel's test range, just before the test body. Within the test range, the water sample is pulled through the vortex chamber and then returned into the tunnel by means of a pump. A computer-controlled step motor opens a ball valve behind the vortex chamber at a given, constant speed. So, the flow rate through the vortex chamber is gradually increased until cavitation starts in the nozzle. An acoustic and optical measuring device detects the moment of cavitation inception and triggers the computer's processor. With the help of measurement software, the pressure inside the vortex chamber and the volume flow through the eddy nozzle is determined. By means of these measured values, the tensile strength of the fluid can be determined by:

$$p_{ts} = p_V(\vartheta) - p_W = p_V(\vartheta) - p_E + K \cdot \dot{V}^2 \qquad (4.3.4)$$

with:

p_{ts} - tensile strength of the fluid

$p_V(\vartheta)$ - vapor pressure dependent on temperature

p_W - pressure in the vortex center ; p_E - pressure before entering the eddy nozzle

$\dot{V}$ - volume flow through the eddy nozzle

K - calibration factor

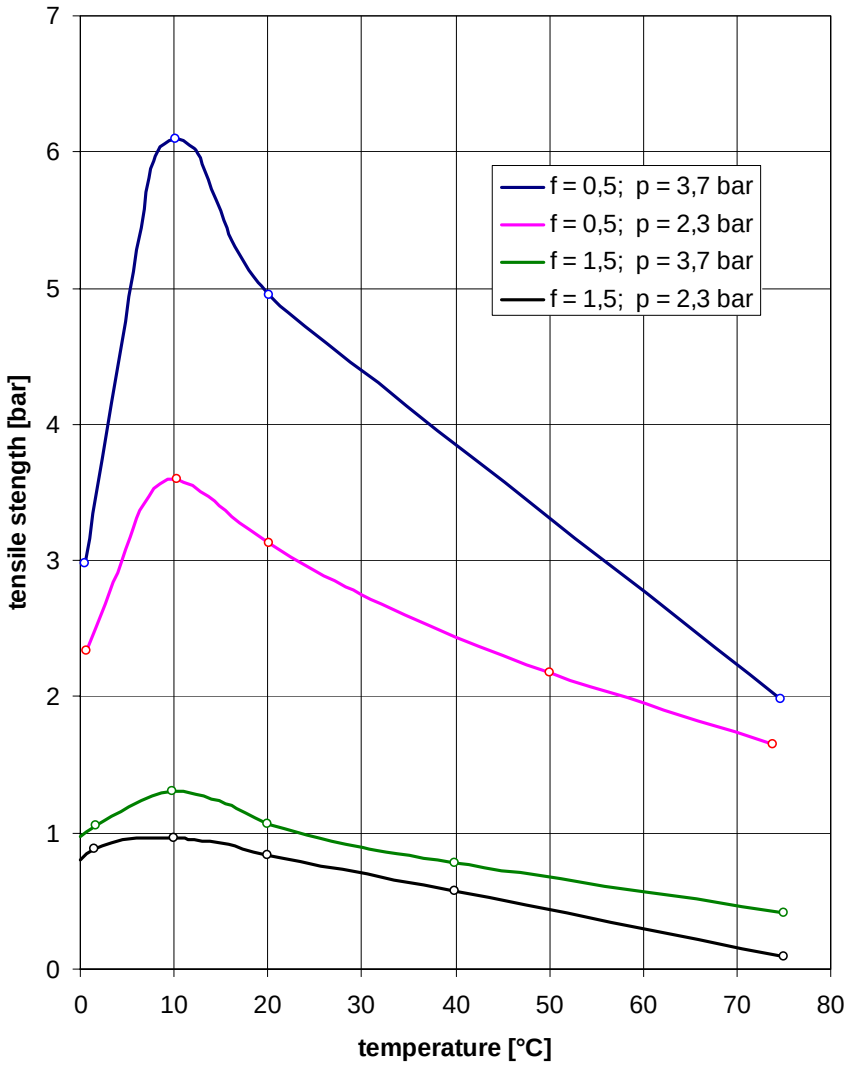

Figure 4.3.10: Tensile strength curve for water after Keller [1982]

The constant K was determined from a calibration with tensile strength-free water, which was produced with a defined injection of micro-bubbles. The calibration founds on the assumption that in a fluid free from tensile strength, cavitation inception in the eddy nozzle occurs at the steam pressure that is associated with the respective temperature.

The tensile strength measurements in the cavitation tunnel were conducted in a physically reasonable sequence. First, the temperature and the total gas content of the test water were set and measured. Then the tunnel was pressurized at a system pressure between 0.5 and 2 bar and the water was circulated in the tunnel for 30 minutes in order to stabilize the nucleus spectrum and thus, the tensile strength of the water. Afterwards, 40 tensile strength measurements each time were conducted to obtain a representative mean value. Since the nuclei of various sizes are statistically distributed, tensile strength is not an evenly distributed property either. As the individually measured tensile strength limit is a function of the nucleus that has just passed through the vortex chamber, a functional relation exists between the valve's opening speed and the measured mean tensile strength.

If the valve is opened very slowly, relatively much water will flow through the nozzle in each velocity range. Thus, there is a relatively high probability that a nucleus critical for this volume flow enters the nozzle. This leads to low tensile strength mean values. On the other hand, if the valve is opened quickly, there will be a greater probability that stronger volume flows through the nozzle can be reached without cavitation inception. This will lead to higher tensile strength values.

According to the respective total gas content, system pressure and the history of the water, the measured tensile strains ranged between $p_{ts} = 0$ and $p_{ts} \cong 2\ \text{bar}$. Tensile strains $p_{ts} = 0$ were mostly measured in gas-saturated, moved water. The highest tensile strains in the cavitation tunnel were obtained in calmed, degassed water (about 0.5 vol % total gas content).

4.3.7 Swirl Nozzle by Heller

Based on the method introduced by Keller [1983] for determining the tensile strength of fluids directly (see chapter 4.3.6), Heller [2000 – 2004] developed a fully automated system to determine tensile strength of water in cavitation tunnels. The focus lay on the construction of a swirl nozzle according to fluid mechanical aspects such as generation of vortex, velocity and pressure gradients against the nozzle's cross section, velocity and pressure progression parallel to the axis, and flow detachment in the diffuser as well as vortex-free flow-off.

For the determination of the tensile strength of water, the swirl nozzle shown in figure 4.3.11 was used. Due to the tangential tube inflow into the swirl nozzle, a swirl flow is generated whose lowest pressure is reached in the flow center during the flow through the narrowest cross-section. Therefore, cavitation occurring in the flow center will be nearly free from interface influences.

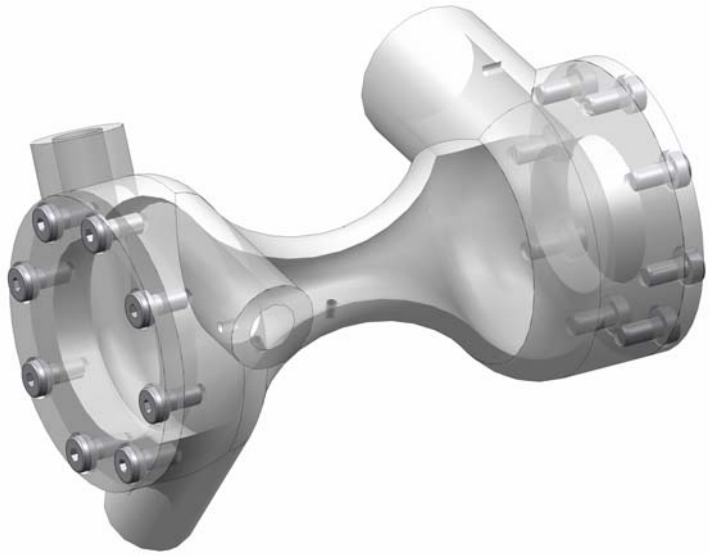

Figure 4.3.11: Swirl nozzle

Contrarily to the minimal pressure in the flow center, pressure measurement is possible at any point of the nozzle contour.

Employing the numerical solution for the dimensionless coefficient k_p, which specifies the ratio of the pressure difference between the wall and the flow center at the narrowest nozzle cross section Δp_{nozzle} and the pressure difference at the wall between nozzle entry and the narrowest nozzle cross section Δp_{wall}, the minimum pressure p_{min} can be determined by:

$$p_{min} = p_{wall} - k_p \cdot \Delta p_{wall} = p_{crit}\,; \tag{4.3.5}$$

with:

$$k_p = \frac{\Delta p_{nozzle}}{\Delta p_{wall}}\,; \tag{4.3.6}$$

$$\Delta p_{nozzle} = p_{wall} - p_{min}; \tag{4.3.7}$$

$$\Delta p_{wall} = p_{inlet} - p_{wall}; \tag{4.3.8}$$

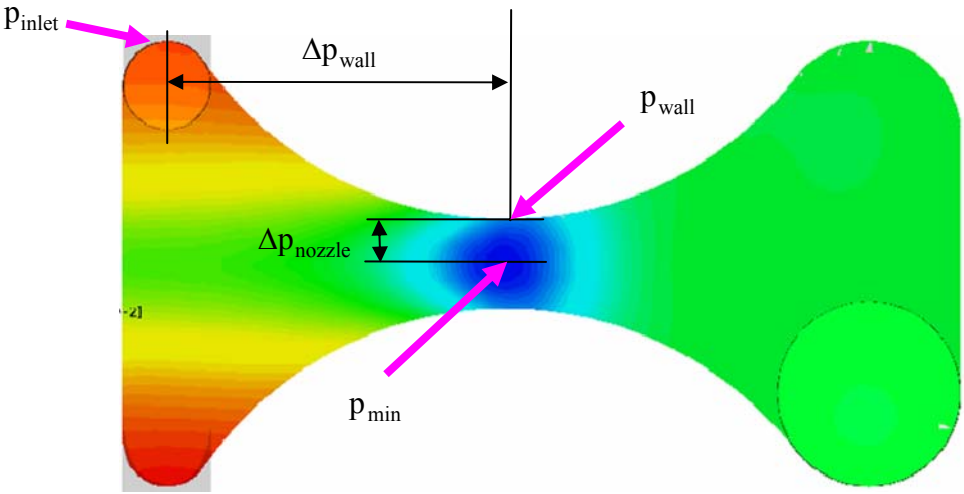

Figure **4.3.12:** Determination of the minimum pressure in the swirl nozzle

The difference of the vapor pressure p_V that is correlated to the measured temperature is specified by the current tensile strength p_{ts} of the water.

$$p_{ts} = p_V - p_{crit}. \tag{4.3.9}$$

A new swirl nozzle for experimental research (see fig. 4.3.13) had to be manufactured for various reasons (strength, vibrations, sealing problems). This swirl nozzle was made off Perspex (synthetic material) and installed into a bypass line of the cavitation tunnel (see chpt. 5.3 and fig. 5.3.2). This necessary pressure difference for the flow through the nozzle was realized by a pump. It is equipped with revolution control and is placed at the suction end of the swirl nozzle. Thus, mass flow through the bypass line is continuously adjustable.

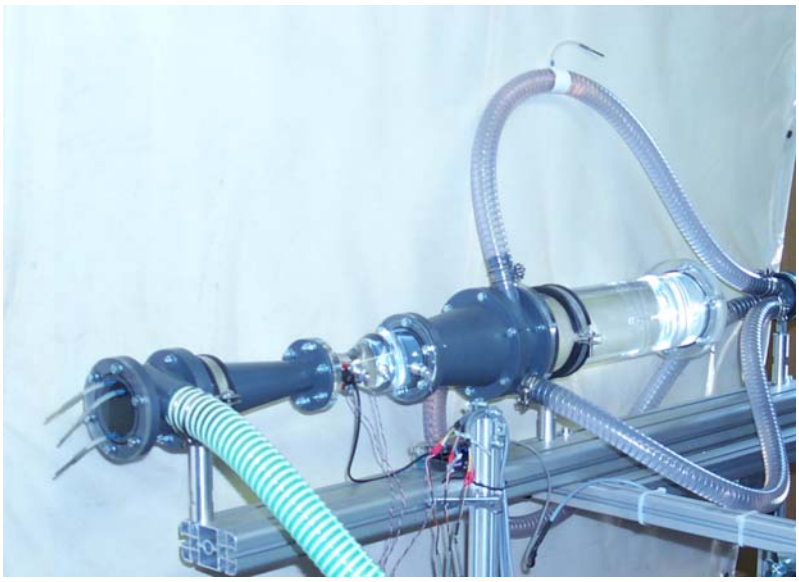

Figure 4.3.13: Swirl nozzle by Heller [2003]

For the pressure measurements, miniature pressure transducers were attached at the respective points of the swirl nozzle. A microphone was installed into the wall of the nozzle in order to detect cavitation inception. The voltage signals of the transducers and the microphone were recorded and processed by a computer. Taking the tensile strength measurements of the water is relatively simple. By means of the bypass pump, flow is increased until the microphone registers the typical sound intensity at cavitation inception. With the pressures measured at that moment, the equations mentioned above are evaluated.

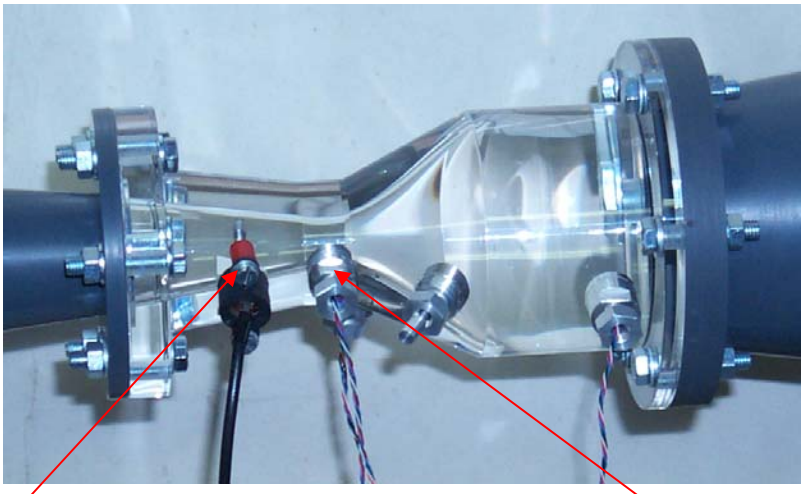

Figure 4.3.14: Swirl nozzle with microphone and pressure transducers

In order to be able to calculate the tensile strength from the measured data with equation (4.3.9), the coefficient $k_p(\Delta p_{wall})$ was determined by means of numerical flow simulation (Kempe [2005]). Flow through the swirl nozzle is characterized by strong curvature of streamlines as well as high velocity and pressure gradients. High demands were made on the flow computations in order to meet the requirement that the flow variables were not only to be provided qualitatively but also quantitatively.

Since the transport equations for the Reynolds stress tensor are not directly solvable, simplifying assumptions had to be made about the complex mechanism of the turbulences. This is why the solution of any flow problem using turbulence models must be an approximate solution. The swirl nozzle has a contraction ratio of 40:1. Due to this contraction, the anisotropy of the Reynolds stress tensor is heavily changed. That is why particular attention was paid to the modeling of the pressure-sheer correlation when selecting a suitable Reynolds stress model. According to a study by Grunert [2000] the SSG-RSM (SSG - model by Speziale, Sakar and Gatski – RSM – Reynolds Stress Model) produces best results for a flow simulation in a swirl nozzle. Furthermore, for comparison, a wide structure simulation (LES – Large-Eddy-Simulation) with the Smagorinski fine structure model (SGS-model) at the same mesh resolution was conducted.

The simulation computations, however, were not carried out for the swirl nozzle flowed through by water (fig. 4.3.14) but for a model nozzle flowed through by air (fig. 4.3.15) in order to verify the numerically obtained data (because of the inaccuracies mentioned above) and to gain best certainty of the results. The Reynolds numbers (in relation to the diameter at the narrowest cross section of the nozzle) are of the order Re ≈ 60.000. The employed calculation mesh had circa $8 \cdot 10^6$ elements with $1.7 \cdot 10^6$ grid points. Calculations were taken over by 5 LINUX-PCs with a clock frequency of 2.5GHz and 2 GB RAM each. Computing time was 120 h per point (see fig. 4.3.17).

Figure 4.3.15: Plastic model of the swirl nozzle (scale 6:1)

The model swirl nozzle shown in figure 4.3.15 was built on a scale of 6:1 and connected to a revolution-controlled electric fan. With the help of this installation the model nozzle could be examined at the same Reynolds number as the original nozzle. For experimental determination of pressure and velocity distributions over a cross section of the model nozzle, pressure and hot-wire probes were installed. Employing the model measurements in the air-flow nozzle, the proportional factor $k_p(\Delta p_{wall})$ dependent on wall pressure and the Reynolds number were ascertained experimentally. The dependency of the factor $k_p(\Delta p_{wall})$ follows well a power function (see fig. 4.3.16) that depends on the nozzle contour.

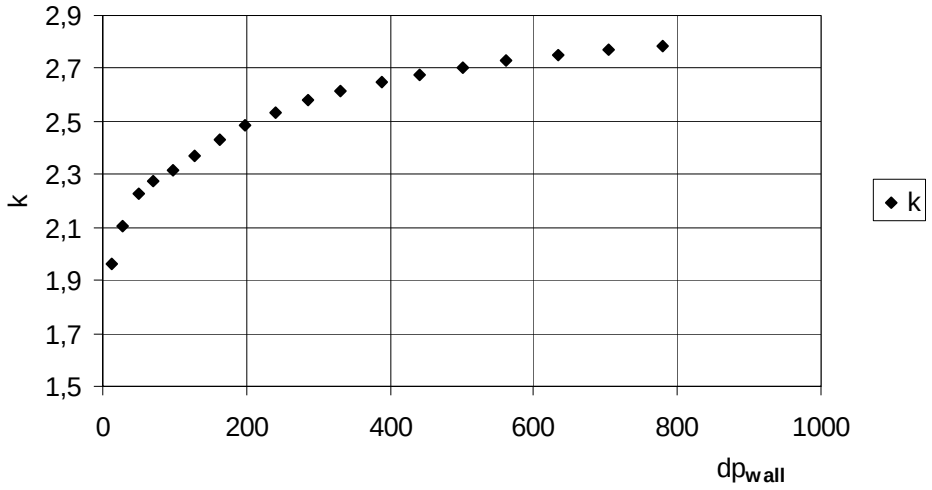

Figure 4.3.16: Dependence of the factor k_p on the wall pressure difference dp_{Wand}

$$k_{Luft} = a \cdot (\Delta p_{Wand})^n \tag{4.3.10}$$

$$K = \frac{\rho_{Wasser}}{\rho_{Luft}} \cdot \left(\frac{\upsilon_{Wasser}}{\upsilon_{Luft}} \right)^2 \cdot \left(\frac{D_{Luft}}{D_{Wasser}} \right)^2 \tag{4.3.11}$$

Due to the equal Reynolds numbers, this function could be transferred to the water-operated original nozzle by means of equations (4.3.10) and (4.3.11).

$$k_{Wasser} = a \cdot \left(\frac{\Delta p_{Wand}}{K} \right)^n \tag{4.3.12}$$

Figure 4.3.17 shows the experimentally determined k_p-values by Heller [2003] and the numerically ascertained values by Kempe [2005].

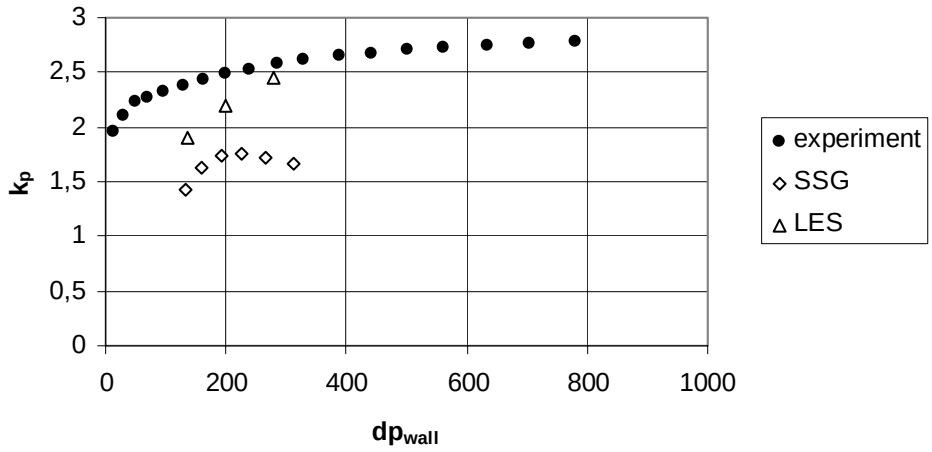

Figure 4.3.17: Comparison between the experimentally determined kp-values by Heller [2003] and the respective computed values by Keller[2005]

The experimental values cannot be reproduced with the SSG-Reynolds stress model. Though the field variables can qualitatively be determined well with the SSG-RSM, the computed pressure in the center of the flow, however, differs from the experimentally obtained value. As mentioned before, for statistic turbulence modeling, simplified model transport equations for the components of the Reynolds stress tensor have to be solved. Even with a refined mesh up to the resolution of the scales in the dissipation range, model transport equations cannot represent the exact solution of the flow field. Employing LES with the Smagorinski fine structure model (only computed for one point), the experimental result can be reproduced much better.

In order to measure and thus, to compare the critical pressure pkrit with the calculated pressure at cavitation inception inside the swirl nozzle, the profile shown in figure 4.3.18 was installed in the test track of the cavitation tunnel. Here, the assumption is made that the critical pressure is independent from the flow, i.e. only dependent on the fluid. The profile consists of two components, one rotary, cylindrical front part and a solid base of constant thickness. A miniature pressure sensor attached to the cylindrical surface is brought to the place of cavitation inception by means of a step motor, consequently measuring the critical pressure directly.

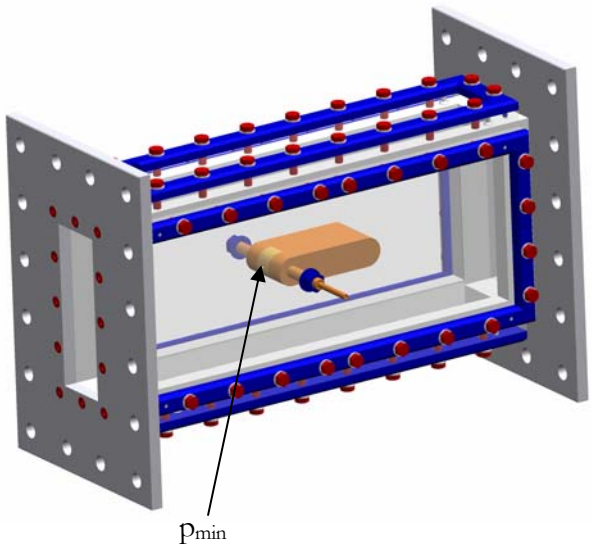

Figure 4.3.18: Determination of the minimal of a profile in the cavitation tunnel

Figure 4.3.19 shows the pressure distributions over the cylindrical front part between 0° and 90° (= 100 gon) at various approach velocities. The orientation of the pressure sensor inside the cylinder against the flow was defined as 0°. At constant approach velocities each time the cylinder was turned clockwise at a step angle of 4.5° and the wall pressures were measured. The minimal pressure was determined with -0.12 bar (last measurement before cavitation inception), matching the minimal pressure that was detected inside the eddy nozzle at the same time.

The results of extensive tests with the swirl nozzle construction described above, however, sometimes exhibited significant fluctuations at constant flow rates. The reasons are wild pressure fluctuations due to the inflow situation through the three tangentially positioned tubes into the swirl nozzle.

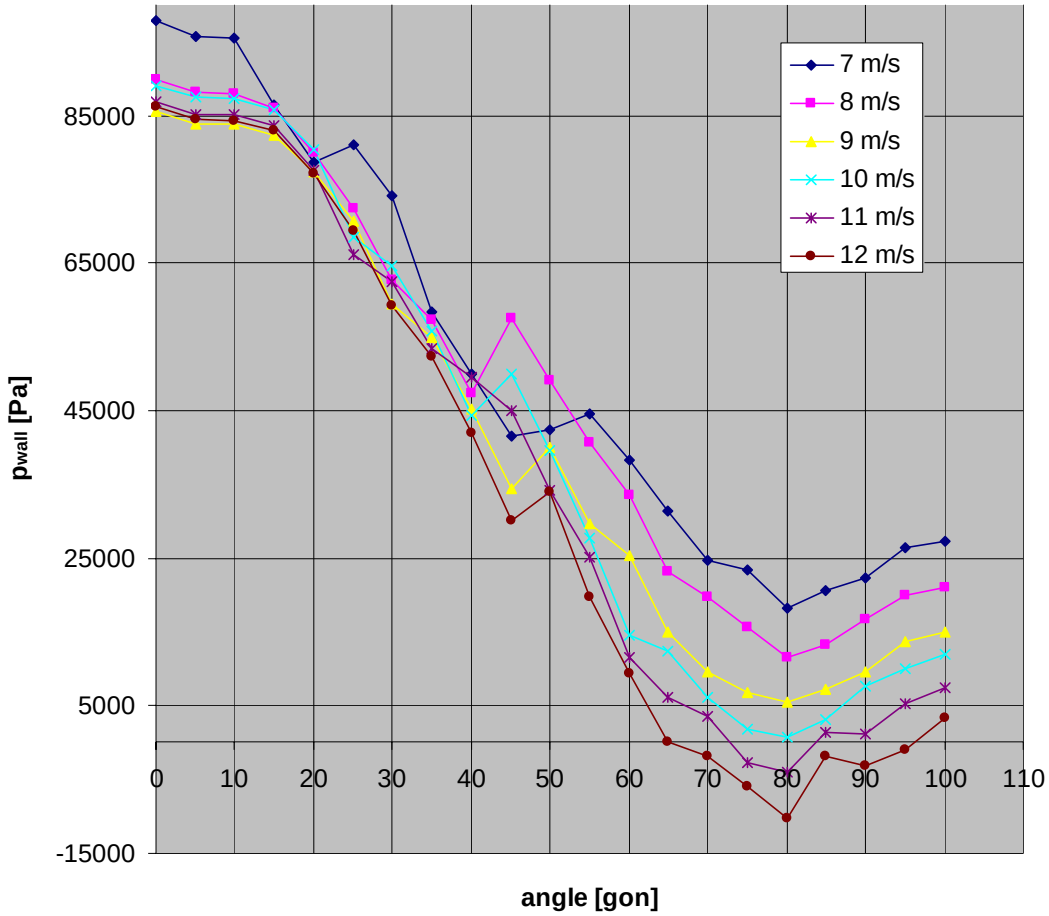

Figure 4.3.19: Pressure distribution across the cylindrical front surface at various approach velocities

However, a fundamental difficulty lies in the fact that by creating such vortex flows, a vortex tube along the nozzle axis of almost constant inner pressure will be generated. It follows that a gas bubble entering this area will greatly expand and consequently fill the whole center of the vortex tube. Because of the statistical size distribution of gas bubbles in water, this process can occur over a wide pressure spectrum without vaporization occurring.

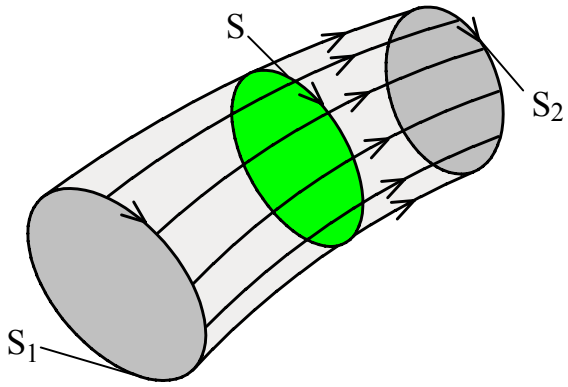

Figure 4.3.20: Vortex tube

For a vortex tube

$$\Gamma = \oint_S \underline{u} \cdot d\underline{s} \tag{4.3.13}$$

denominates its intensity, where S is a curve enclosing the vortex tube. After the third Helmholtz Vortex Law, for any two such curves S_1 and S_2 it is:

$$\Gamma_1 = \oint_{S_1} \underline{u} \cdot d\underline{s} = \Gamma_2 = \oint_{S_2} \underline{u} \cdot d\underline{s} \,. \tag{4.3.14}$$

This means that a vortex tube with non-vanishing intensity Γ cannot end inside a flow area. It must either end at a wall or form a ring. In the swirl nozzle mentioned above, the case walls ensure the stable existence of the vortex tube.

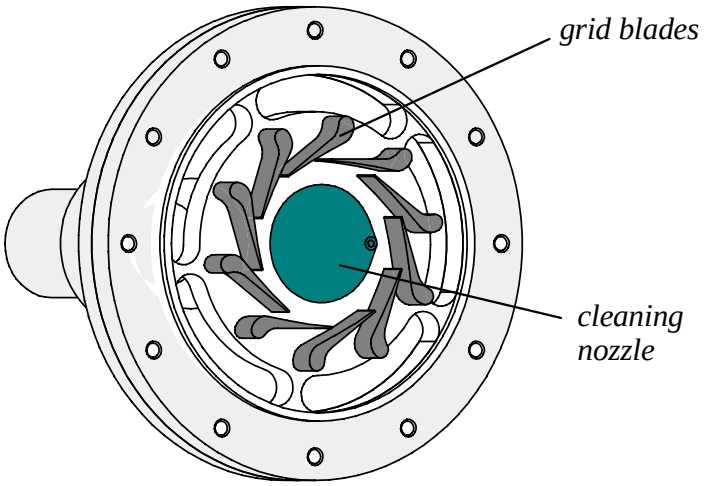

Bild 4.3.21: Set of blades with cleaning nozzle

Finally, problems with the sensitive miniature pressure transducers were difficult to master. In addition to the relatively complicated measurement technology and its necessary calibration, leakages were rather common at the sensors' installation points in the nozzle. These problems were to be remedied with the subsequently described, improved construction. To even out pressure fluctuations of the inflow into the swirl nozzle, a set of blades are used to control the swirl angle, as shown in figure 4.3.21. The so-called cleaning nozzle prevents both the generation of a stable gaseous vortex tube and the adhesion of gas bubbles at the inner case walls.

In order to prevent interferences with the pressure transducers used so far, the minimal pressure inside the swirl nozzle was measured against the volume flow. This functional relation was implemented into the measuring software. The pressure in the vortex center and at the narrowest cross section of the nozzle, based on the flow path theory of stationary and friction-free flow, was calculated for a swirl angle of α=35° as follows:

$$p(r) = p_{ges} - \frac{\rho}{2} \cdot u(r)^2 \tag{4.3.15}$$

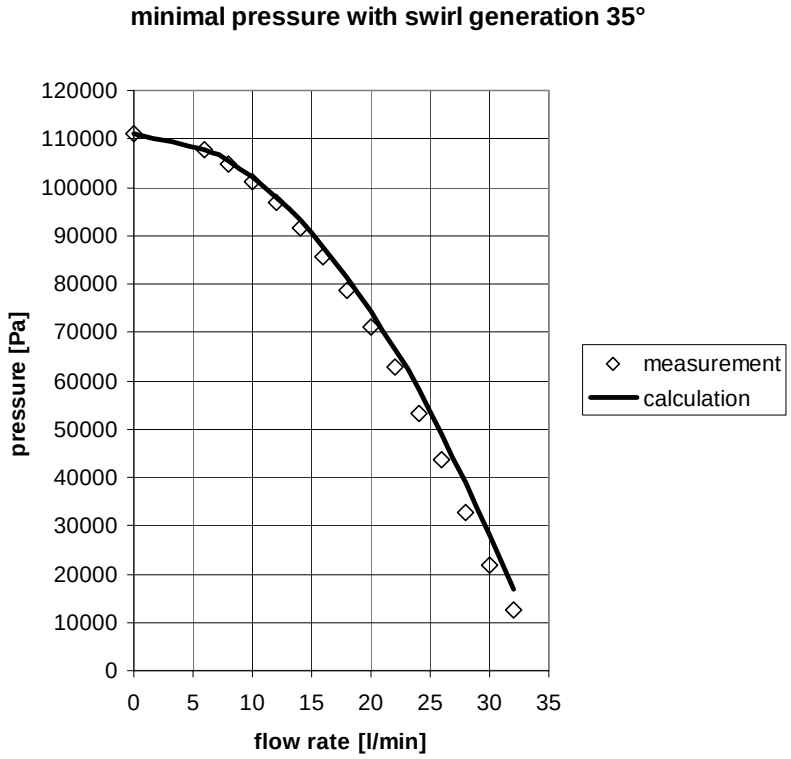

Figure 4.3.22: Comparison of measurement and calculation of the minimal pressure inside the swirl nozzle

with:

$$u(r) = \sqrt{u_m^2(r) + u_u^2(r)} \tag{4.3.16}$$

$$u_m(r) = \frac{\dot{V}}{A} \tag{4.3.17}$$

$$u_u(r) = \frac{u_m(r)}{\tan\alpha} \tag{4.3.18}$$

where:

$$\begin{aligned} u_m \cdot r &= \text{const.} \\ u_u \cdot r &= \text{const.} \end{aligned} \tag{4.3.19}$$

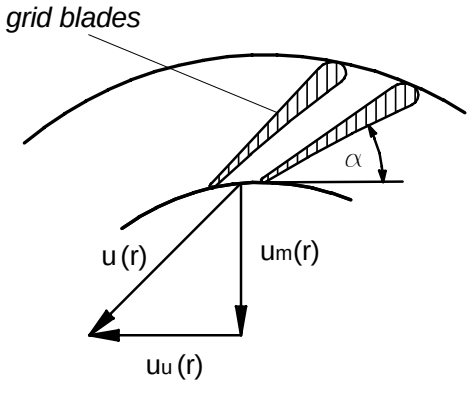

Figure 4.3.23: Swirl generation

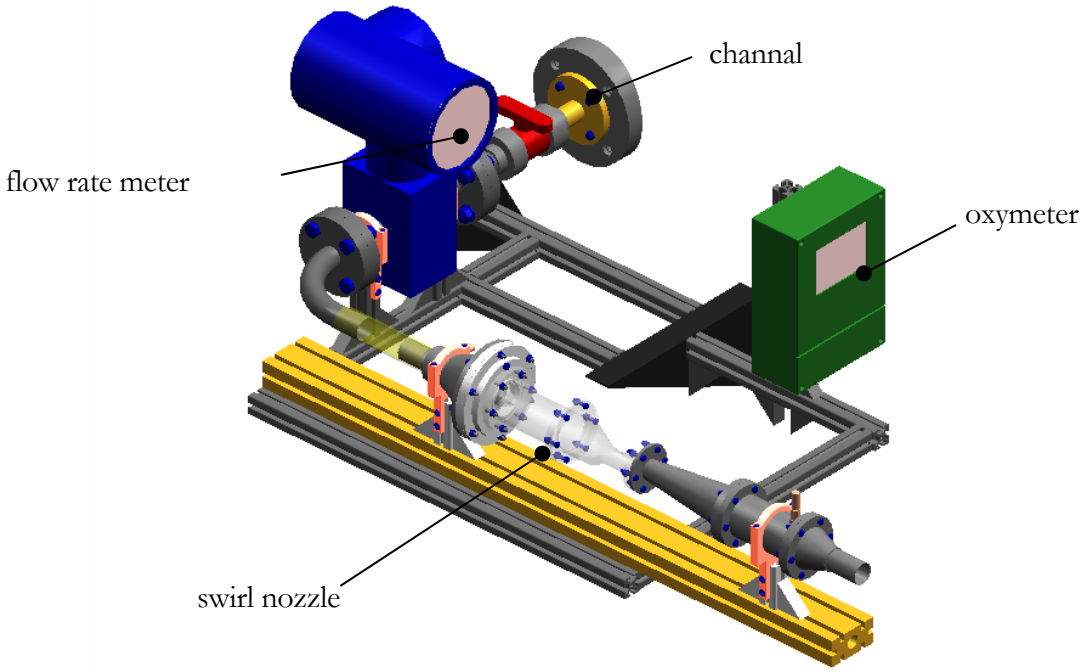

Figure 4.3.24: Tensile strength measurement facility

So, a measuring instrument has been made available for determining the tensile strength of water in tunnels, which works independent from the tunnel type and fully automated. Measurements in various tunnels and test rigs produced reproducible tensile strains in the range of $p_{ts} = 0 \ldots 1{,}3 \text{ bar}$.

5 Hydrodynamic Effects and Water Quality

5.1 Sound Velocity in Gas-Containing Water

The influence of gas-containing water on the local sound velocity is significant. Employing the theory of equilibrium flow, ISAY (1989) gives the following equation (5.1.1) for the local sound velocity a:

$$a = (1+\alpha)\sqrt{\frac{p - p_v + \frac{4S}{3R}}{\rho_W \cdot \alpha}} \tag{5.1.1}$$

with the local relation of gas content and water volume,

$$\alpha = \frac{V_G}{V_W} \tag{5.1.2}$$

the surface tension σ and the bubble radius R.
Using the quasi-stationary stability theory, the critical bubble radius is obtained by the relation:

$$p_v - p_{crit} = \frac{4S}{3R_{crit}} \tag{5.1.3}$$

Thus, the sound velocity in equation (5.1.1) vanishes for the critical bubble state, which demonstrates the validity limit of the theory of equilibrium flow. In order to elude these difficulties, ISAY (1989) derives the equation (5.1.4):

$$a = (1+\alpha)\sqrt{\frac{p}{\rho_W \cdot \alpha \cdot (1+\Lambda)}} \tag{5.1.4}$$

with the pressure p, the density of water ϱ_W and an empirical coefficient Λ. With both equation (5.1.1) and equation (5.1.4), determination of the sound velocity in pure water ($\alpha \rightarrow 0$) is impossible, because in the derivatives water is assumed incompressible. The following equation (5.1.5) is presented for the calculation of the local sound velocity taking into acount the compressibility of water:

$$a = (1+\alpha)\cdot\left(\frac{\rho_W \cdot \alpha}{\kappa(p - p_v) + \frac{2S}{R}\left(\kappa - \frac{1}{3}\right)} + \frac{1}{a_W^2}\right)^{-\frac{1}{2}} \tag{5.1.5}$$

which is also valid for the special case $\alpha \rightarrow 0$ for pure water. Figure 5.1.1 shows the sound velocity a_W in pure water against the temperature. For comparison, values for air have also been added.

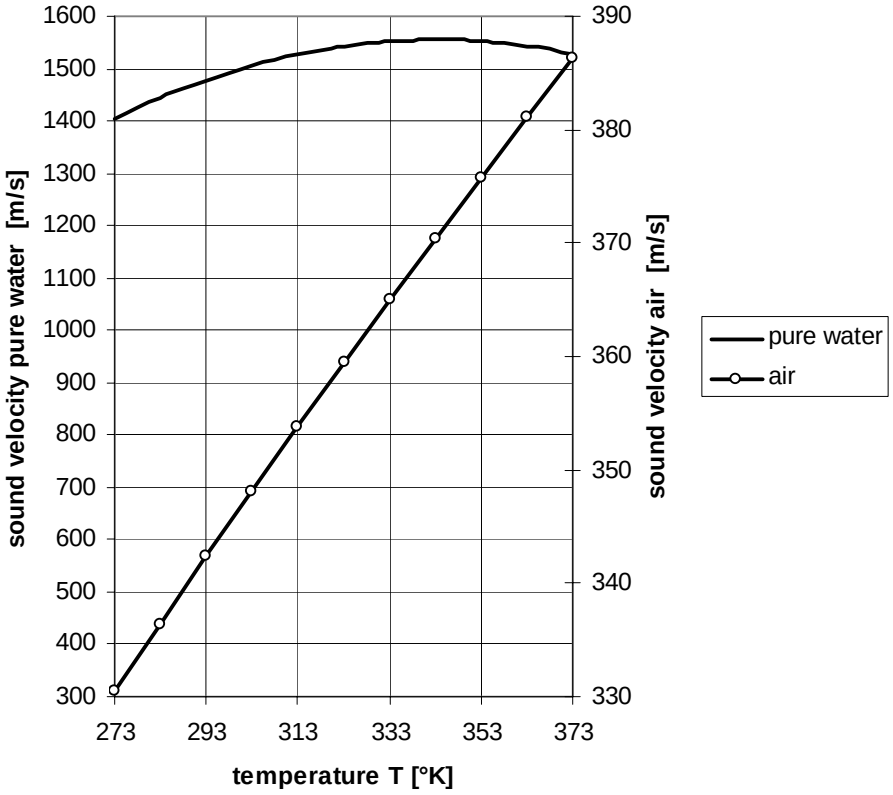

Figure 5.1.1: Sound velocities against the temperature after Isay [1989]

On the other hand, calculations with equations (5.1.1) and (5.1.4) show that the sound velocity in gas-containing water in thermo-dynamic balance can reach very low values and it can fall far below the values valid for air. Figure 5.1.2 shows the sound velocity in gas-containing water against the pressure p. As a reference value p_0 = 1 bar was assumed. The propagation of planar sound waves in bubble-containing fluids was examined by Wijngaarden [1972, 1979]. Employing the one-dimensional principle of linear momentum as well as the continiuty equation, the sound velocity, as phase velocity dependent on the mean void fraction α_0 in equation (5.1.6), is derived to:

$$a = \frac{1+\alpha_0}{\sqrt{\rho_W \alpha_0}} \sqrt{p_{L_0}\left(1-\frac{\Omega^2}{\omega_0^2}\right)} \tag{5.1.6}$$

with: $$\omega_0 = \frac{1}{R_0}\sqrt{\frac{3p_{L_0}}{\rho_W}} \tag{5.1.7}$$

as the mean bubble eigenfrequency and Ω as the impressed angular frequency. Further attenuation of sound propagation is caused by viscosity and heat transfer effects between fluid and bubbles. An expansion of the theory for various velocities of bubbles and fluids can be found in Tan & Bankoff [1984], Biesheuvel & van Wijngaarden [1984] and Agostino, Brennen & Acosta [1988]. A work about the propagation of non-linear waves in a fluid containing vapor bubbles was published by Nakoryakov, Pokusaev, Shreiben & Pribaturin [1988].

$a_W = 1450\ m/s$ $p_0 = 1{,}0\ bar$ $p_V = 0{,}020\ bar$	1) $\alpha_0 = 10^{-4};\quad \Lambda = 0$ 2) $\alpha_0 = 10^{-3};\quad \Lambda = 0$ 3) $\alpha_0 = 10^{-4};\quad \Lambda = 1$ 4) $\alpha_0 = 10^{-3};\quad \Lambda = 1$	5) $\alpha_0 = 10^{-4};\quad R_0 = 10^{-3}\ cm$ 6) $\alpha_0 = 10^{-4};\quad R_0 = 5 \cdot 10^{-3}\ cm$

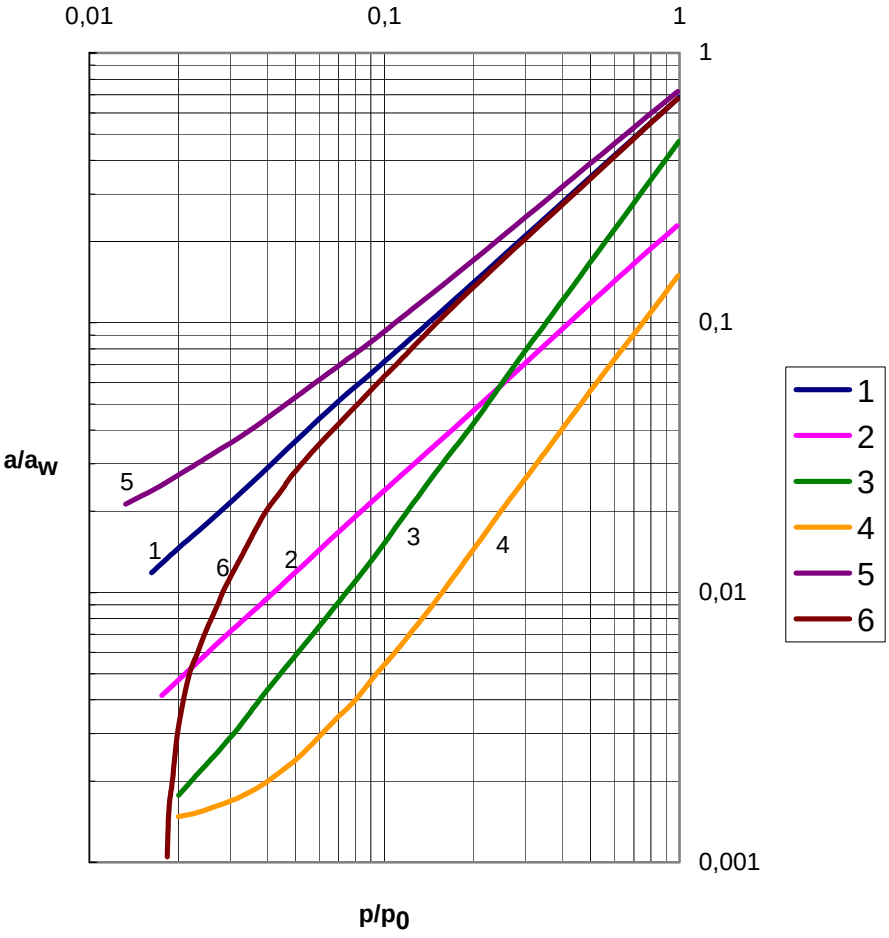

Figure 5.1.2: Characteristics of sound velocity in gas-containing water after Isay 1989]

Stoffel & Striedinger (2000) give an estimate of the sound velocity a_m in mixtures of water and water vapor:

$$\frac{1}{a_m} = \sqrt{\frac{(1-\alpha)^2}{a_{Fluid}^2} + \frac{\alpha^2}{a_{Gas}^2} + \frac{\alpha \cdot (1-\alpha) \cdot \rho_{Fluid}}{p}} \tag{5.1.8}$$

with: $$\alpha = \frac{V_{Gas}}{V_{Gas} + V_{Fluid}} \tag{5.1.9}$$

Figure 5.1.3 shows the sound velocity a_m against α.

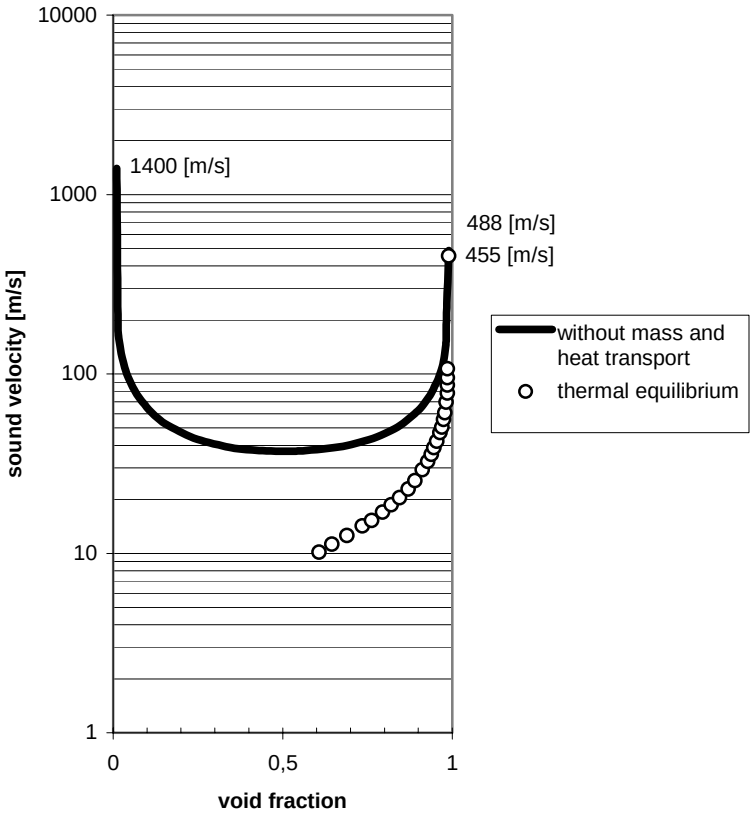

Figure 5.1.3: Sound velocity against the void fraction after Stoffel & Striedinger [2000]

Thus, the compressibility of gas-containing water is significant, so supersonic states in negative pressure areas of technical flows are likely to appear at high gas contents. Similar to transonic aerodynamics, pressure and shocks occur at the end of local supersonic areas (see Campbell. Pitcher [1958], Wieghardt [1967], Wijngaarden [1972, 1979] und Isay. Roestel [1974, 1975]). Employing the conventional quasi-stationary shock equations as well as the laws of conservation of mass, momentum and energy, the following constitutive equations dependent on the void fraction α can be derived:

$$\frac{\hat{\rho}}{\rho} = \frac{u}{\hat{u}} = \frac{1+\alpha}{1+\hat{\alpha}} \tag{5.1.10}$$

$$\hat{p} - p = \rho \cdot u\left(u - \hat{u}\right) = \rho_W \cdot u^2 \frac{\alpha}{\left(1+\alpha\right)^2}\left(1 - \frac{\hat{\alpha}}{\alpha}\right) \tag{5.1.11}$$

$$\frac{\hat{T} - T}{T} = \frac{R_L\, \eta_{L_0}\, \alpha}{2\, \varepsilon_W\, \alpha_0} \cdot \frac{\hat{p} + p}{p_0 - p_v + \dfrac{2S}{R_0}} \tag{5.1.12}$$

The state variables after the shock are marked with "^". Further designations:

$u, \hat{u}$ normal component of the velocity relative to the shock area

η_{L_0} air-mass ratio m_L / m_W at the initial state of the inflow

ε_W specific heat of the water; R_L gas constant

S surface tension

Estimates with equation (5.1.12) show that the temperature increase during the shock in gas-containing water remains neglectably small, contrasting the significant temperature leaps known in aerodynamics. Figure 5.1.4 shows a military aircraft with a condensation cloud in the expansion area during flight at transonic speed. The cloud ends abruptly at the shock due to the temperature leap.

Figure5.1.4: Condensation cloud in transonic flight (image source: http://aero.ilr.tu-berlin.de)

5.2 Gas Content of Water and Pressure Distribution at Profiles

In Isay & Roestel [1974, 1975] and Isay [1989] there are comprehensive publications on the influence of the gas content in water and the pressure distribution in the surrounding of profiles. Plane and steric, stationary and instationary, compressible flows of gas-containing water around airfoils are discussed. The eigenmotion of the gas bubbles is neglected and a uniform pressure and velocity field is assumed. It is shown that pressure distributions dependent on the water's gas content are significantly different from the incompressible state of flow if, due to the low local sound velocities, local supersonic areas limited by compression impulses occur.

Figure 5.2.2 shows calculations of pressure distributions for a curved profile in stationary flow with an approach angle $\delta_0 = 0$. A curved profile at $\delta_0 = 0.025$ is shown in Figure 5.2.3. The values are given for the drag side at $y = 0$ and a greater distance y/A (see fig. 5.2.1). The incompressible pressure distribution is depicted as a dashed line. Figure 5.2.3 clearly shows how the expansion of the supersonic area is increasing at growing void fraction α_0 and how the shock is moving downstream. The supersonic areas for the curved profile at no approach angle (fig. 5.2.2) are more expanded than for a curved profile at some approach angle. Beyond the shock, post-expansion occurs, as known from gas-dynamic flows. The results show clearly that significant differences between the compressible and incompressible pressure field only result from the influence of the shock and are therefore restricted to its surrounding.

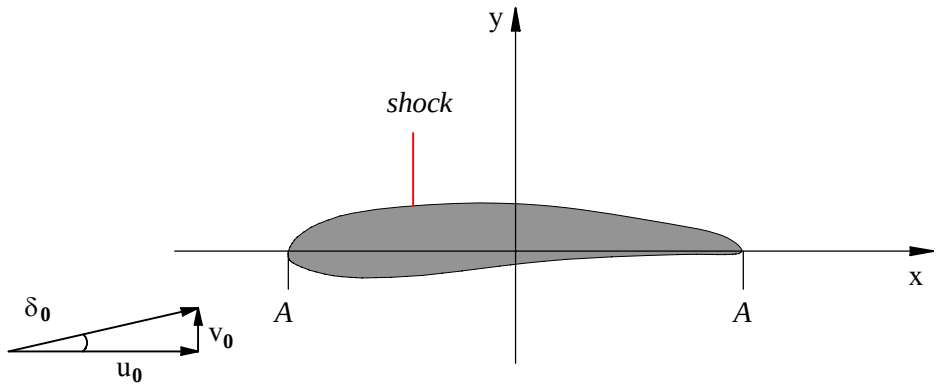

Figure 5.2.1: Designations and coordinates at the profile

——— compressible

– – – – – – incompressible

10	$\alpha_0 = 10^{-4}$;	$y/A = 0$;	$p_0 = 1{,}0$ bar
11	$\alpha_0 = 10^{-4}$;	$y/A = 0{,}07$;	$p_0 = 1{,}0$ bar
20	$\alpha_0 = 10^{-4}$;	$y/A = 0$;	$p_0 = 0{,}5$ bar
21	$\alpha_0 = 10^{-4}$;	$y/A = 0{,}05$;	$p_0 = 0{,}5$ bar
30	$\alpha_0 = 4 \cdot 10^{-4}$;	$y/A = 0$;	$p_0 = 0{,}5$ bar
31	$\alpha_0 = 4 \cdot 10^{-4}$;	$y/A = 0{,}09$;	$p_0 = 0{,}5$ bar

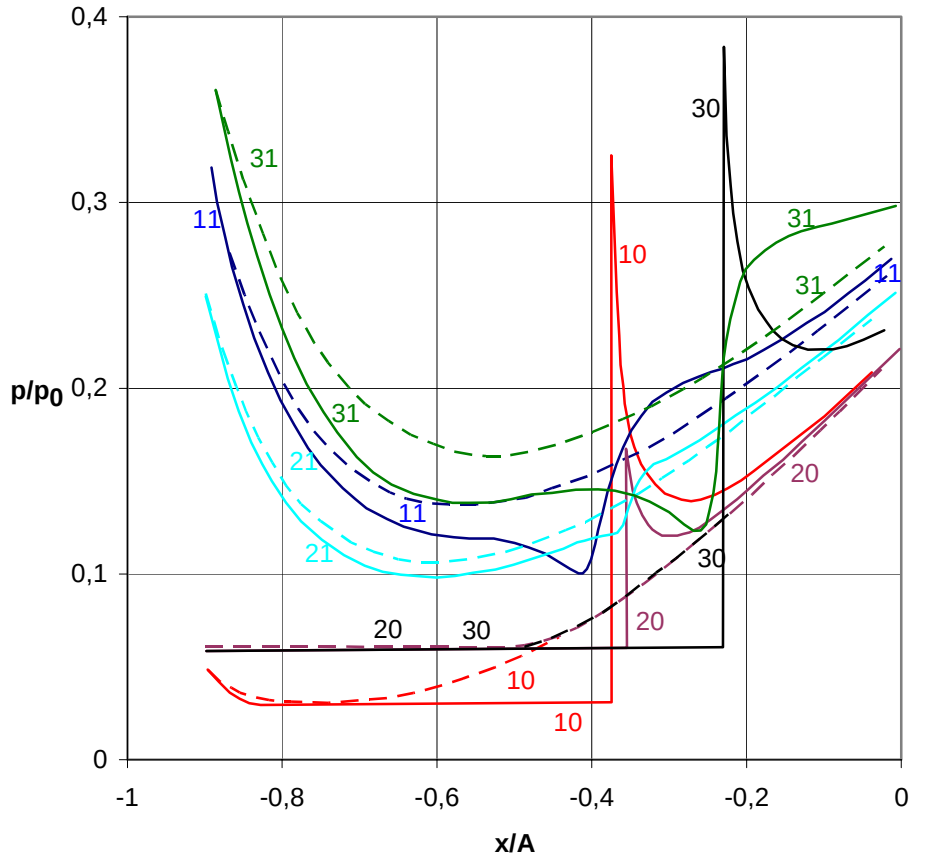

Figure 5.2.2: Computed pressure distribution at a curved profile in gas-containing water after Isay [1989]

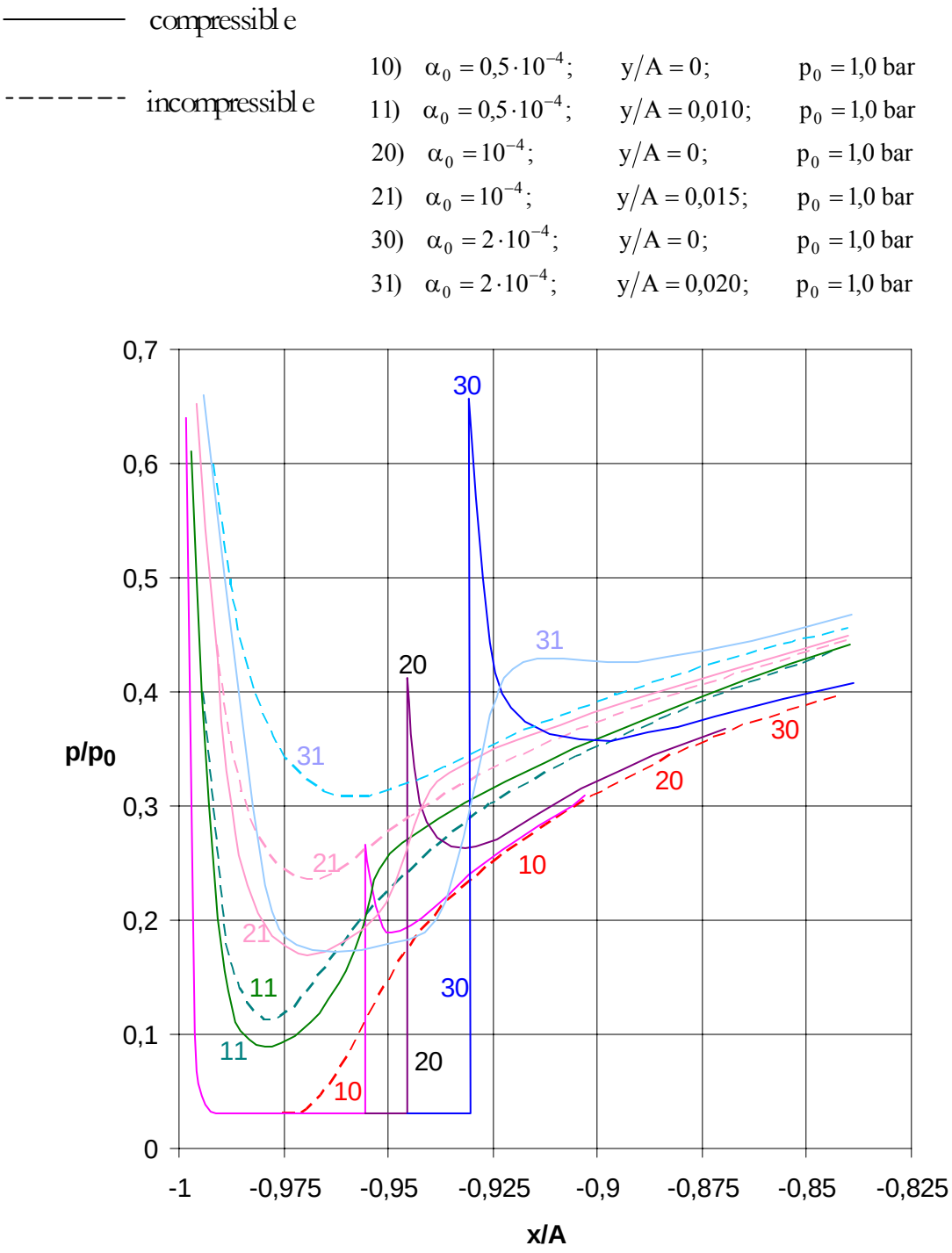

Figure 5.2.3: Computed pressure distribution at an uncurved profile in gas-containing water after Isay [1989]

5.3 Cavitation

5.3.1 Introduction

The phenomenon of cavitation (see chpt. 1.2) was first observed in 1894 when the English vessel Turbinia was equipped with fast-rotating steam turbines instead of the slowly rotating conventional piston steam engines. Apart from a loss of efficiency, already after a short time of operation, the propeller blades had suffered severe deterioration that could not be explained with corrosion or similar effects. Later other hydraulic engines such as pumps or water turbines exibited remarkably deep and extensive erosions that were regarded as a special form of electro-magnetic corrosion. However, since Lord Rayleigh (1842 – 1919) called attention to the high pressures that may occur at the implosions of vapor bubbles, cavitation erosion has been recognized as material destruction primarily caused by mechanical impact. (see chpt. 5.3.3)

If cavitation cannot be avoided by alterations or limitations of operation, undesirable effects can occur such as vibrations, severe noise, loss of efficiency and extensive material erosion as far as the complete destruction of the part being subject to flow. Particularly, areas with high flow velocities and the resulting low local pressures are affected, for example hydraulic engines, valves and pipelines, constructions of hydraulic engineering and elements of shipbuilding.

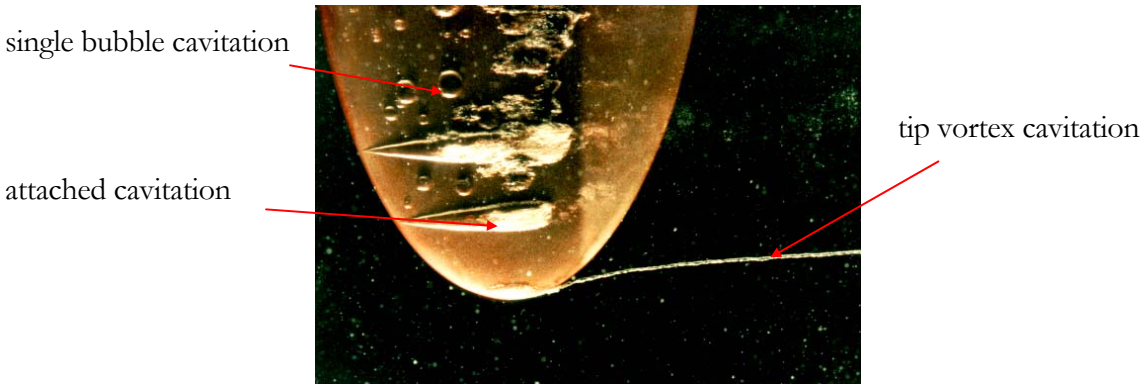

Figure 5.3.1: Cavitation at a three-dimensional profile with the cavitation types single bubble cavitation, attached cavitation and tip vortex cavitation by Keller [1984]

Properties of cavitation play an important role in designing and constructing hydraulic turbo engines, propellers and other hydraulic systems. Investigations to determine the various types of cavitation and their influences on characteristics or the efficiency of affected machinery are normally carried out at model machines or by means of special test facilities, so-called cavitation tunnels. Figure 5.3.2 shows the conventional configuration of a test facility schematically. However, installation size as well as construction characteristics of existing tunnels may vary considerably according to the purpose of their uses (pumps, turbines, etc.).

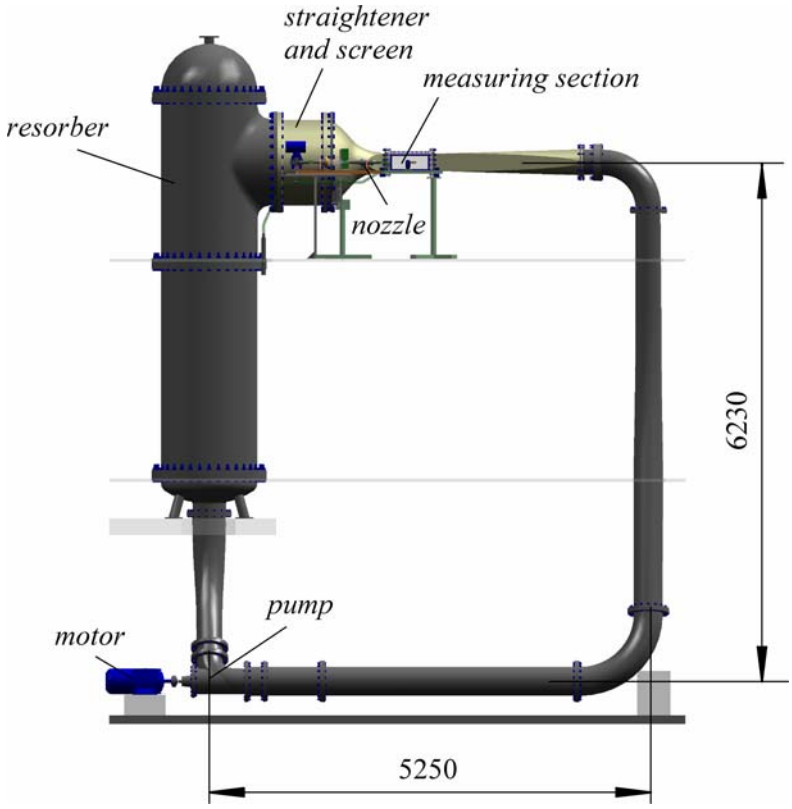

Figure 5.3.2: Principle sketch of a cavitation tunnel (TU Dresden)

Nuclei existing in water act as centers of cavitation processes. The pressure field is of particular importance for their behavior. Although the mean pressure of an interface adjacent to a body equals the pressure in the outer flow with good approximation, local and temporal pressure fluctuations within that interface may significantly influence cavitation inception. Such fluctuations occur in turbulent interface or shear layers. However, describing these turbulent processes in detail is very complicated. In a flow that is stationary by potential theory, pressure and velocity also fluctuate aperiodically around a mean value and can therefore only be ascertained stochastically.

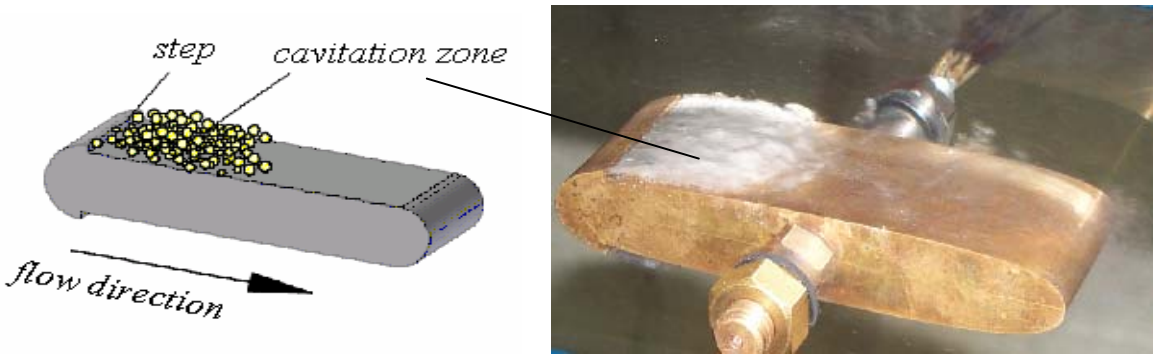

Figure 5.3.3: Cavitation behind a step of a symmetric profile (Heller [2000])

Figure 5.3.3 shows distinct cloud cavitation behind a step of a symmetric profile in a high velocity water flow. In turbulent pressure fields, the pressure causing cavitation inception is composed of the pressure reduction due to the acceleration of the fluid and the pressure reduction due to turbulent motion in the approach flow and interface. A cavitation nucleus moving along a body contour (Langrange-viewpoint) will be affected by both the pressure

reduction caused by the accelerated flow and the minimal pressure in the center of a vortex moving along with the approach flow or in the interface respectively, if this nucleus is drawn spirally into the vortex and dragged along.

In order to assess cavitation behavior, usually the cavitation number by Thoma [1925] is employed, which indicates a state of cavitation of limited size or a cavitation-free state. The Thoma number represents the relation of two pressures: the numerator is the pressure difference to the vapor pressure, preventing cavitation; the denominator is the dynamic pressure of the fluid, i.e. the pressure reduction causing cavitation. The presumption of the Thoma number is that cavitation inception occurs exactly when the vapor pressure p_V of the fluid is reached. The velocity q_∞, the density ϱ and the pressure p_∞ are measured values of the unperturbed approach flow.

$$\sigma = \frac{p_\infty - p_V}{\frac{\rho}{2} \cdot q_\infty^2} \tag{5.3.1}$$

Conventional cavitation theory assumes that cavitation processes at model and prototype are identical for geometrically similar bodies at an equal σ-value (compare eqn. 5.13) and independent from changes of physical parameters such as the body's size, flow velocity, temperature, type of fluid etc.. However, as known by experience and systematic investigations, this presumption is normally not applicable. Even at one and the same test body, significantly different degrees of cavitation can be observed if the body is, at equal σ-values, subjected to flows of various velocities and pressures (Keller [1996], Keller u. Rott [1997]). Additionally, differences in the viscosity of the fluid and the turbulence of the approach flow (Heller [1997]) extensively influence the degree of cavitation at a test body. However, all these scale effects can be superimposed by so-called "water quality effects", which affect the tensile strength of the fluid (e.g. Keller [1973, 1983, 1984, 1994, 1996], Keller u. Zielke [1976], Keller u. Prassad [1978], Keller und Eickmann [1989], Eickmann [1992]).

Cavitation is a phenomenon that can appear in all fluid flows. In most cases, however, the occurrence of this phenomenon is to be prevented or, since this is often impossible, reduced to a technically feasible minimum. For example, during operation of rotary pumps the decrease of delivery height due to cavitation can reach up to 3% without danger of significant material damage (brethren Sulzer, [Manual of Rotary Pumps - Kreiselpumpenhandbuch]. In some single technical applications the occurrence of cavitation can be desirable such as in sanitization of micro-surgical instruments or when degassing or mixing fluids. Cavitation is a very complex physical process, whose mathematical description has been insufficient due to various influencing parameters until today. International research in this area is still intense because of its fundamental economic importance (e.g. Keller, Rott, Stoffel, Striedinger [1999], Keller [2000, 2001], Keller, Pan, Yang [2003]).

5.3.2 Cavitation Inception

At first sight, research about cavitation inception does not appear very relevant in praxis since on many occasions far evolved cavitation with its respective impacts on machinery and parts such as vibration or erosion must be considered. Cavitation inception constitutes only the first visible signs of complicated cavitation states occurring in praxis but it is the only state of cavitation that can be defined sharply. All further processes are denominated evolved cavitation, which cannot be described clearly and thus reproducibly. For practical application in model measurements of cavitation test facilities, it is important that a cavitation number free from scale effects is known in order to be able to predict cavitation processes at the original.

The conditions for the occurrence of cavitation, i.e. local vaporization of the fluid under static or dynamic tensile strength, are closely linked with the state of the fluid regarding its tensile strength. Free phase interfaces are the pre-requisite for the transition of a fluid from the liquid to the vaporous state. The most relevant criteria for cavitation susceptibility are therefore size and number of stabilized gas or vapor bubbles, so-called cavitation nuclei. Assessing the properties of water merely by its gas content is problematic because only the undissolved part, the so-called nuclei, must be viewed as the relevant parameter influencing cavitation susceptibility. Thus, for the prediction of cavitation behavior, some information about the fluid's characteristics in model and original size is also required. As already described in chapter 4, methods for the dynamic tensile stress measurement are available for this purpose.

Eckeret [1930] already constituted as a result of his cavitation experiments that there was no generally acceptable law of similarity for transfer of model measurement results to the prototype. Even experiments with identical or similar test bodies in various test facilities produced different results. Countless examples can be found in praxis where at respective cavitation parameters, matching those of the prototype, no cavitation could be observed at the model, whereas distinct cavitation was exhibited at the prototype under equal conditions.

The ITTC [1978] initiated extensive comparative tests with special profiles at various cavitation tunnels (e.g. in Germany, France, the Netherlands, the USA and Shweden). The test program's aim was to determine the inception of different cavitation types as a function of flow velocity and gas concentration. The results shown in figure 5.3.4 prove great deviations among the individual test facilities and observers. The σ-values for cavitation inception differ by upto 150% among the several test facilities, which demonstrates the dilemma of non-comparable test results.

The test results in figure 5.3.4 bear out the remarkable fact that the distinctly different results have been produced in spite of equal test conditions. However, since possible scale effects due to velocity, size, turbulence and viscosity were thus practically eliminated, the influence of the water quality on the test results consequently remains as the dominant effect. It seems reasonable that the evaluation of cavitation experiments without information about water quality is problematic. Therefore, the necessity for developing suitable measurement methods as described in chapter 4 becomes apparent.

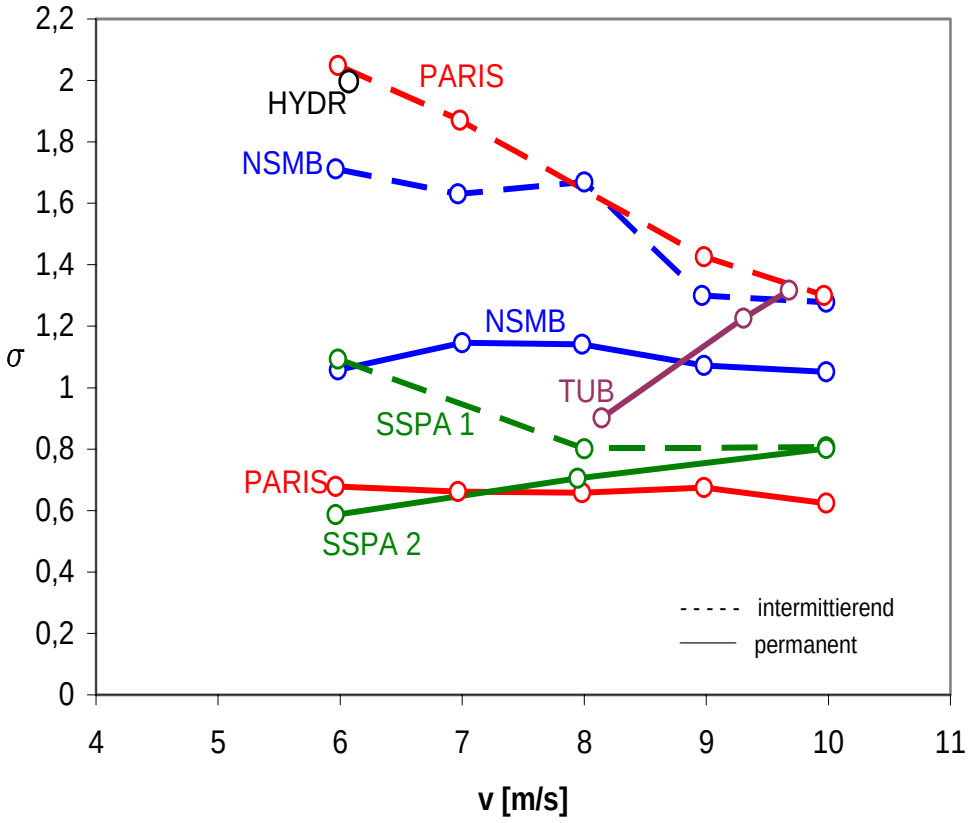

Figure 5.3.4: Measurement results ITTC [1978]

A summarizing report about the current state of research in this area until 2002 is provided by the Specialist Committee on Water Quality and Cavitation of the International Towing Tank Conference (ITTC, 2002). Essential articles in this context have been published by Acosta [1970], Arndt [1994], Billet [1988], Ceccio [1997], Gates [1980], Gindroz [1996], ITTC [1990, 1993, 1996], Shen [1994]. The most important articles about the correlation of water quality and cavitation inception were undoubtedly provided by Keller [1983 … 2003], whose most significant results are collected subsequently. Keller developed a measurement method, described in chapter 4.3.6, for determining the tensile strength of water until routine application in order to use this method in comprehensive test series for determining actual scale effects. The necessity to make use of this measurement method in cavitation experiments is exemplified by the water quality effects (tensile stress) on cavitation at a circular cylinder with hemispherical front surface, as shown in figure 5.3.5.

Figure 5.3.5: Tensile strength effect on cavitation at a circular cylinder by Keller[1996]

In the left photo no cavitation can be observed due to a water quality with high tensile strength, whereas on the right hand side after reducing the tensile strength, at the same flow velocity and equal σ- value, severe cavitation can be noticed.

Figure 5.3.6 shows the development of cavitation at a NACA-profile in three water qualities under otherwise completely equal conditions. In the left photograph, tensile strength is high and no cavitation can be observed. In the middle photograph, at zero tensile strength the beginning vortex cavitation is noticeable while in the photograph on the right, at negative tensile strength, fully developed vortex cavitation and single bubble cavitation is occurring.

The conventional relation of equation 5.3.1 for the cavitation number σ is associated with the presumption that at the break of the fluid (cavitation inception) the critical pressure p_{krit} equals the vapor pressure p_d of the fluid. The actual critical pressure, however, equals the fluid's tensile strength p_{zug}, which can sometimes be influenced within certain limits in a cavitation tunnel.

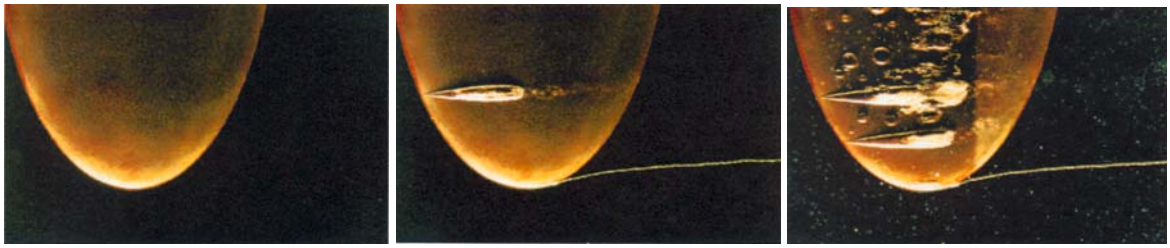

Figure 5.3.6: Effect of tensile strength on cavitation at a NACA-profile by Keller [1996]

Calmed water with high gas content can carry high concentrations of large gas bubbles, which prevents this water from accepting tensile strains. This can even lead to enormous growth of these bubbles before reaching vapor pressure in areas of lower pressure and thus, a state similar to cavitation arises. This is called negative tensile strength of the water or pseudo cavitation. On the other hand, clean, degassed and calmed water can reach high tensile strains, which lets cavitation nuclei only develop if pressures are reached more or less below the vapor pressure. Thus, it becomes clear that at cavitation inception the critical pressure of a fluid may be above or below the vapor pressure, and only in exceptional cases or by special manipulation of the fluid, the critical pressure equals the vapor pressure.

The cavitation number σ can be made independent from water quality effects by replacing the vapor pressure p_V with the current critical pressure p_{krit} in equation (5.3.1). Thus, a modified cavitation number σ´ is obtained with.

$$\sigma' = \frac{p_\infty - p_{krit}}{\frac{\rho}{2}\cdot q_\infty^2} = \frac{p_\infty - (p_V - p_{ts})}{\frac{\rho}{2}\cdot q_\infty^2} = \frac{p_\infty - p_V}{\frac{\rho}{2}\cdot q_\infty^2} + \frac{p_{ts}}{\frac{\rho}{2}\cdot q_\infty^2} = \sigma + \Delta\sigma \qquad (5.3.2)$$

The necessary pressure reduction below the vapor pressure is specified by the tensile strength p_{ts}.

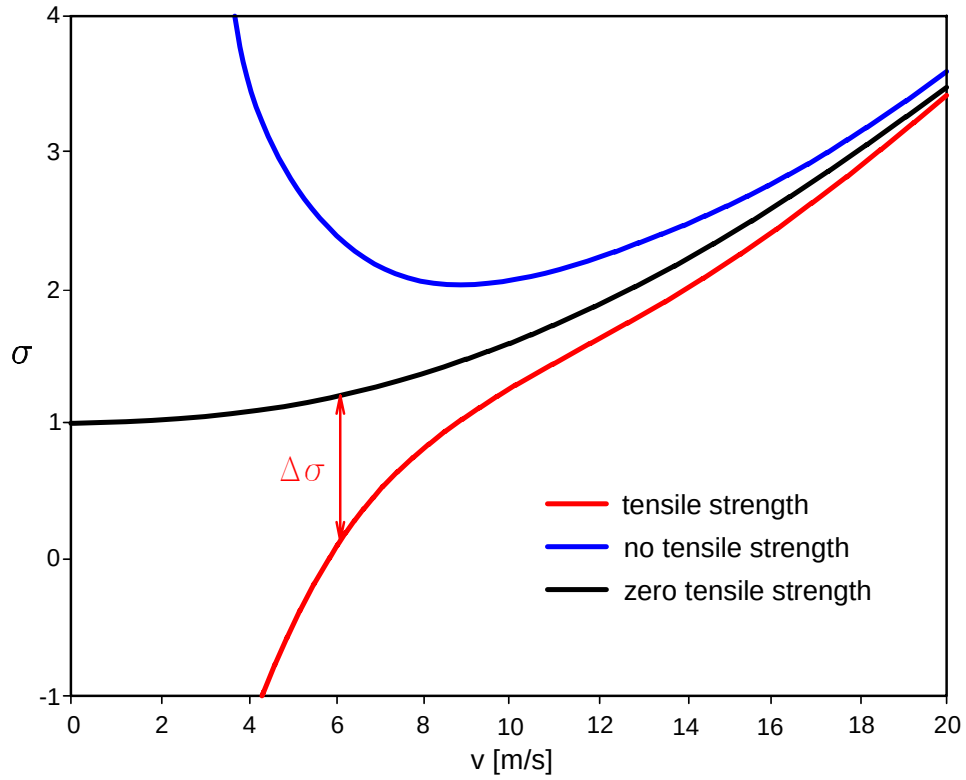

Figure 5.3.7: Schematic depiction of test results for cavitation in water with and without tensile strength by Keller [1994]

As shown schematically in figure 5.3.7, the effect of a fluid's tensile strength on cavitation experiments can be significant. While at high velocities, $\Delta\sigma$ is relatively small for any given p_{ts}, it will increase drastically at low velocities. This water quality effect can therefore lead to confusing test result in cavitation experiments, as mentioned above. The effect can decidedly outweigh actual scale effects and may therefore lead to incorrect interpretations of a body's cavitation behavior.

Systematic research about cavitation inception considering water quality has provided evidence that the influence of tensile strength on test results can be avoided if nuclei-saturated water is used for the tests. In this case, the water contains a sufficient number of cavitation nuclei whose critical diameter is reached within the range of vapor pressure. If in a tunnel, the pre-treatment of the water is either impossible or not desired, the transfer to a different tensile strength according equation oben: 5.3.2 is possible.

5.3.3 Cavitation Erosion

As discussed above, the occurrence of cavitation induces undesirable effects. Except for noise emission and vibration caused by strong pressure fluctuations, cavitation erosion probably has the severest impact on hydraulic machinery and constructions. Figure 5.3.8 shows examples of damages caused by cavitation erosion at a race boat propeller and a valve case.

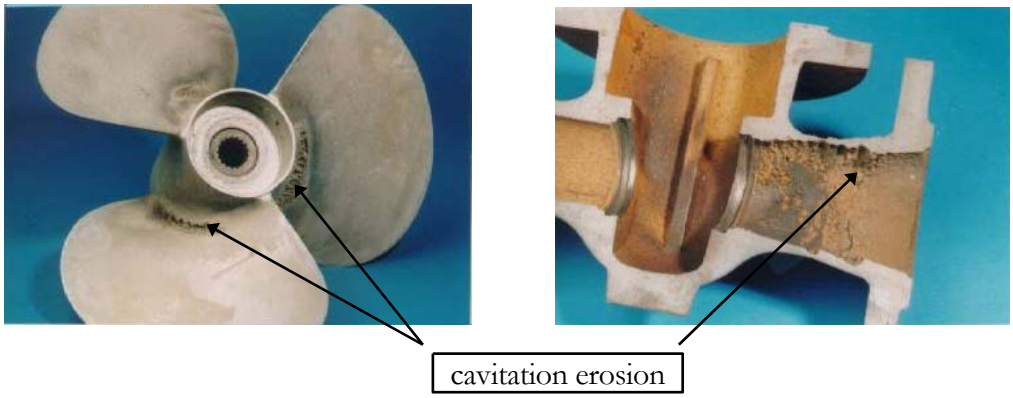

Figure 5.3.8: Damage caused by cavitation at a race boat propeller and a valve case (photographs by Keller [1984])

Cavitation damage by erosion at hydraulic facilities becomes apparent particularly quickly, because the material concrete exhibits only little resistibility against cavitating flows. This may have dramatic effects on the safety of specific constructions, as can be seen at the destroyed spillway chute of a floodwater relieving facility (fig. 5.3.9).

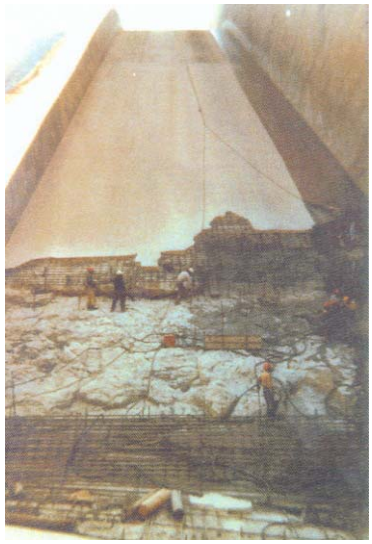

Figure 5.3.9: Destroyed spillway chute of a flood water relieving facility (Huber [2004])

In 1974, due to severe cavitation erosion, the bypass tunnel of the Tarbela embankment dam in Pakistan, which had been in operation with flow velocities up to 30 m/s for over a month, collapsed over a length of 60 m (see fig. 5.3.10, Kenn und Garrod [1981]). The tunnel with a diameter of 14 m had been damaged by cavitation erosion over a length of 800 m.

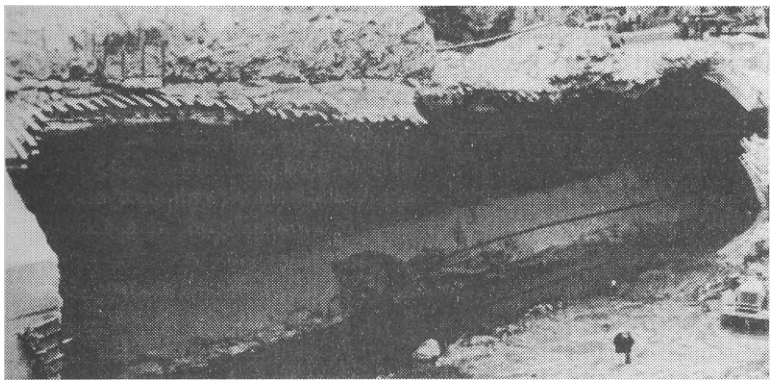

Figure 5.3.10: Destruction of a bypass tunnel of the Tarbela embankment dam caused by cavitation erosion (Garrod [1981])

In order to apprehend how cavitation can cause such enormous damage, the behavior of bubble nuclei must be analyzed in greater detail. Due to flow-induced pressure fluctuations, bubble nuclei become instable and cavitation bubbles appear. These are transported by the flow into areas of higher pressures where they collapse implosively. In free flow, this is a nearly symmetrical process, in relation to the bubble shape. It is denominated as spherically symmetric bubble collapse with subsequent rebound of the bubble after which shock waves are propagated spherically.

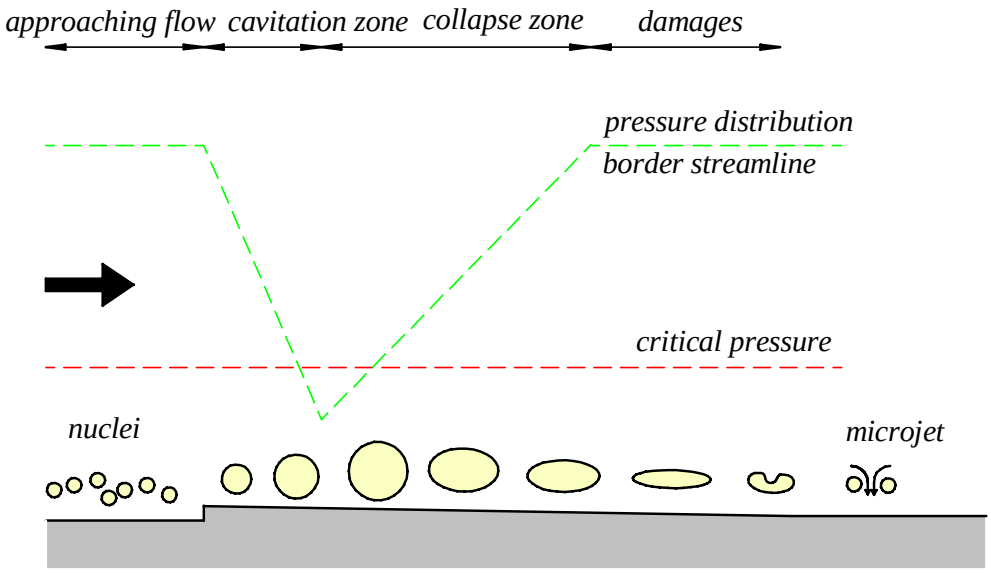

Figure 5.3.11 Schematic sketch of a cavitation zone and erosion zone after Huber [2004]

Bubbles case walls collapse asymmetrically by denting in on one side, which generates a micro-jet across the bubble that collides with the wall at high velocity (see figs. 5.3.12 and 5.3.13). According to Lauterborn [1980], this jet is between 10 and 100 µm in diameter, may reach a velocity of 200 m/s and produces pressures of 1500 bar. By means of bubble-dynamic examinations, the possible velocity of the fluid jet was estimated even to 10^3 m/s, and the induced pressures were calculated as high as 10^5 bar (Choffat et al. [1980]). The time of impact on the walls is specified in the order of ns to µs.

Figure 5.3.12: Imploding cavitation bubble at a wall with micro-jet (Suslick [1989])

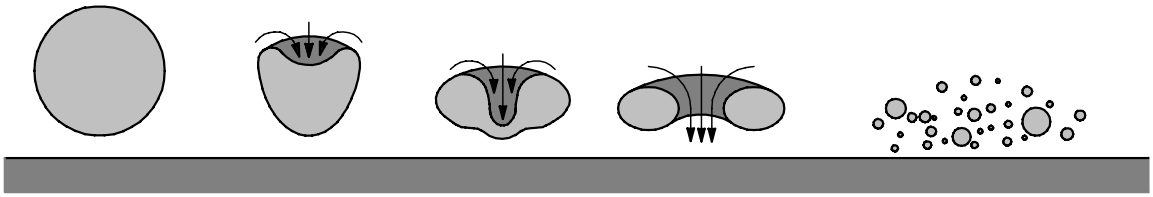

Figure 5.3.13: Schematic sketch of the implosion process of a cavitation bubble after Knapp et al. [1970]

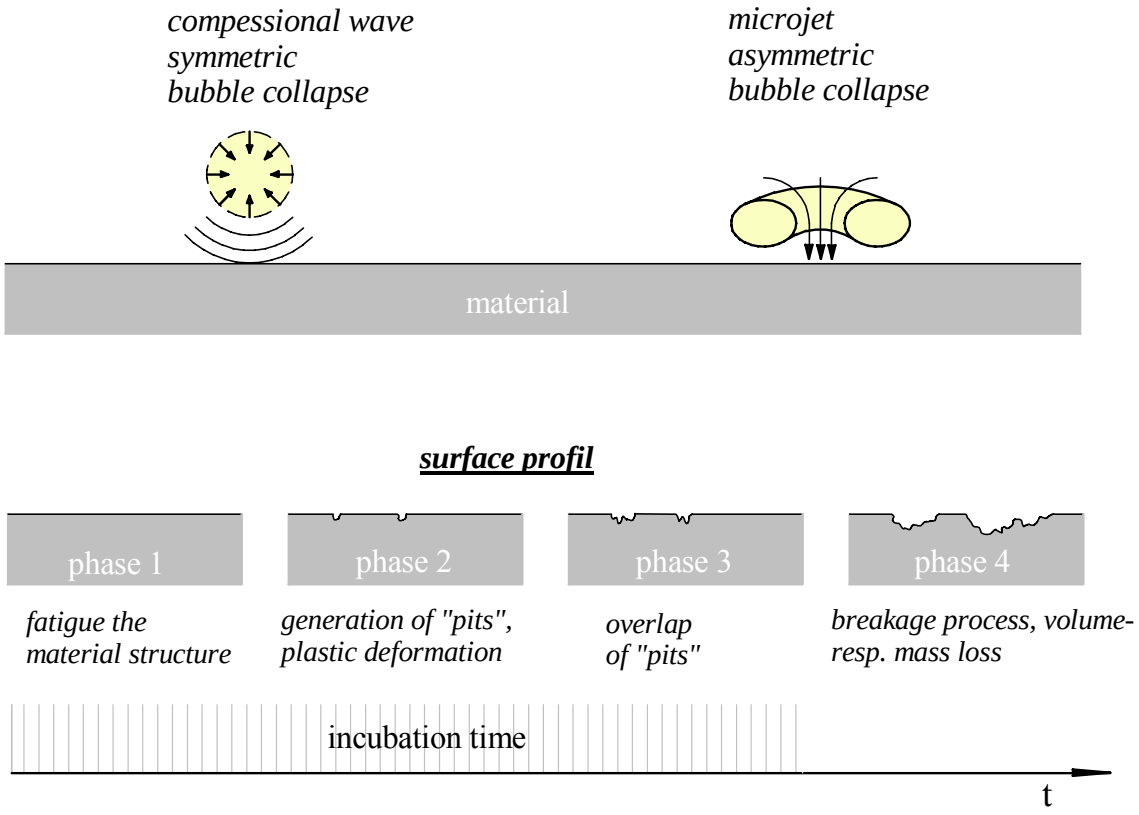

Figure 5.3.14 Schematic sketch of erosive aggressiveness and temporal alteration of the material surface after Huber [2004]

Affecting the materials confining the flow, the damaging process induced by cavitation is of very complex nature. Namely, material erosion only starts after a certain incubation time during which, externally hardly noticeable, the material's microstructure is being modified and after a period of strain hardening, material cohesion will reduce. Initially, the surface is deformed plastically, which can be observed as small crater-like indentations, so-called "pits", followed by cracks. Only when the energy supplied to the material (mostly by microjets and shock waves caused by collapsing bubbles) exceeds a threshold, will a speedy and deep-reaching material removal begin (Knapp et al. [1970]).

The strain of the material caused by cavitation is characterized by the so-called erosive aggressiveness of the flow, which is specified by the temporal and spatial distribution of impacts due to bubble collapses. The process of erosive aggressiveness is shown schematically in figure 5.3.14.

Figure 5.3.15 schematically shows the volume loss ΔV or, respectively, the mass loss Δm against the time of impact [Huber, 2004]. A wide range can be identified where the rate of volume loss

$$\Delta \dot{V} = \frac{\Delta V}{\Delta t} \tag{5.3.4}$$

or the rate of mass loss respectively

$$\Delta \dot{m} = \frac{\Delta m}{\Delta t} \tag{5.3.5}$$

have a constant value. If the evolved indentations do not trigger further cavitation, that value may decline asymptotically approaching zero in later progression due to the so-called hole damping effect. Thus, caused by erosion, the distance between the material surface in the erosion area and the place of bubble collapse is increased to the an extend that the micro-jet's effect is reduced.

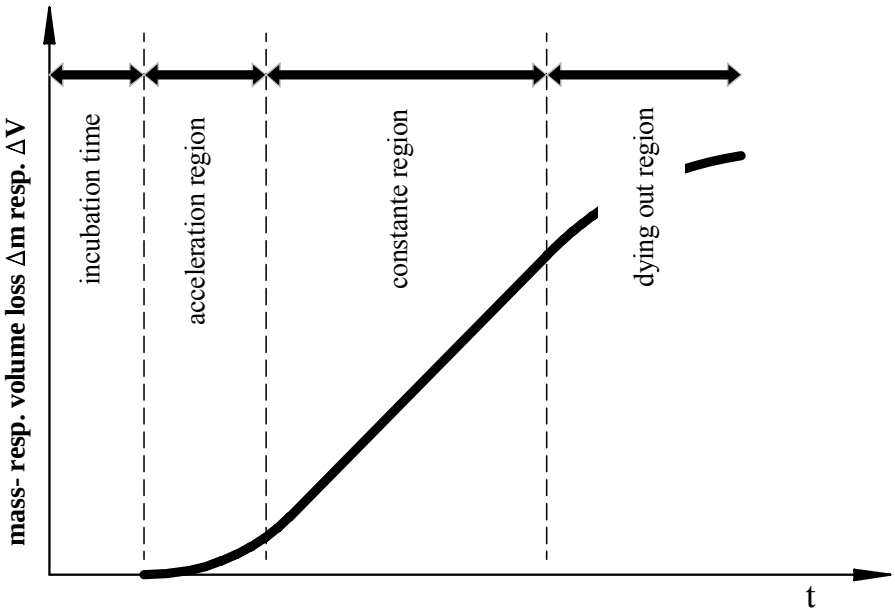

Figure 5.3.15 Schematic graph of the temporal progress of volume and mass loss after Huber [2004]

Volume loss against time and the area of the erosion zone Aerosion is also used as a measure of material removal. The following equation (5.3.6) uses MDPR ('**m**ean **d**epth of **p**enetration **r**ate') and MDDR ('**m**ean **d**epth of **d**eformation **r**ate') interchangeably:

$$\mathrm{MDPR} = \mathrm{MDDR} = \frac{\Delta V}{\Delta t \cdot A_{\mathrm{Erosion}}} = \frac{\Delta \dot{V}}{A_{\mathrm{Erosion}}} \tag{5.3.6}$$

For the realization of cavitation experiments, various test facilities are utilized which differ regarding their way of generating cavitation. The most common facilities are closed circuit tunnels similar to the cavitation tunnel depicted in figure 5.3.2 where cavitation is generated by flow around a cavitator fitted into the measuring section. The test body to be examined can be integrated into the cavitator. They may be positioned apart from each other, or (more rarely) the cavitator is the test body itself.

Built by Bux [1987], the rotating disk shown in figure 5.3.16 is another test facility with so-called flow-induced cavitation. Test body and cavitator are fastened to a disk (diameter of 400 mm) rotating at high velocity in a circular space that is filled with the test fluid. The pressure inside the circular space and disk velocity can be controlled. The maximum velocity of test body and cavitator in the system was 36 m/s. In contrast to the cavitation tunnel, here the test body and cavitator are moved against the fluid so that a certain relative velocity between fluid and test body is reached in operation and, in comparison to the cavitation tunnel, erosion intensity is significantly higher.

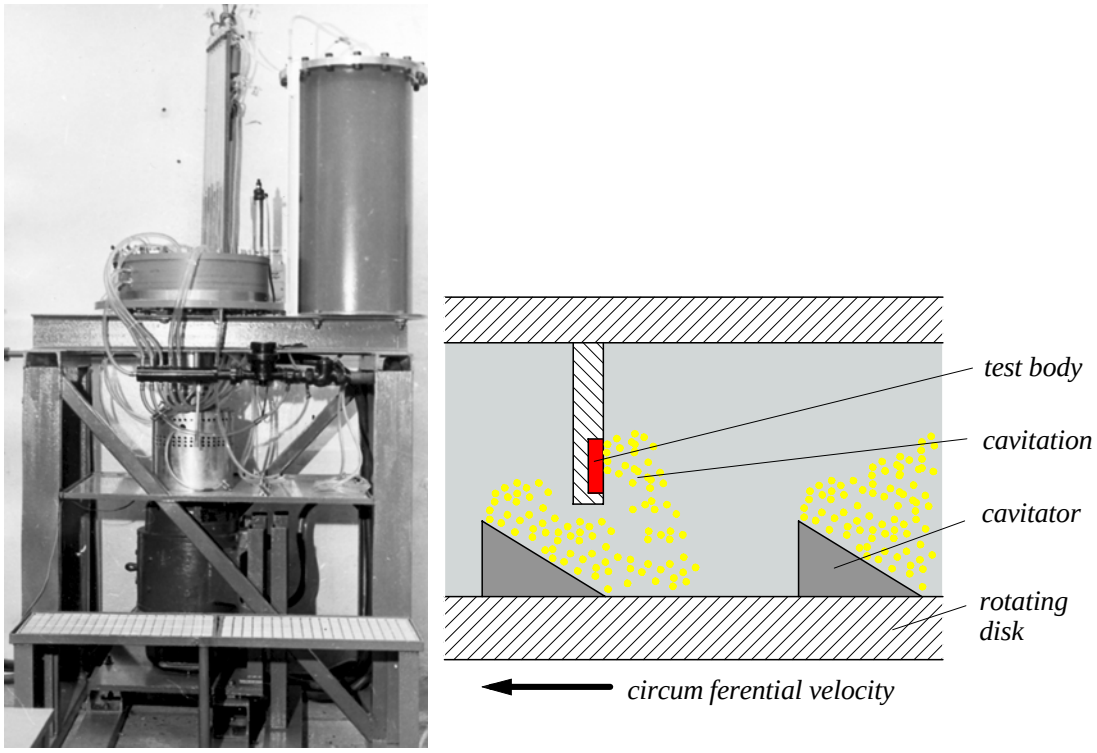

Figure 5.3.16 Test facility "rotating disk" at TU Dresden (left) with schematic sketch of the active principle **Figure 5.3.17**

a) Damages against time at Babbitt metal with u = 36 m/s and σ = 0.72

t = 6 hours t = 9 hours t = 15 hours

b) Damages against velocity at aluminum with t = 1,5 min and σ = 0,56:

u = 28 m/s u = 31 m/s u = 35 m/s

c) Damages at inflicted indentations in lead with t = 30 min u = 30 m/s and σ = 0,75:

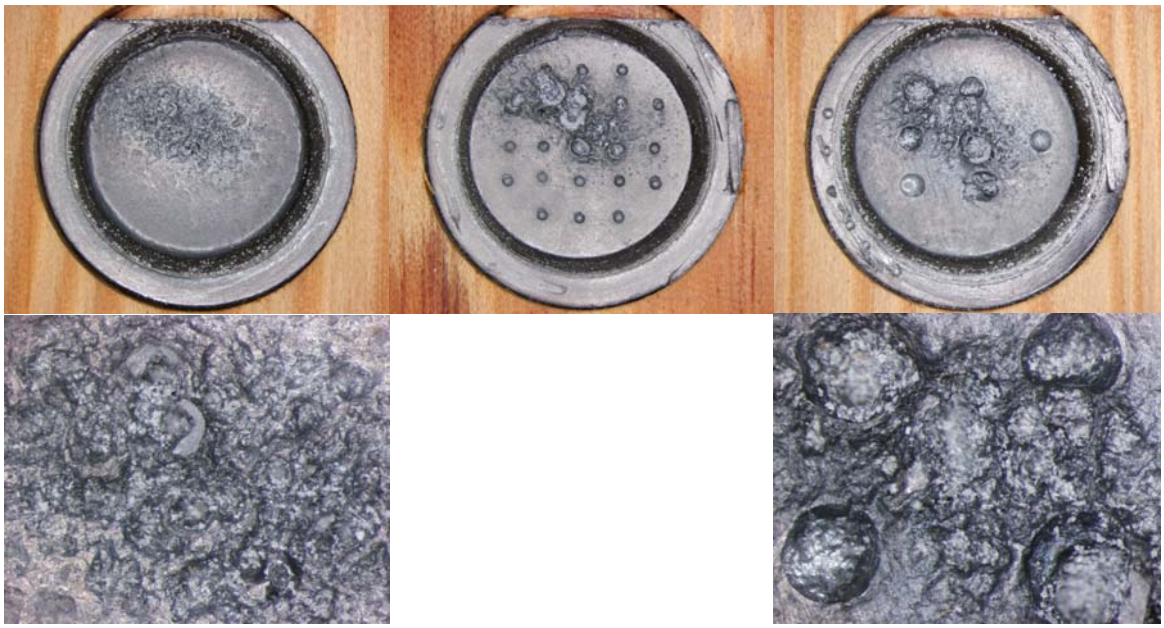

low indentations deep indentations

Figure 5.3.18: Correlation cavitator-test body and images of damages at test bodies of various materials after Bux [1987]

Similarly high erosive intensities can be reached in the so-called steel chamber, depicted as principle sketch in figure 5.3.19. This method is based on an open cavitating jet entering the test chamber, which is filled with the same test fluid, through a nozzle. By setting the flow conditions, it is ensured that the open jet is cavitating when leaving the nozzle. Hitting the test body, the cavitating jet is deflected radially symmetrically. This leads to the typical circular erosion zone with an uneroded area in the center.

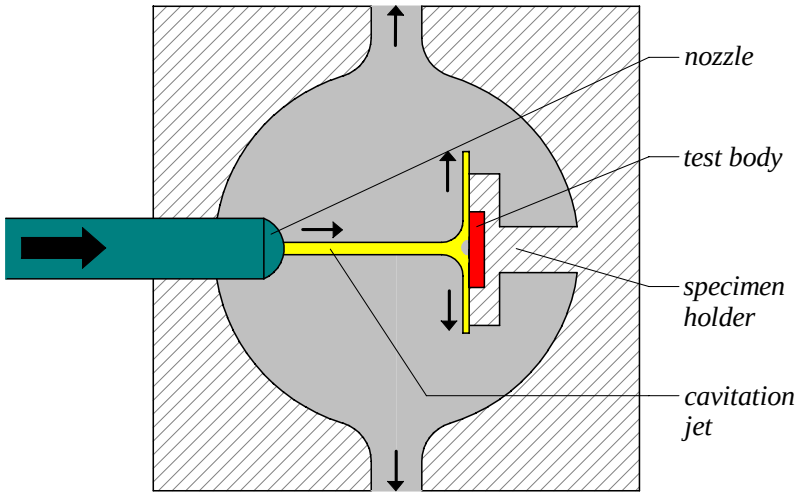

Figure 5.3.19 Principle sketch of a steel chamber with test body

The device depicted as principle sketch in figure 5.3.20 can also be used for examination of materials regarding cavitation erosion in fluids. By means of an oscillator, an acoustic pressure field at 20 kHz is generated, causing cavitation in the gap between the oscillator and the test body.

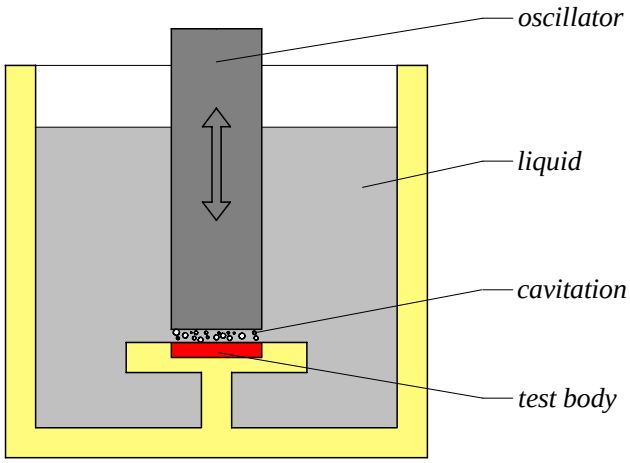

Figure 5.3.20 Principle sketch of vibration-induced cavitation after Trevena [1987]

In order to measure the erosive aggressiveness of a cavitating flow, the alteration of the material surface against time and the material is examined. Preferably, soft materials (e.g. lead, Babbitt, copper or aluminum) are utilized so that significant deformation and measurable mass or volume loss is achieved within a short time. After dismounting the test body, these characteristics can be determined by means of mechanical and optical methods as well as weighing.

This can be done by so-called thin film activation (Bux [1987]). In an accelerator, positively charged particles are fired at material samples. These particles penetrate the test surface up to depths of 300 μm where they excite nuclear reactions generating radioactive isotopes of the alloy elements. Hardness, structure, microstructure and electro-chemical potential of the material remain unchanged. Consequently, the sample is emitting low β- and γ-radiation (total intensity of 10^5 … 10^6 Bq). The energy spectra of the γ-radiation before and after erosion are measured, specifies the activity of individual nuclides. The decrease of activity is therefore a measure of material erosion and thus, of the cavitating fluid's aggressiveness. Advantages of this method lie in the quasi-continuous measurement and its high sensitivity ($\Delta m \approx 10^{-11}$ g)

By coating test bodies with certain materials (or/and special paints) the erosive aggressiveness can be determined by analyzing the eroded area by means of special image processing methods. Here, too, the test cycle must be interrupted. Because of their minor importance, other methods such as the measurement of pressure impulses caused by bubble implosions, the measurement of macroscopic pressure fluctuations as well as sound measurements shall only be mentioned here briefly..

According to Huber [2004], hardly any information about the influence of water quality can be found in respective literature. Böhm [1998] examined the dependency of the pitting rate on the total gas content by setting three different gas contents. He found highest erosivity for a medium gas content, which can be explained with the high attenuation at high gas contents and the prevailing tensile stresses at low gas contents. Regarding the influence of the free gas content on cavitation erosion, similar results have been published by several authors (Peterka [1953], Hutton and Meshhedani [1992], Arndt et al. [1995], Eisenhauer [1995], Winter et al. [1998]). Concordantly, they observed that by aerating the cavitating flow, cavitation erosion could be reduced or even prevented.

However, until today, only Huber [2004] has examined the influence of the water's tensile strength on cavitation erosion in detail. To determine tensile strength during his erosion experiments he employed the measuring method by Keller [1983], which is described in chapter 4.3.6. It became clear that during cavitation tunnel experiments (see figure 5.3.2) with its well-developed cavitation, sufficient cavitation nuclei are always present. They are the reason why, independent from the set dissolved gas content, the water's tensile strength constantly remains zero. Thus, proof is furnished that there is no influence of the tensile strength on cavitation erosion in circuit tunnels since it is always nil. Additionally, it must be noticed that under these test conditions the dissolved gas content has no influence on the tensile strength of the water.

Huber [2004] was also first to examine the influence of the dissolved gas content on the erosion rate during cavitation experiments in circuit tunnels. To determine the dissolved gas content, equation (5.3.7) was used:

$$O_2[\%\ \text{saturation}] = \frac{p_\infty}{p_{atm}} \cdot 100 \tag{5.3.7}$$

which had resulted from numerous tensile strength measurements at the cavitation tunnel mentioned above. At a test track's reference pressure of p_∞ = 0.5 bar and the atmospheric pressure of p_{atm} = 1.0 bar, a dissolved oxygen content of O_2 = 50% would be necessary to obtain tensile strength free water.

The erosion rate is defined as volume loss per time according to equation (5.3.4):

$$ER = \frac{\Delta V}{\Delta t} = \Delta \dot{V} \ [mm^3/h] \tag{5.3.8}$$

Five test cycles to examine volume loss were conducted. In contrast to equation (5.3.7), the dissolved gas contents were not adjusted to fit the respective test tracks' reference pressure p_∞ but were chosen constant at O_2 = 63% saturation. According to equation (5.3.7), this meant a more or less strong saturation of the water for each test series, as can be seen in table 5.3.1.

σ	O_2 saturation after (5.3.7) (nominal)	O_2 saturation dialed (actual)
1,11	95%	63%
1,42	121%	63%
1,52	129%	63%
1,63	138%	63%
1,77	150%	63%

Table 5.3.1: Nominal and actual dissolved gas contents during the experiments to ascertain the influence of dissolved gas content on erosion rate after Huber [2004]

Figure 5.3.21 clearly shows the influence of the lower dissolved gas content. In the experiments with constant dissolved gas content, erosion rates are higher by the factor 2 to 3.5 despite the zero tensile strength.

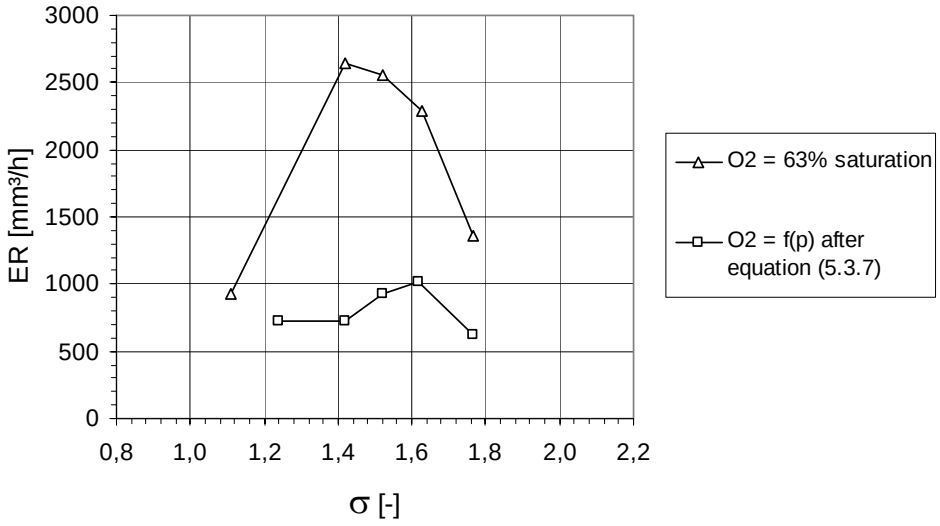

Figure 5.3.21 Comparison of erosion rates at dissolved gas contents after Huber [2004]

This result is certainly plausible since, with decreasing dissolved gas content, the attenuating effect of the gas inside the cavitation bubble is lessening during the implosion process. Thus, the released energy for the microjet is increasing and so is the erosive aggressiveness of the water (Young [1989]). On the other hand, this is just the reason why a high dissolved gas content hinders the erosion process, particularly with an additional attenuating effect due to the presence of undissolved gas bubbles.

5.4 Lift, Drag and Loss

5.4.1 Cavitating Flows

Stoffel & Striedinger [2002] provide an overview of the influence of cavitating flows on the friction factor c_W (eqn. (5.4.1)) and the lift coefficient c_A (eqn. (5.4.2)). Using the measured forces of drag F_W and lift F_A, the dimensionless characteristics

$$c_W = \frac{F_W}{\frac{\rho}{2} \cdot q_\infty^2 \cdot A} \qquad (5.4.1) \qquad \text{and} \qquad c_A = \frac{F_A}{\frac{\rho}{2} \cdot q_\infty^2 \cdot A} \qquad (5.4.2)$$

are calculated and depicted against the degree of processing cavitation σ. This progression line shows beginning or light cavitation, advanced cavitation and finally, fully developed cavitation. The smaller the σ-values, the lager the areas become that are filled with vapor bubbles until super-cavitation is reached eventually.

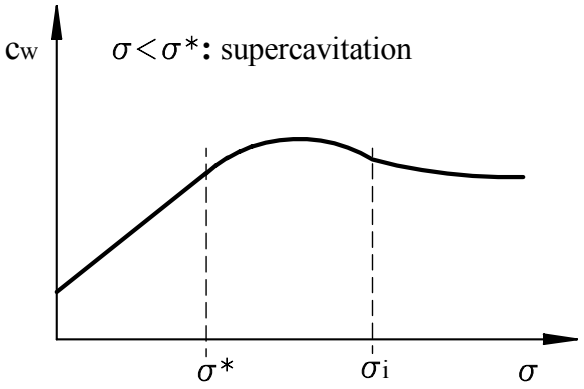

Figure 5.4.1 c_W - Characteristic of symmetrical, slim bodies after Striedinger [2002]

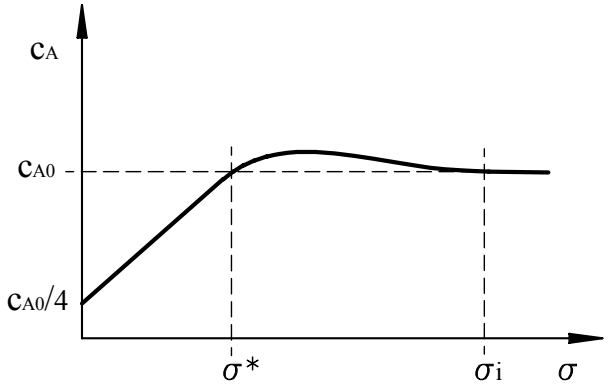

Figure 5.4.2 c_A - Characteristic of progressing cavitation after Striedinger [2002]

The characteristic of the c_W-value at symmetrical, slim bodies is shown in figure 5.4.1. Beginning or light cavitation can foster transition and therefore, increase frictional drag downstream and reduce pressure drag. Advanced cavitation has only little influence on the frictional drag, however, pressure drag increases. Super-cavitation causes a significant decline of the c_W-values with falling σ-values because vapor pressure prevails all over the downstream side, while on the upstream side, the decreasing fluid pressure p_∞ is effective.

At lift-producing profiles, the lift coefficient c_A is also dependent on the σ-value in case of cavitation. As can be seen in figure 5.4.2, beginning or light cavitation has only little influence on c_A. Even a positive effect is possible if the pressure distribution on the suction side is changed respectively by cavitation. Advanced cavitation leads to lower c_A-values because of the limitation of the minimal pressure at vapor pressure. Super-cavitation causes a linear decline of c_A with σ since vapor pressure is on the vapor-covered side of the profile while on the water-covered side, the mean pressure declines approximately proportionally with p_∞.

Similar observations can be made concerning the influence of cavitating flows on the loss coefficient in pipes, fittings or bends.

$$\varsigma_V = \frac{\Delta p_V}{\frac{\rho}{2} \cdot q_\infty^2} \tag{5.4.3}$$

While beginning or light cavitation has hardly any qualitative influence on ς_V, advanced cavitation increases the loss coefficient significantly in both adjacent and detached cavitation, as can be seen in figure 5.4.2 These different influences are caused by the obstructive effect of the cavitation bubbles or the cavitation areas respectively, leading to increasing flow velocity in the cavitation area with higher friction and subsequent delay and mixing downstream of the cavitation area. Full cavitation causes a steep rise of ς_V until reaching the throughput limit.

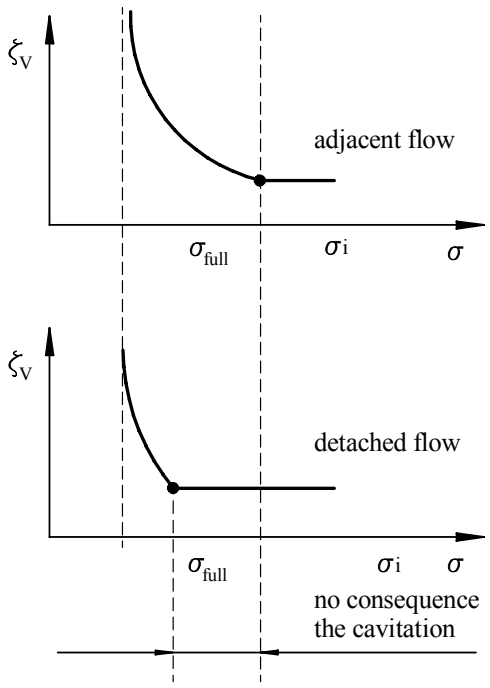

Figure 5.4.3 Correlation between the degree of cavitation progress σ and ς_V after Striedinger [2002]

5.4.2 Electrically Conductive Fluids

(after Weier [2000 - 2005])

Electrically conductive fluids such as acids, bases as well as the salt water of the oceans can be affected systematically by electro-magnetic fields. At body surfaces, these fields generate Lorentz-forces in the area close to the walls, which can be used to attenuate (and also to intensify) vortex motion. Flow detachment can be prevented and drag can be reduced many times over. Dependent on the electrical conductivity σ_L of the fluid, two types can be distinguished:

1. In fluids of high conductivity such as liquid metals with $\sigma_L \approx 10^6$ S/m, high current densities can be produced by application of an external magnetic field. Together with the applied magnetic field, these current densities cause Lorentz-forces that may significantly influence the flow.
2. In fluids of low conductivity $\sigma_L \approx 10$ S/m as it can be found in electrolytes and in ocean water, the currents generated by a moderately strong magnetic field ($B \approx 1T$) are too low to considerably influence the flow. In order to reach a noticeable effect, an additional external electric field must be applied. (see principle sketch in figure 5.4.4)

The Lorentz-force $\vec{f}_L$ is described by the Cartesian product of electrical current density $\vec{j}$ and magnetic induction $\vec{B}$:

$$\vec{f}_L = \vec{j} \times \vec{B} \tag{5.4.4}$$

Proportional to the electric conductivity σ_L, the current density $\vec{j}$ is generated in a magnetic field $\vec{B}$ by an electric field $\vec{E}$ and the fluid flow $\vec{v}$:

$$\vec{j} = \sigma_L \cdot \left(\vec{E} + \vec{u} \times \vec{B}\right) \tag{5.4.5}$$

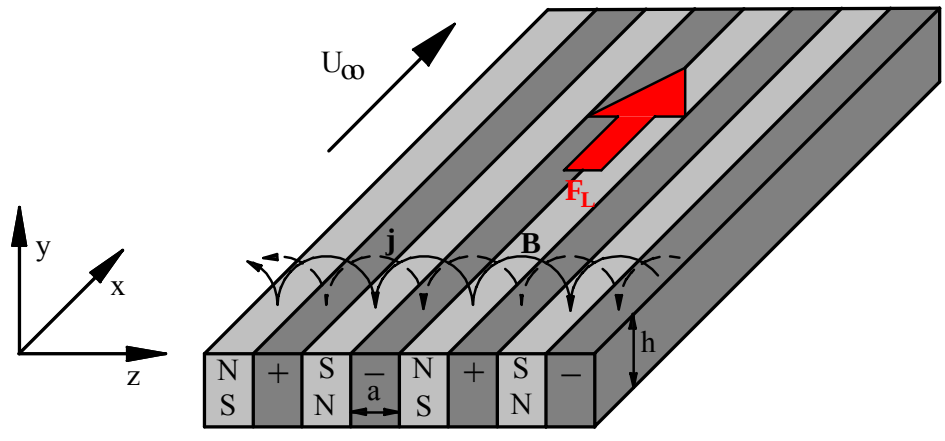

Figure 5.4.4 Stripe order of electrodes and magnets to generate a wall-parallel Lorentz-force after Weier [2000]

Due to the low conductivity σ_L of typical electrolytes, the currents caused by the motion within the magnetic field are so low that they do not produce noticeable force action. This is why, in addition to the external magnetic field, an external electric field must be applied here. Provided that the induced magnetic field is weak compared to the total field, the Lorentz-force can be calculated only from the applied fields. Thus, force distribution is independent from the flow itself. The complete equation of motion for the resulting flow is represented by the Navier-Stokes-equation for incompressible fluids considering the Lorentz-force:

$$\frac{\partial \vec{u}}{\partial t} + (\vec{u} \cdot \nabla)\vec{u} = -\frac{\nabla p}{\rho} + \nu \nabla^2 \vec{u} + \frac{\vec{j} \times \vec{B}}{\rho} \tag{5.4.6}$$

After the usual interface simplifications, the interface equation for a plane plate according to Tsinober & Shtern [1967] can be written as:

$$u\frac{\partial u}{\partial x} + v\frac{\partial u}{\partial y} = \nu \frac{\partial^2 u}{\partial y^2} + \frac{\pi}{8}\frac{j_0 \cdot M_0}{\rho} \cdot e^{-\frac{\pi}{a} \cdot y} \tag{5.4.7}$$

with the additional term for the Lorentz-force density:

$$F = \frac{\pi}{8} \cdot j_0 \cdot M_0 \cdot e^{-\frac{\pi}{a} \cdot y} \tag{5.4.8}$$

j_0 : current density; M_0 : magnetization a : distance between the electrodes, magnets; y : distance to the wall

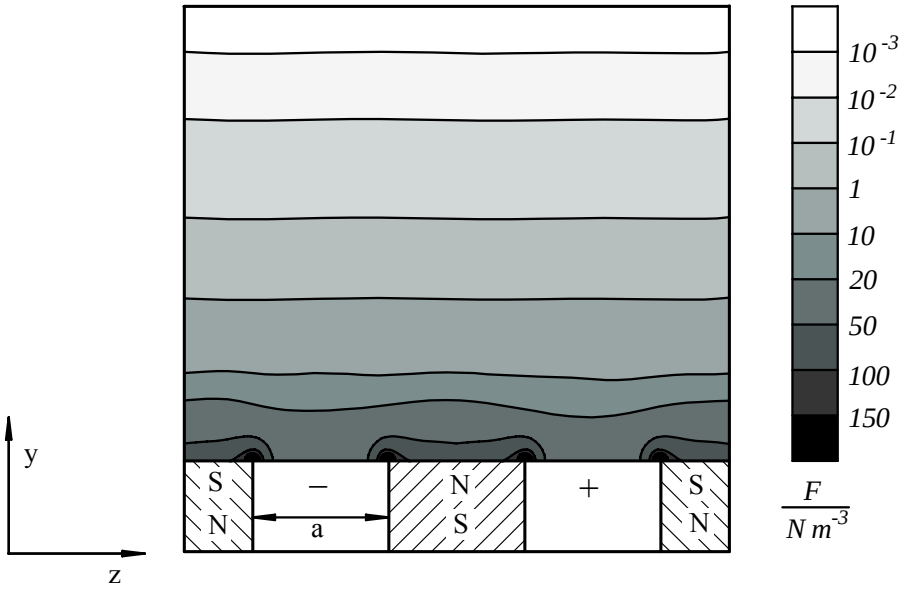

Figure 5.4.5 Lorentz-force over the order of electrodes and magnets, calculated after Weier[2000]

Figure 5.4.5 shows the density distribution of the Lorentz-force at a model plate, which results from a combination of the applied magnetic and electric field. It is important to acknowledge that the force density is not simply described as a function of the distance to the wall but it also varies transversely. This inhomogeneity, particularly near the wall, may influence the transition of the interface.

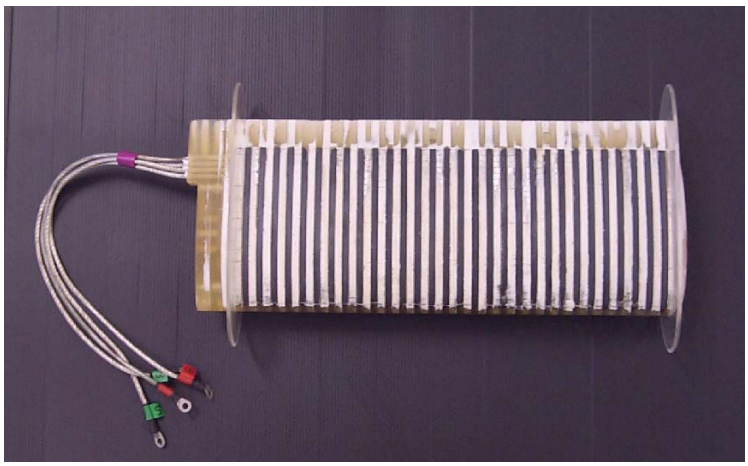

Figure 5.4.6 Model of a rudder, consisting of electrode segments and magnet segments (Weier [2005])

Figure 5.4.6 shows the model of rudder, which consists of electrode and magnet segments, as it was used for respective measurements.

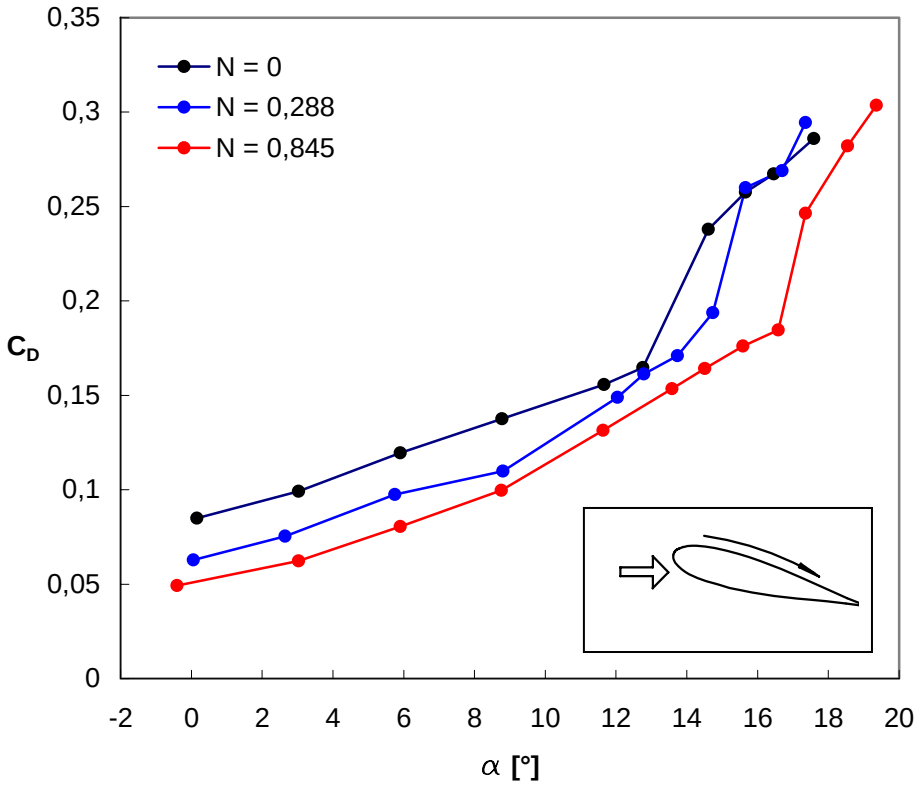

Figure 5.4.7 Drag coefficients c_D against the approach angle α at various interaction parameters N at a rudder after Weier [2005]

The effect of the actual Lorentz-force (e.g. on the drag coefficient c_D) is illustrated by the diagram in figure 5.4.7. The greater the interaction parameter N, the lower is the drag coefficient at equal approach angle α of the profile.

The interaction parameter N is a measure of the force action that is described by the ratio of the electro-magnetic force to the force of inertia.

$$N = \frac{j_0 \cdot B_0 \cdot L}{\rho \cdot q_\infty^2} \tag{5.4.9}$$

j_0 - current density
B_0 - magnetic field
L - characteristic length (e.g. profile depth or plate length)
ρ - density of the fluid
q_∞ - velocity of the approach flow

The improvement of lift at a model rudder due to detachment prevention is depicted in figure 5.4.8:

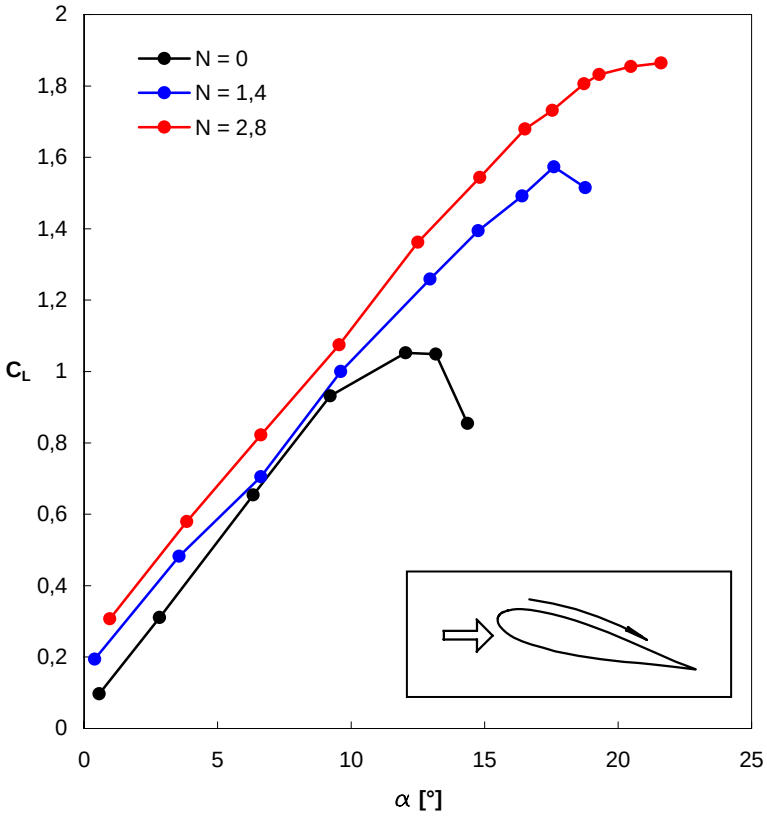

Figure 5.4.8 Lift coefficients c_L against the approach angle α at different interaction parameters N at a rudder after Weier [2005]

Figure 5.4.9 shows the flow around a plane plate angled at 18° and the dimensions 130 x 140 x 6. It has a half-cylindrical front edge and a conical rear edge. The arrangement of the electrodes and magnets starts at the front edge of the plate, is 90 mm in length and covers the whole plate width. In the left image, the unaffected flow at the bottom side of the profile detaches at the front edge. The right image shows that the Lorentz-force, which is applied to act in direction of the flow, causes the flow to attach completely. Due to the pressure increase in the outside flow, the interface flow near the front edge is significantly decelerated.

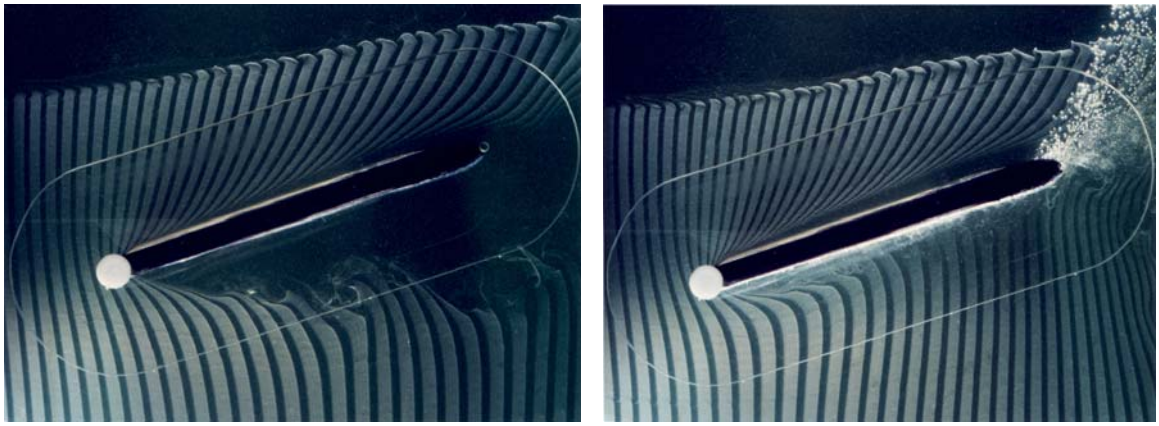

Figure 5.4.9 Plate in oblique approach flow without and with Lorentz-force by Weier [2005]

Afterwards, the fluid near the wall is accelerated by the Lorentz-force, generating many electrolysis bubbles. In contrast to electron conductors such as metals, electrolytes are ion conductors. In order to be electrically conductive, electrolytes must hold a sufficient number of charge carriers, which are attained by electrolysis. This process generates gas bubbles, which, depending on the electrolyte, may consist of oxygen, chlorine or hydrogen. The bubble diameter ranges at $d_B \approx (5\text{-}20)\mu m$ and is dependent on velocity and flow density. Bubbles, released at a certain velocity, do not only influence the critical Reynolds number and thus, the transition, they are also potential cavitation nuclei. Consequently, a resulting question is whether there is a method of influencing interfaces by means of electro-magneto-hydrodynamics without the inevitable generation of bubbles.

In any case, when working with so-called unaffectable electrodes as they are employed in salt water, the application of stationary Lorentz-forces in order to influence flow will always be connected with the release of gas bubbles. However, there is the possibility to realize electric current but avoiding gas production. By impressing an alternating current of a certain frequency, the capacity of the electrolytic bilayer is exploited, which, however, causes the Lorentz-force change direction constantly. Here is only a short description of this process in detail since it is rather complicated:

That electrolytic bilayer is generated at the electrode's surface when it is immersed in an electrolyte. In the simplest case, this bilayer resembles a charged plate capacitor of a certain capacity. When an alternating voltage is impressed, the bilayer's polarity is changed while a current flows through the electric circuit that consists of cathode, anode and electrolyte with the necessity of charge carriers moving through the phase interface electrode/electrolyte. High current densities can be reached with high frequencies. However, the amplitude of the alternating current must remain below the corrosion voltage E_z of the electrolyte. In seawater, this is $E_{z,O_2} = 1{,}23\,V$ for producing oxygen, and $E_{z,Chlor} = 1{,}37\,V$ for producing chloride.

Research about unsteady stimulation of detached flows at hydrofoils by externally applying sound has shown that this stimulation can cause the partial re-attachment of the detached flow (Greenblatt & Wygnanski [2000]). This, in turn, leads to significantly increased lift and reduced drag coefficients. The frequency of stimulation is essential. Stimulation of large vortex structures close to and downstream of the point of detachment results in shortening the detachment bubble.

Periodic stimulation of detached flows by means of time-dependent Lorentz-forces was examined by Weier [2005]. Figure 5.4.10 shows the influence of the detached flow around a plane plate as dependent on a dimensionless stimulation frequency and a specially defined impulse coefficient c'_μ. While the unaffected flow at the under-side of the profile detaches at the front edge, the area of detachment is reduced with higher impulse coefficients. Similar to stationary Lorentz-forces, the influence on drag and lift can clearly be verified.

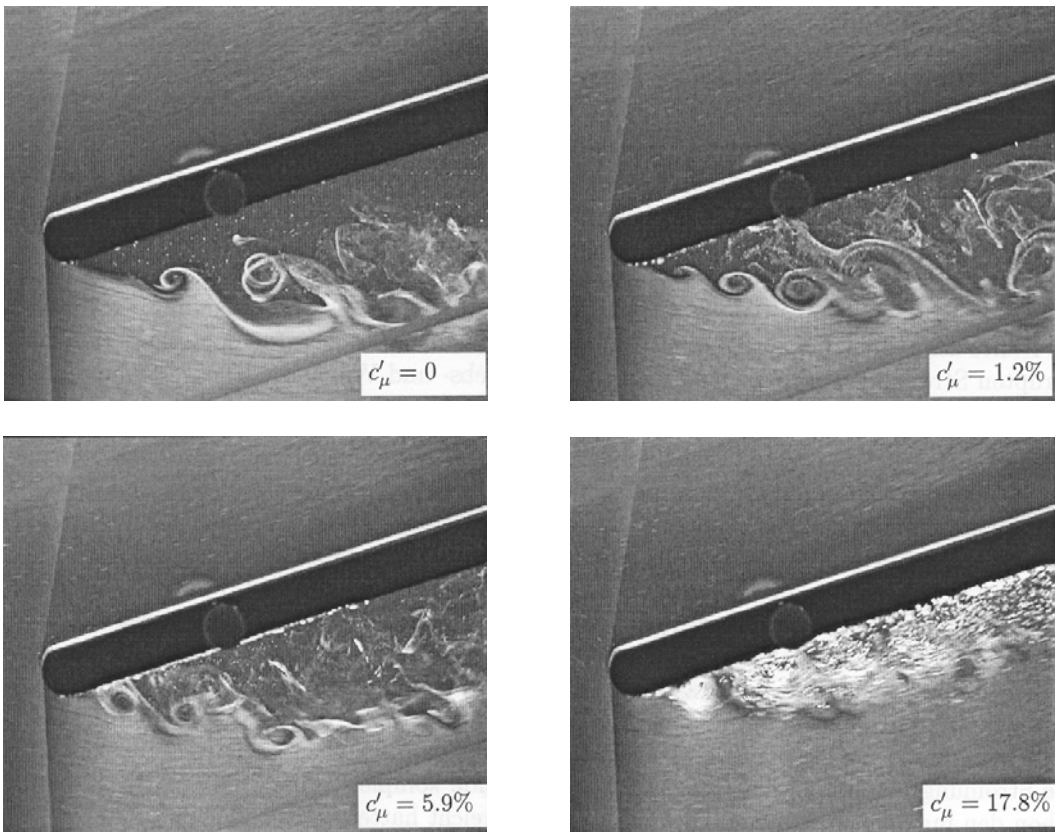

Figure 5.4.10 Experiments with oscillating Lorentz-force at an oblique plate by Weier [2005]

6 Concluding Remarks

The development of fluid mechanics during the twentieth century has been affected by intense research in order to fathom numerous practically relevant hydrodynamic effects, to understand the physical processes and correlations and to describe them mathematically. This became necessary because employing only the fundamental hydrodynamic equations, the description of certain phenomena in fluid flows caused by fluid properties was impossible.

It has been essential to examine water regarding its solvent properties, particularly concerning gases and furthermore the insight that nuclei are always present in water. These nuclei, especially stabilized gas bubbles, neutralize the inter-molecular forces of the fluids at their interfaces and therefore considerably reduce the applicable tensile stress. Additionally, studies were needed concerning the behavior of such nuclei in flows under the influence of alternating surrounding conditions, e.g. oscillation behavior and growth due to diffusion.

In order to assess the quality of fluids regarding their gas contents and their nuclei distributions, various measuring methods and devices have been developed and constructed since the beginning of the twentieth century. This historical development could be described nearly completely in this work, particularly the development of devices to determine the total gas content. Apart from the mostly difficult handling of these measurement methods and devices, only the influence of single parameters such as the total gas content, the dissolved oxygen content, nucleus content, nucleus distribution and the distribution of nucleus sizes on hydrodynamic effects was examined. However, the correlations between these single parameters, as they occur in real flows, could not be taken into consideration.

As early as the end of the ninetieth century the development of methods and devices began to determine the tensile strength of fluids. The initially static methods have been followed by the developments of dynamic methods since the beginning of the 1970s. While for specially prepared fluids, tensile strengths of several hundred bar were measured under static conditions, the typical values for water, measured with the eddy and swirl nozzle, range between zero and two bar. This illustrates the strong influence of interactions between all parameters on the tensile strength in flowing fluids.

Except for sound velocity and pressure distribution at profiles, water quality particularly affects certain cavitation phenomena. Various cavitation tests around the world have shown that without determining the actual tensile strength of the test water, it is impossible to obtain reproducible results regarding cavitation inception. In experiments concerning cavitation erosion, the correlation between water quality, erosive aggressiveness and erosion rate was proven unmistakably. Evidently, permanent measurement of the test fluid's tensile stress during cavitation experiments with model bodies is compulsory in order to be able to interpret measurement results correctly.

Cavitation phenomena at profiles or other parts affected by flow cause changes of lift, drag and loss coefficients depending on the degree of the cavitation progress. The influence of transition, detachment, obstruction and pressure distribution plays a special role. The quality of electrically conductive fluids is determined by their conductivity. By means of electromagnetic fields Lorentz-forces are generated, whose effect can be observed in lessening of flow detachment, drag reduction and increased lift.

Manifold experimental research results in the area of fluid mechanics have proven that the fluid quality must be taken into account when describing real flow processes. Since the many flow parameters are subject to permanent interaction, ultimately, the sum of all single parameters lead to the effects mentioned. For the determination of the water quality such as in cavitation experiments, the tensile stress of the water can be measured making the mathematical description of cavitation inception possible.

Bibliography

Ackeret, J. [1930]
Experimentelle und theoretische Untersuchungen über Hohlraumbildung (Kavitation) im Wasser.
Technische Mechanik und Thermodynamik, VDI - Zeitschrift, Bd. 1, Berlin.

Acosta, A. J.; Parkin, B. R. [1970]
Cavitation Inception – A Selective Review.
Proceedings of the 17th American Towing Tank Conference.

Ahmed, O. [1972]
Cavitation Nuclei Measurements in a Closed Water Tunnel.
Ph.D. Thesis, Department of Nuclear Engineering, University of Michigan, Ann Abor.

Ahmed, O.; Hammitt, F. G. [1969]
Determination of Particle Population Spectra from Water Tunnel Using Coulter Counter.
ASME Cavitation Forum, pp. 26 - 28.

Apfel, R. E. [1971]
A Novel Technique for Measuring the Strength of Fluids.
The Journal of the Acoustical Society of America, S. 145 – 155.

Apfel, R. E. [1972]
The Tensile Strength of Liquids.
Scientific American, S. 58 – 71, Dec. 1972.

Apfel, W. H.; Roestel, T. [1974]
Berechnung der Druckverteilung an Flügelprofilen in gashaltiger Wasserströmung.
ZAMM 54, S.571.

Arndt, R. E. A.; Ellis, C. R.; Paul, S. [1995]
Preliminary Investigation of the Use of Air Injection to Mitigate Cavitation Erosion.
Transactions of the ASME, Vol. 117, pp. 498 - 504.

Arndt, R. E. A.; Keller, A. P.. [2003]
A Case Study of International Cooperation: 30 Years of Collaboration in Cavitation Research.
FEDSM'03, ASME Fluids Engineering Division Summer Meeting, Honolulu, Hawaii, Juli 6-10, 2003.

Arndt, R. E. A.; Maines, B. H. [1994]
Vortex Cavitation: a Progress Report.
ASBE FED-Vol. 90, Lake Tahoe, Nevada.

Bachert, B.; Bernhard, B.; Stoffel, B. [2003]
Experimental Investigations Concerning Influences on Cavitation Inception at an Axial Test Pump.
FEDSM'03, ASME Fluids Engineering Division Summer Meeting, Honolulu, Hawaii, Juli 6-10.

Barlow, E. J.; Langlois, W. E. [1962]
Diffusion of Gas from a Liquid into an Expanding Bubble.
IBM Journal of research an development, Vol. 6, No. 3, pp. 329 - 337.

Berthelot, M. [1850]
Sùr quelques phenomènes de dilatation forcèe de liquides.
Ann. Cim. Phys. (3), 30, 2321-2342.

Biesheuvel, A.; van Wijngaarden, L. [1984]
Two Phase Flow Equations for a Dilute Dispersion of Gas Bubbles in Liquid.
Journal Fluid Mechanics 148, p. 301.

Billet, M. L.; Gindroz, B. [1988]
Influence of the Nuclei on the Cavitation Inception for Different Types of Cavitation on Ship Propellers.
Journal of Fluids Engineering, ASME.

Böhm, R. [1998]
Erfassung der hydrodynamischen Beeinflussung fortgeschrittener Kavitationszustände und ihrer erosiven Aggressivität.
Dissertation. Technische Universität Darmstadt.

Brand F. [1973]
Vorrichtung zum Bestimmen der in einer Flüssigkeit enthaltenen Menge gelösten Gases.
Deutsches Patentamt, Auslegeschrift 2362158.

Briggs, L. J. [1950]
Limiting Negative Pressure to Water.
Journal of Applied Physics. Vol. 21, Juli 1950, 721-722.

Brockett, T. [1969]
Computational Method for Determination of Bubble Distributions in Liquids.
Naval Ship Research and Development Center Report 2798.

Bux, K. & Vollheim, R. [1987]
Untersuchungen zum Werkstoffverhalten bei Strömungskavitation - Kavitationserosion.
Forschungsbericht F 72. Technische Universität Dresden.

Campbell, I. J.; Pitcher, A. S. [1958]
Shock Waves in a Liquid Containing Gas Bubbles.
Proceedings Royal Society Ser. A 243, p. 534.

Ceccio, S. L.; Gowing, S.; Shen, Y. [1997]
The Effect of Salt Water on Bubble Cavitation.
Journal Fluid Mechanics.

Choffat, T.; Franc, J.-P.; Fortes-Patella, R.; Archer, A. [2003]
A Procedure to Account for Overlaping in Pitting Tests.
Fifth International Symposium on Cavitation (CAV 2003), November 1-4, Osaka, Japan.

d' Agostino, L.; Brennen, C. E.; Acosta, A. J. [1988]
Linearized Dynamics of Two-Dimensional Bubbly and Cavitating Flows over Slender Surfaces.
Journal Fluid Mechanics 192, p. 485.

D'Ans; Lax [1992]
Taschenbuch für Chemiker und Physiker.
Band 1, Physikalisch-chemische Daten. Springer-Verlag.

Donny, F. M. L. [1846]
Sur la cohèsion des leqùides, et sùr lèurs adhèrence aùx corps soliders.
Ann. Cim. Phys. (3), 16, 167-190.

Eickmann, G. [1992]
Maßstabseffekte bei der beginnenden Kavitation; Ihre gesetzmäßige Erfassung unter Berücksichtigung der wesentlichen Einflußfaktoren.
Dissertation. Bericht Nr. 69 der Versuchsanstalt Obernach und des Lehrstuhl für Wasserbau und Wassermengenwirtschaft der Technischen Universität München.

Eisenhauer, N. [1995]
The Effect of Aeration on Cavitation Erosion.
International Symposium on Cavitation, CAV'95, Mai 1995, Deauville, Frankreich.

Eller, A.; Flynn, H. G. [1965]
Rectified Diffusion during Nonlinear Pulsations of Cavitation Bubbles.
Journal of The Acoustical Society of America, Vol. 37, pp. 493 - 503.

Ellis, A. T. [1965]
Parameters Affecting Cavitation and Some New Methods for Their Study.
California Institute of Technology, Hydrodynamics Laboratory Report E-115.1.

Elsner, N. [1980]
Grundlagen der Technischen Thermodynamik.
Akademie – Verlag Berlin, 4. bearbeitete und erweiterte Auflage.

Elsner, N.; Dittmann, A. [1993]
Grundlagen der Technischen Thermodynamik.
Akademie – Verlag Berlin, 8. Auflage, Bd. 1.

Epstein, P. S.; Plesset, M. S. [1950]
On the Stability of Gas Bubbles in Liquid-Gas Solutions.
Journ. Chem. Phys. 18, p. 1505.

Fox, F. E.; Carley, S. R.; Larson, G. S. [1955]
Phase Velocity and Absorption Measurements in Water Containing Air Bubbles.
Journal of the Acoustical Society of America, Vol. 27, No. 3, pp. 534 - 539.

Franks, F. [1984]
Water.
Royal Society of Chemistry Paperbacks, ISBN 0-85186-473-2, March 1984.

Gast, P. [1962]
Experimentelle Untersuchung über den Beginn der Kavitation an umströmten Körpern.
Dissertation. Technische Universität Darmstadt.

Gates, E. M.; Billet, M. L. [1980]
Cavitation Nuclei and Inception.
IHAR Symposium, Tokyo, Japan.

Gavrilov, L. R. [1970]
Free Gas Content of a Liquid and Acoustic Techniques for its Measurement.
Soviet Physics Acoustics, Vol. 15, No. 3.

Gindroz, B. [1992]
Qualification of a Centerbody Cavitation Nuclei Counter Using Optical Techniques.
XVI IAHR Symposium, Proceedings, pp. 595 - 604.

Gindroz, B.; Matera, F. [1996]
Influence of the Cavitation Nuclei on the Cavitation Bucket When Predicting the Full-Scale Behavior of a Marine Propeller.
21th Symposium on Naval Hydrodynamics, Trondheim, Norway.

Greenblatt, D.; Wygnanski, I. J. [2000]
The control of flow seperation by periodic excitation.
Prog. Aero. Sci. 36, pp. 487 - 545.

Grunert, K. [2000]
Untersuchungen zur Turbulenzmodellierung verdrallter Innenströmungen.
Dissertation. Technische Universität Berlin.

Harvey, E. N. et all [1945]
Removal of Gas Nuclei from Liquids and Surfaces.
Journal Am. Chem. Soc. 67, p. 156.

Harvey, E. N. et all [1947]
On Cavity Formation in Water.
Journal Appl. Physics 18, p.162.

Haussmann, G.; Lauterborn, W. [1978]
Automatische Bestimmung von Blasengrößenverteilungen anhand dreidimensionaler Hologrammrekonstruktion.
Bildverarbeitung und Mustererkennung, Hrsg. E. Triendl; Berlin: Springer, Informatik Fachberichte 17, S. 275 - 280.

Heller, W. [1991]
Erarbeitung einer Meßmethode für die Bestimmung des Gesamtgasgehaltes an Kavitationskanälen.
Diplomarbeit. Technische Universität Dresden.

Heller, W. [1995]
Experimentelle und numerische Untersuchungen zum Einfluß des Gasgehaltes auf die Strömungskavitation.
Institutsbericht I 1507. Technische Universität Dresden.

Heller, W. [1997]
Zum Einfluss der Turbulentenz der Anströmung auf die Druckwirkungen in Grenzschichten und den Kavitationsbeginn.
Dissertation. Technische Universität Dresden.

Heller, W. [1999]
On the Influence of the Turbulence of Flow on Pressure Effects in Boundary Layers and Cavitation Inception.
International Symposium on Cavitation Inception, San Francisco, USA, July 18-23.

Heller, W. [1999]
Cavitation Inception and Turbulence of Flow.
International Forum on Cavitation Inception, Wuhan, China, October 11-17.

Heller, W. [2003]
A New Approach for Determination of Cavitation Sensitivity of Water.
FEDSM'03, ASME Fluids Engineering Division Summer Meeting, Honolulu, Hawaii, Juli 6-10.

Heller, W. [2004]
Meßsystem zur Bestimmung der Kavitationsempfindlichkeit von Wasser.
75th Annual Scientific Conference, GAMM, Dresden, March 21 – 27.

Hentschel, W.; Lauterborn, W. [1980]
Holografische Erzeugung von Kavitationsblasensystemen.
Fortschritte der Akustik – DAGA '80, München, 11.-13. März; Berlin: VDE-Verlag, S. 411-414.

Hodgman, Ch. D. [1957]
Handbook of Chemistry and Physics.
Cleveland, USA.

Huber, R. [2004]
Geschwindigkeitsmaßstabseffekte bei der Kavitationserosion in der Scherschicht nach prismatischen Kavitatoren.
Dissertation. Technische Universität München.

Hutton, S. P.; Meshhedani, W. A. [1992]
The Effects od Air Injection upon Cavitation Erosion..
Cavitation, Intern. Conference, Cambridge, Proc. of the Institution of Mechanical Engineers.

Ilichev, V. I.; Neuimin, G. S. [1966]
Size Distribution Law of Gas Bubbles in a Turbulent Viscous Flow.
Soviet Physics Acoustics, Vol. 11, No. 4.

Isay, W. H.; Roestel, T. [1974]
Berechnung der Druckverteilung an Flügelprofilen in gashaltiger Wasserströmung.
ZAMM 54, S.571.

Isay, W. H.; Roestel, T. [1975]
Die niederfrequent instationäre Druckverteilung an Flügelprofilen in gashaltiger Wasserströmung.
ZAMM 55, S.465.

Isay, W. H. [1989]
Kavitation.
Schiffahrts - Verlag „Hansa" C. Schroeter & Co. Hamburg, 3. erweiterte Auflage.

Isay, W. H. [1992]
Zum Einfluß des Sättigungsgrades der im Wasser gelösten Luft sowie des Keimgehaltes auf den Kavitations-Einsatz.
Institut für Schiffbau der Universität Hamburg, Bericht Nr. 525.

ITTC [1972]
Report of the Cavitation Committee.
13th International Towing Tank Conference.

ITTC [1978]
Report of the Cavitation Committee.
15th International Towing Tank Conference.

ITTC [1990]
Report of the Cavitation Committee.
19th International Towing Tank Conference, Vol. 1, Madrid, Spain.

ITTC [1993]
Report of the Cavitation Committee.
20th International Towing Tank Conference, Vol. 1, San Francisco, California.

ITTC [1996]
Report of the Cavitation Committee.
21th International Towing Tank Conference, Vol. 1, Trondheim, Norway.

ITTC [2002]
Report of the Cavitation Committee.
22th International Towing Tank Conference.

Iyengar, K. S.; Richardson, E. G. [1956]
The Detection of Cavitation Nuclei.
Mechanical Engineering Research Laboratory, Fluid Mechanics Division, National Engineering Laboratory, East Kilbride, Scotland, Fluids Note 42.

Keller, A. P. [1970]
Ein Streulicht-Zählverfahren, angewandt zur Bestimmung des Kavitationskeimspektrums.
OPTIK, Band 32.

Keller, A. P. [1973]
Experimentelle und theoretische Untersuchungen zum Problem der modellmäßigen Behandlung von Strömungskavitation.
Technische Universität München, Versuchsanstalt für Wasserbau. Bericht Nr. 26.

Keller, A. P.; Yilmaz, E.; Hammitt, F. G. [1974]
Comparative Investigations of the Scattered Light Counting Method for the Registration of Cavitation Nuclei and the Coulter Counter.
The University of Michigan, Department of Mechniacal Engineering, Cavitation and Multiphase flow Laboratory, Report No. UMICH 01357-36-T, January 1974.

Keller, A. P. & Zielke, W. [1976]
Veränderung des freien Gasgehaltes einer turbulenten Rohrströmung bei plötzlichen Druckabsenkungen.
Technische Universität München, Versuchsanstalt für Wasserbau. Bericht Nr. 32.

Keller, A. P. & Prasad, R. [1978]
Einfluß der Vorgeschichte des Testwassers auf den Kavitationsbeginn an umströmten Körpern.
Technische Universität München, Versuchsanstalt für Wasserbau. Bericht Nr. 39.

Keller, A. P. [1980]
Beginnende Kavitation.
Schlussbericht für VDMA. Technische Universität München, Versuchsanstalt für Wasserbau.

Keller, A. P. [1983]
Maßstabseffekte bei der Anfangskavitation.
Technische Universität München, Versuchsanstalt für Wasserbau. Bericht Nr. 47.

Keller, A. P. [1984]
Maßstabseffekte bei der Anfangskavitation unter Berücksichtigung der Zugspannungsfestigkeit der Flüssigkeit.
Pumpentagung Karlsruhe ´84. Fachgemeinschaft Pumpen im VDMA
.
Keller, A. P.; Eickmann, G [1989]
Velocity and Size Scale Effects for Incipient Cavitation of Axisymmetric in Water of Different Quality.
International Symposium on Cavitation Inception, ASME, San Francisco, 1989.

Keller, A. P. [1994]
New Scaling Laws for Hydrodynamic Cavitation Inception.
The International Symposium on Cavitation. Proceedings. Tokyo, Japan.

Keller, A. P. [1996]
Zum Einfluß der Turbulenz der Anströmung auf den Kavitationsbeginn – der Turbulenzmaßstabseffekt.
Pumpentagung Karlsruhe.

Keller, A. P.; Rott, H. [1997]
The Effect of Flow Turbulence on Cavitation Inception.
Pumpentagung Karlsruhe.

Keller, A. P.; Rott, H.K.; Stoffel, B.; Striedinger, R. [1999]
Maßstabseffekte bei der Strömungskavitation.
Forschung im Ingenieurwesen 65 (1999), 48-57, Springer Verlag.

Keller, A. P.; [2000]
Cavitation Scale Effects – A Representation of its Visual Appearance and Empirically Found Relation.
NTC'50, International Conference on Propeller Cavitation, April 2000, University of Newcastle.

Keller, A. P. [2001]
Cavitation Scale Effects – Empirically Found Relation and the Correlation of Cavitation Number and Hydrodynamic Coefficient.
CAV 2001, 4th International Symposium on Cavitation, California Institute of Technology, Pasadena, California, USA, June 20-23, 2001.

Keller, A. P.; Pan, S.; Yang, Z. [2003]
Comparison Testes for Checking Relations for Cavitation Scale Effects.
FEDSM'03, ASME Fluids Engineering Division Summer Meeting, Honolulu, Hawaii, Juli 6-10, 2003.

Kempe, T. [2005]
Numerische Untersuchung der Strömung in einer Dralldüse.
Projektarbeit. Technische Universität Dresden, Institut für Strömungsmechanik.

Kenn, M. J.; Garrod, A. D. [1981]
Cavitation damage and the Tarbela tunnel collapse of 1974.
Proceedings Inst. Civ. Engineers Part 1, Vol. 70, 65 - 89.

Killen, J. M.; Ripkin, J. R. [1964]
A Water Tunnel Air Content Meter.
University of Minnesota, St. Anthony Falls Hydraulic Laboratory, Project Report No. 70.

Knapp, R. T. [1957]
Cavitation Scale Effect.
Trans. of the 7th General IAHR - Meeting, Vol. 1, Lisboa.

Knapp, R. T. ; Daily, J. W.; Hammitt, F. G. [1970]
Cavitation.
McGraw-Hill Book Company, New York St. Louis San Francisco Düsseldorf London Mexico Panama Sydney Toronto.

Kümmel, K. [1978]
Theoretische und experimentelle Untersuchungen über die Rolle der Strömungskeime bei der Entstehung von Flüssigkeitskavitation.
Dissertation. Technische Hochschule Darmstadt.

Kuz, K. D. [1971]
Ein Beitrag zur Frage des Einsetzens von Kavitationserscheinungen in einer Düsenströmung bei der Berücksichtigung der im Wasser gelösten Gase.
Universität Stuttgart. Mitteilungen Heft 19.

Landa, I.; Tebay, E. S.; Johnson, V.; Lawrence, J. [1970]
Measurement of Bubble Size Distribution Using Scattered Light.
Hydronautics, inc., Technical Report 707-4, June 1970.

Lauterborn, W. [1969]
Fotografische Aufnahmen vom Aufreißen einer rotierenden Wassersäule und Zerreißfestigkeitsmessungen an Wasser nach der Zentrifugenmethode.
Acustica 22 (1), S. 35 - 47.

Lauterborn, W.; Hinsch, K.; Bader, F. [1972]
Holography of Bubbles in Water as a Method to Study Cavitation Bubble Dynamics.
Acustica 26 (1), S. 170 – 171.

Lauterborn, W.; Ebeling, K.-J. [1977]
High-Speed Holography of Laser-Induced Breakdown in Liquids.
Appl. Phys. Letters 31, pp. 663 – 664.

Lauterborn, W.; Haussmann, G.; Steinhoff, W. [1979]
Digitale Verarbeitung dreidimensionaler holografischer Bilder.
Informationssysteme, Honeywell Bull Magazin 1, S. 19 - 23.

Lauterborn, W. [1980]
Cavitation and Coherent Optics.
Proceedings of the First International Conference on Cavitation and Inhomogeneities in Underwater Acoustics, Göttingen, 9.-11. Juli, Springer Verlag, Berlin – Heidelberg – New York.

Lauterborn, W.; Hentschel, W. [1989]
Holografische Hochgeschwindigkeitskinematografie.
Praxis der Holografie, Hrsg. H. Marwitz; Ehningen, Germany: Expert Verlag, S. 354 – 370 und 474 - 475.

Manley, J. P. [1960]
Change of Size of Air Bubbles in Water Containing a Small Dissolved Air Content.
British Journal of Applied Physics, Vol. 11.

Messio, D.; Sette, D.; Wanderlingh, F. [1963]
Statistical Approach to Ultrasonic Cavitation.
Journal of the Acoustical Society of America, Vol. 35, No. 10, pp. 1575 - 1583.

Moerch, K. A. [1986]
Cavitation Nucleation by Solid Particles in a Focussed Acoustic Field.
Proc. International Symposium on Cavitation. Sendai, April 1986.

Moerch, K. A. [1999]
Cavitation Nuclei and Bubble Formation - a Dynamic Liquid-Solid Interface Problem.
Proc. of the 1999 ASME/JSME Fluids Engineering Division Summer Meeting, July 18-23, 1999 San Francisco, California.

Nakoryakov, V. E.; Pokusaev, B. G.; Shreiber, I. R.; Pribaturin, N. A. [1988]
The Wave Dynamics of Vapour- Liquid Medium.
Intern. Journal Multiphase Flow 14, p. 655.

Neal, L. G.; Bankoff, S. G. [1963]
A High Resolution Resistivity Probe for Determination of Lokal Void Properties in Gas-Liquid Flow.
American Institute of Chemical Engineering Journal, pp. 490 - 494.

Numachi, F. [1936]
Über die Kavitationsentstehung mit besonderem Bezug auf den Luftgehalt des Wassers.
Ingenieur - Archiv, Band VII, S. 396 - 409.

Oldenziel, D. M. [1979]
Bubble Cavitation in Relation to Liquid Quality.
Ph.D. thesis, Technische Universität Twente, Delft Hydraulics Laboratory, Publication No. 211.

Peterka, A. J. [1953]
The Effect of Entrained Air on Cavitation Pitting.
Minnesota Hydraulics Convention.

Peterson, F. B.; Danel, F.; Keller, A. P.; Lecoffre, Y. [1975]
Comparative Measurement of Bubble and Particulate Spectra by three Optical Methods.
14th International Towing Tank Conference, Report of Cavitation Committee, Appendix 1.

Plesset, M. S.; Zwick, S. A. [1952]
A Nonsteady Heat Diffusion Problem with Spherical Symmetry.
Journal of Applied Physics, Vol. 23, pp. 329 - 337.

Rayleigh, Lord J. W. S. [1917]
On the Pressure Developed in a Liquid During the Collapse of a Spherical Cavity.
Phil. Mag. 34, p. 94.

Richardson, E. G. [1956]
Detection of Gaseous Nuclei in Liquids Using an Ultrasonic Reverberating Chamber.
Mechanical Engineering Research Laboratory, Fluid Mechanics Division, National Engineering Laboratory, East Kilbride, Scotland, Fluids Note 38.

Rood, E. P. [1991]
Review – Mechanism of Cavitation Inception.
ASME Journal of Fluids Engineering, Vol. 113, pp. 163 - 175.

Schiebe, F. R. [1969]
The Influence of Gas Nuclei Size Distribution on Transient Cavitation Near Inception.
St. Anthony Falls Hydraulic Laboratory, Project Report No. 107.

Schiebe, F. R.; Killen, J. M. [1971]
An Evaluation of Acoustic Techniques for Measuring Gas Bubble Size Distributions in Cavitation Research.
University of Minnesota, St. Anthony Falls Hydraulic Laboratory, Project Report No. 120.

Schöneberger, W. [1966]
Untersuchungen über Kavitation an radialen Kreiselpumpenrädern.
Dissertation. Technische Hochschule Darmstadt.

Schweitzer, P. H. & Szebekely, V. G. [1950]
Gas Evolution in Liquids and Cavitation.
Journal of Applied Physics, Vol. 21, No. 12, pp. 1218 - 1224.

Shen, Y. T.; Gowing, S.; Ceccio, S. [1994]
Salt Water Effects on Bubble and Sheet Cavitation.
21th International Symposium on Cavitation, Tokyo, Japan.

Silbermann, E.; Schiebe, F. R. [1973]
The Use of Standard Bodies to Measure the Cavitation Strength of Water.
University of Minnesota, St. Anthony Falls Hydraulic Laboratory, Project Report No. 141.

Skarsoulis, M. [1988]
Instationäre Theorie der Porenkeime.
VDI-Fortschrittsberichte, Reihe 7, Strömungsmechanik Nr. 141.

Stoffel, B.; Striedinger, R. [2000]
Kavitation
Vorlesungsvordruck zur Vorlesung. 2000.

Strasberg, M. [1955]
Undissolved Air Cavities as Cavitation Nuclei.
Cavitation in Hydrodynamics, Proc. of a Symposium at the National Physical Laboratory.

Strasberg, M. [1956]
The Onset of Ultrasonic Cavitation in Tap Water.
Catholic University Ph.D. Dissertation.

Strasberg, M. [1957]
The Influence of Air-Filled Nuclei on Cavitation Inception.
David Taylor Model Basin Report 1078.

Striedinger, R. [2002]
Ein Beitrag zur Bedeutung der Wasserqualität und von Maßstabsgesetzen in Kreiselpumpen bei beginnender Kavitation.
Dissertation. Technische Universität Darmstadt.

Strube, H. W.; Lauterborn, W. [1970]
Untersuchung der Kavitationskeime an der Grenzfläche Quarzglas-Wasser nach der Zentrifugenmethode.
Zeitschrift Angewandte Physik 29, S. 349 - 357.

Suslick, K. S. [1989]
Die chemischen Wirkungen von Ultraschall.
Spektrum der Wissenschaft, S. 60 - 66.

Tan, M. J.; Bankoff, S. G. [1984]
Propagation of Pressure Waves in Bubbly Mixtures.
Physics of Fluids 27, p. 1362.

Thoma, D. [1925]
Kavitation.
VDI - Zeitschrift, Nr. 69.

TOPAS [2001]
Partikel Analyse System für Flüssigkeiten.
Topas GmbH, www.topas-gmbh.de.

Trevena, D. H. [1987]
Cavitation and Tension in Liquids.
Adam Hilger, Bristol and Philadelphia, ISBN 0-85274-454-4.

Tsinober, D. J.; Shtern, A. G. [1967]
On the possibility to increase the stability of the flow in the boundary layer by means of crossed electric and magnetic fields.
Magnitnaya Gidrodinamica 3 (1967), Nr. 2, S. 152-154.

Turner, W. R. [1963]
Physics of Microbubbles.
Vitro Laboratories, Technical Note 01645 01-2, Silver Spring, Maryland.

Turner, W. R. [1963]
Ultrasonic Measurement for Microbubble Research.
Vitro Laboratories, Technical Note 01645 01-1, Silver Spring, Maryland.

Turner, W. R. [1969]
Acoustic Microbubble Spectrum Analyser.
Vitro Laboratories, Technical Note 01992 01-1, Silver Spring, Maryland.

Van Slyke, D. D.; Neill, J. M. [1924]
The determination of gases in blood and other solutions by vacuum extraction and manometric measurement.
The Journal of Biological Chemistry, Vol. 61, pp. 523 - 572.

van Wijngaarden, L. [1972]
One Dimensional Flow of Liquids Containing Small Gas Bubbles.
Ann. Rev. Fluid Mechanics 4, p. 369.

van Wijngaarden, L. [1979]
Sound and Shock Waves in Bubbly Liquids. Cavitation and Inhomogeneities in Underwater Acoustics.
Proceedings 1st Intern. Conf. Göttingen, p. 127. Springer Verlag Berlin – Heidelberg – New York.

Wagner, W.; Kruse, A. [1998]
Properties of Water and Stream.
Zustandsgrößen von Wasser und Wasserdampf.
ISBN 3-540-64339-7, Springer-Verlag Berlin Heidelberg New York.

Watanabe, M.; Prosperetti, A. [1994]
Mass Diffusion Effects an Cavitation Nuclei.
The Second International Symposium on Cavitation, Proceedings. Tokyo, Japan.

Weier, T., Fey, U., Gerbeth, G., Mutschke, G., Avilov, V. [2000]
Boundary layer control by means of electromagnetic forces.
ERCOFTAC Bulletin, Vol. 44, pp. 36-40.

Weier, T. [2005]
Elektromagnetische Strömungskontrolle mit wandparallelen Lorenzkräften in schwach leitfähigen Fluiden.
Dissertation. Technische Universität Dresden.

Wieghardt, K. [1967]
Kompressibilitätseffekte in Wasser mit freiem Luftgehalt.
Schiffstechnik 14, S. 24.

Winkler, L. W. [1889]
Die Löslichkeit des Sauerstoffs in Wasser.
Berichte der Deutschen chem. Gesellschaft, Jahrgang XXII.

Winter, K.; Keller, A. P.; Strobl, T. [1998]
Erfahrungen mit Belüftung von Francisturbinen zur Vermeidung von Kavitationserosion.
Berichte der Versuchsanstalt Obernach und des Lehrstuhls für Wasserbau der Technischen Universität München, Heft Nr. 82.

Young, F. R. [1989]
Cavitation.
McGraw-Hill Book Company.